Computational Modeling of Propeller Noise: NASA SR-7A Propeller

by

Karim Moussa

A thesis

presented to the University of Waterloo

in fulfillment of the

thesis requirement for the degree of

Master of Applied Science

in

Mechanical Engineering

Waterloo, Ontario, Canada, 2014

I hereby declare that I am the sole author of this thesis. This is a true copy of the thesis, including any required final revisions, as accepted by my examiners.

I understand that my thesis may be made electronically available to the public.

Abstract

The aerospace industry has been concerned with propeller noise levels for years. This interest is two-fold: government regulation and comfort in cabin. This report attempts to create a simulation mechanism needed to evaluate the far-field noise generation levels. However, in order to do that, the tandem cylinder case was evaluated first as a validation step before the SR-7A propeller case was performed. Both cases use STAR-CCM+, a commercial software, to perform the simulations.

The tandem cylinder case involved simulating two cylinders equal in diameters (D = 0.05715m) at a separation distance of 3.7D from center-to-center in a flow with Re # = 166,000 corresponding to Mach number of 0.128. The spanwise dimension of the domain was set to 3D to reduce the number of mesh cells and the resulting computational cost.

A Detached Eddy Simulation (DES) coupled with a k-ω SST turbulence model was used to model this case. The acoustic results were obtained using the Ffowcs Williams-Hawkings model. The aerodynamic and acoustic results were compared to the experimental results performed in the Basic Aerodynamic Research Tunnel (BART) and Quiet Flow Facility (QFF) test facilities.

The results showed that there was negative flow behind the upstream cylinder. This caused the shear layers to extend further downstream and eventually lead to the delayed roll-up with the presence of adverse streamwise and favourable crossflow pressure gradients. This affected mean pressure coefficient in the downstream cylinder. No clear distinct peaks are available in the sound pressure level analysis of the receiver locations due to the low sampling time. However, the primary shedding frequency matches the QFF results with the trends and broadband being reasonably captured.

The SR-7A propeller simulation was simulated to produce three different results – power coefficient, unsteady pressure coefficient, and the sound pressure level at receiver locations. All the simulations used the same computational setup and meshing parameters, unless otherwise stated. The moving reference frame approach was employed followed by the sliding mesh approach for the unsteady simulation. The k-ω SST turbulence model was employed at cruise conditions with an advance ratio of 3.06.

The power coefficient results were obtained for 0.6, 0.7, and 0.8 Mach numbers and were compared to NASA results. The simulation results matched the experimental results very well at the three Mach numbers. This was the first step in validating the aerodynamics of the case.

The unsteady pressure coefficient results were obtained using the inviscid code with a 0.8 Mach number at freestream in order to match the aerodynamic results predicted by NASA Euler code. The inflow angle was set to 1.6° and the results were compared at one transducer location on the suction and pressure surface of the blade (2 locations in total).

Two different meshes were employed on the same domain setup. The coarser mesh did not produce reasonable results. Unusual separation was noticed primarily on the suction surface of the blade and it translated in the unsteady pressure coefficient to be wrongly predicted. There was extensive fluctuation on the waveform and the magnitude were an order of magnitude higher at times. After analysis, it was apparent that the mesh is a major factor and a relatively finer mesh was developed. The results improved significantly at the 0.65R – 0.1c transducer location. The trend was well captured and the fluctuations ceased on the suction and pressure surfaces.

The acoustic simulations involved obtaining the sound pressure levels at 0.6 and 0.7 Mach numbers for the five receiver locations and comparing it to NASA wind tunnel experimental results. At both Mach numbers, the blade passing frequencies and their associated harmonics were well captured for all receivers. The sound pressure levels were well captured for the most part at Receivers A to D, with a maximum deviation of 5 dB below NASA results at Receiver D. At 0.7 Mach number, the simulation results deviated by about 5 dB below the corrected NASA wind tunnel experiments at all receivers for the third harmonic. At Receiver E, the sound pressure levels were about 15 dB below the NASA results for the blade passing frequency for Both Mach numbers. However, the gap continued to increase at the second and third harmonics for 0.7 Mach number.

The directivity results were promising as well. At the 0.6 Mach number, the simulation results captured the directivity trend relatively well. The is a sharper decrease in the sound pressure level between 110° and 131° compared to the NASA results. With an exception to 131°, the directivity is relatively flat.

For 0.7 Mach number, the directivity trend for the blade passing tome directivities is somewhat captured. This lobed pattern is consistent with the NASA results with a slight drop in the sound pressure level at 100° from propeller axis followed by a rise in the sound pressure level at 110° to the same level as it was at 90°. Similar to 0.6 Mach number, the magnitude of the sound pressure level is lower except at 100°. The is a sharper decrease in sound pressure level between 110° and 131° compared to the NASA results.

Acknowledgments

I would like to express my sincere gratitude to my advisor Prof. Fue-Sang Lien for his invaluable and continuous support in this MASc. research. His immense knowledge, guidance, motivation, and approachable attitude made it possible for the completion of this thesis.

I would also like to thank my co-advisor Prof. Armaghan Salehian for her continuous support and willingness to help in my MASc. research. I have learned a lot from her during the first research project.

I would like to thank WATCFD, NSERC IPS, and NSERC ENGAGE for their generous financial support of this research. I would like to thank Kung-Jun Hsieh for the invaluable discussions and for his contributions in different presentations and reports. This thesis would not have reached to this shape without his support. I would also like to thank Sid-Ali Meslioui, Daniel Opoku, and Man-Chun Tse from Pratt-Whitney Canada for their invaluable time and comments throughout the research process.

Last but not least, I would like to thank my parents for their continuous encouragement and support in every new chapter in my life. I would never have reached where I am without their assistance. I will forever be indebted.

To my parents, brother, family, and loved ones

Table of Contents

List of Figures

List of Tables

Nomenclature

x_i	generic direction
u_i	*i-th* component of velocity
t	time
p	pressure,
ρ	density
ν	dynamic viscosity
τ_{ji}	viscous stress tensor
$u_i{}'$	Reynolds fluctuating quantity
$u_i{}''$	Favre fluctuating quantity
$\bar{u}_i$	mean Reynolds averaging
$\tilde{u}_i$	mean Favre averaging
k	turbulent kinetic energy
ω	specific dissipation rate
ε	turbulence dissipation rate
μ_t	turbulent eddy viscosity
R_{ij}	Reynolds stress tensor
C_{lim}	clip factor
$\tilde{S}_{ij}$	mean strain rate tensor
P_k	production rate of turbulence
F_1, F_2	blending functions
$CD_{k\omega}$	part of the cross-diffusion term
l_t	turbulent length scale

C_{des}	DES model constant
Δ	maximum grid dimension between cell centers
F_{DES}	switching function between RANS and LES models
c	speed of sound
ρ'	perturbation density
T_{ij}	Lighthill turbulence stress tensor components
$\delta(f)$	Dirac delta function
v_n	local normal velocity
l_i	local force intensity acting on fluid
ρ_0	free-stream density
$H(f)$	Heaviside function
$\mathrm{v_r}$	relative velocity viewed from the rotating frame
C_L	lift coefficient
C_D	drag coefficient
D	diameter
A	area
U_o	free-stream velocity
F	frequency needed to be resolved
M	number of recommended cells per acoustical wavelength
J	advance ratio .
n	rotational speed in revolutions per second (rps),
P	power produced by the propeller
$C_{pressure}$	unsteady pressure coefficient
C_{power}	power coefficient
SPL	sound pressure level

Re	Reynolds number
y+	normalized wall coordinate
θ	azimuthal angle
M_{ht}	helical tip Mach number
R	radius
β	blade setting angle
Ma	Mach number

Chapter 1

Introduction

1.1 Motivation

The turboprop idea was first published in 1928 by the Hungarian engineer György Jendrassik. During World War II, he produced and tested the first 100-hp experimental engine in Budapest [20]. At the same time, other countries like Soviet Union, United States and United Kingdom were producing their own experimental versions. Turboprop engines eventually became a new topic of research. It was extremely promising due to the drastic fuel savings they offered.

Figure 1 shows the fuel savings that are achieved by using advanced turboprops over comparable technology turbofans at different trip lengths. At a 0.8 Mach number, the fuel savings range from 15-20% when the trip is primarily in cruise condition. This trend increases to about 30% at shorter trips where climb and descent dominates. A similar but higher fuel savings is observed at a Mach number of 0.7. Further savings can also be realized with the introduction of swirl recovery technology and advanced airfoil shapes. To take advantage of the fuel savings, there was a need to tackle the noise levels associated with the operation of a turboprop.

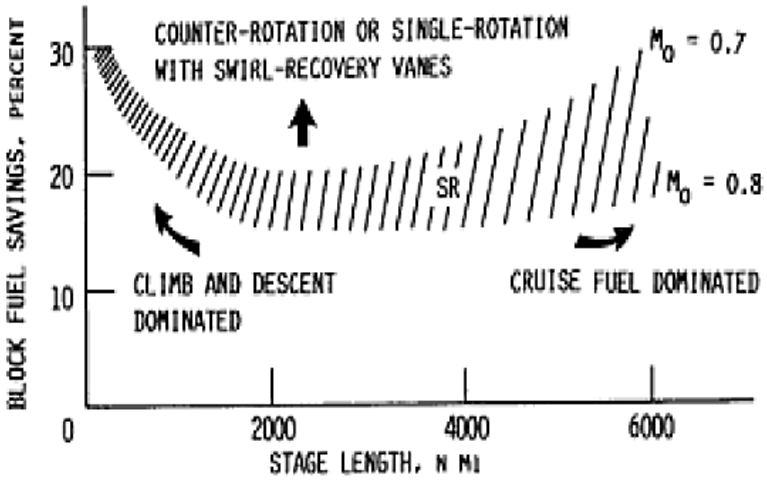

Figure 1: Fuel savings for advanced turboprops with respect to equivalent technology turbofan [42]

The aerospace industry has been concerned with the noise issue for years for two major reasons: the increasing pressure from international/governmental regulations and the needed in-cabin comfort. The environmental regulations are concerned with the noise levels at and around airports during the take-off and landing situations. The International Civil Aviation Organization

(ICAO) Annex 16 is the one involved with setting the standards of noise levels for aircraft and engine manufacturers. Figure 2 shows the measurement points that the ICAO are concerned with. They are the approach point (area before the landing), sideline (on the runway), and take-off point (area surrounding the take-off of the plane). At these locations, the aircraft should meet its specific noise limit which depends on the aircraft's maximum takeoff weight and the number of engines.

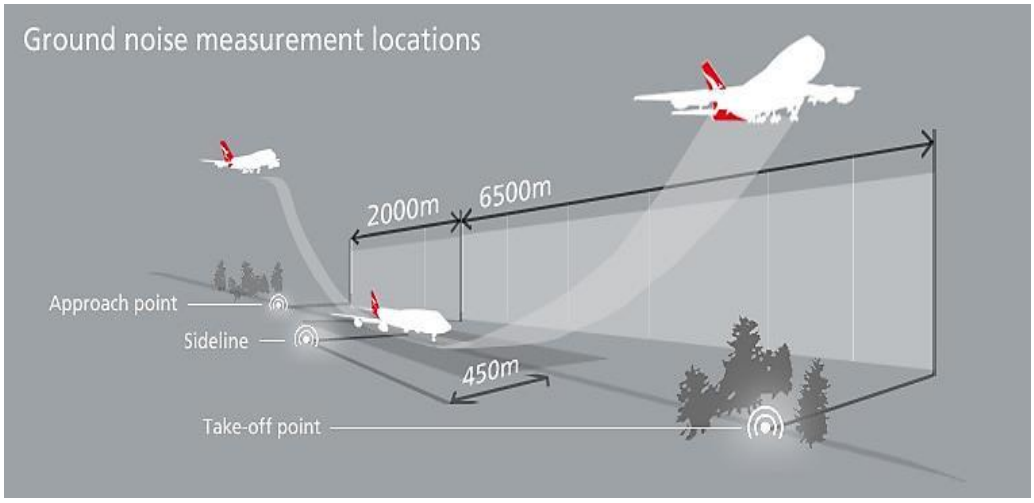

Figure 2: ICAO Noise Measurement Points [40]

ICAO Annex 16 was revised in March 2002 and a new Chapter 4 noise standard was introduced. This standard requires that all aircrafts newly certified starting January 2006 to remain below the older Chapter 3 noise levels by 10 decibels or more [7]. This, in turn, is the strictest noise protection standard currently in force. These regulations are expected to become more and more stringent with the introduction of more Chapters. This will eventually require more research into the aeroacoustic field to fulfil the requirements.

The comfort in the cabin was an important issue when the aeroacoustic research was initiated due to the high noise levels during cruise. However, it is now primarily an added marketing advantage for the manufacturer in order to have a competitive edge in the industry, thereby attracting more customers.

1.2 Background

In the mid-1970s, the National Aeronautics and Space Administration (NASA) established the Advanced Turboprop Program (ATP). The purpose of this major research is to establish the technology base required to lead to the application of the advanced turboprop propulsion system concept [42]. Since its initiation, various researchers ([8], [13], [18], and [24]) conducted aerodynamic and acoustic tests on several different propeller models such as SR-2, SR-1, SR-3, SR-6, etc. in the NASA Lewis wind tunnel. These propellers are 0.622 m (24.5 in.) in diameter with the SR-2 propeller only having straight (unswept) blades. Figure 3 shows the photographs for the SR-2, SR-1, and SR-3 propeller blades.

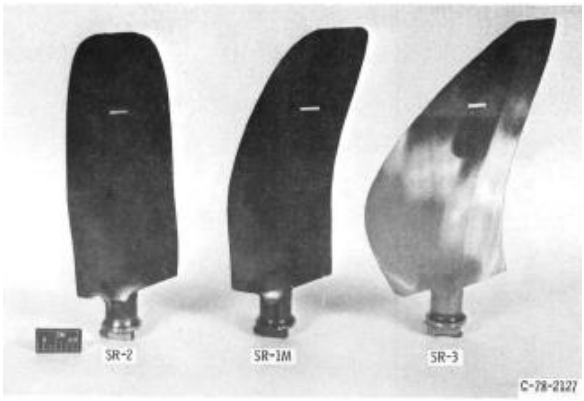

Figure 3: Propeller blades [8]

Another propeller blade, SR-7, received extensive attention by the researchers at NASA. Its development was a two-phase process that occurred simultaneously. One phase, referred to as the Large-Scale Advanced Prop-Fan Program (LAP), involved the design, fabrication, and ground testing of a 2.743 m (9-ft) diameter propeller [47]. Upon completion, this prop-fan (designated as SR-7L) would be incorporated on a test bed Gulfstream II aircraft as shown in Figure 4 under the Propfan Test Assessment (PTA) program. Lockheed Aircraft and United Technologies were an integral part of this research. This phase involved extensive aeroacoustic testing under actual flight conditions over the Lockheed-Georgia facility.

Figure 4: SR-7L propeller on the Gulfstream II aircraft [47]

Phase two involved the creation of an aeroelastically-scaled 0.622 m (24.5 in.) model (designated as SR-7A) to help measure the aerodynamic performance of the propeller which could not be performed in the phase one flight test [12]. A secondary objective of the SR-7A was to obtain acoustic results through wind tunnel testing. Figure 5 shows the SR-7A propeller inside the NASA Lewis wind tunnel. These acoustic results were compared to flight test results after the required acoustic scaling was performed.

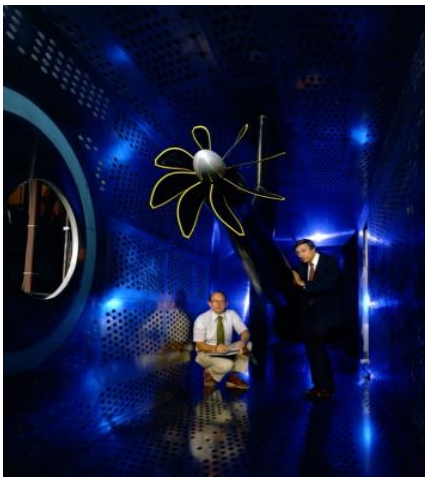

Figure 5: SR-7A propeller in the NASA Lewis wind tunnel [12]

One of the biggest uncertainties in acoustic scaling is that the addition or subtraction of decibels is purely based on observation and not even correlated empirically. The high cost associated with acquiring free flight test data makes the amount of information about scaling ground to flight methodology rare in the open literature and are often company proprietary and part of their competitive edge [2]. As a result, some caution needs to be exercised when scaling simulation results. In this thesis, only well-defined scaling will be used in noise level adjustments.

The only simulation effort of a NASA propeller blade was performed by De Gennaro et al. in 2010 on the SR-2 blade using ANSYS FLUENT [6]. They compared their aeroacoustic results with the experimental data presented in Dittmar [14] in cruise conditions. In this thesis, a similar effort will be conducted on the swept SR-7A propeller blades using another commercial code, STAR-CCM+. However, more extensive aerodynamic results will be produced. In addition to the power coefficient, the unsteady pressure coefficient at several blade locations will be analyzed and compared to experimental data.

An SR-7A blade has not been simulated using commercial code and discussed in literature before. The importance of this blade is that its geometry highly resembles the newly developed blades. The scarcity of this endeavor in literature makes this investigation valuable and enhances the use of commercial code for industrial applications. This tool will potentially serve as a very efficient tool for enhancement of designs due to its cost effectiveness as compared to the highly expensive iterative approach in wind tunnel testing.

1.3 Approach

The aim of this research is to perform a one-way coupled aerodynamic and acoustics simulation of the SR-7A propeller to address the issue of elevated noise levels. This project will split into two components: aerodynamics of the rotors and acoustic levels near the fuselage. The aerodynamics of the rotors will involve resolving the flow field around the rotors. Once that is accomplished, the acoustic levels will be computed using the acoustic analogy equations from the blade pressures and near-field perturbations.

For this project, STAR CCM+, commercial computational fluid dynamic software, will be used to resolve the flow field around the propeller. The results will be post-processed within STAR CCM+ to obtain the far-field noise levels at the fuselage using the Ffowcs-Williams and Hawkings equation. Validation of the results will then be performed by comparing the simulated results with the NASA wind tunnel testing data.

Due to the lack of extensive aerodynamic results for the SR-7A propeller and since predicting the appropriate physics for the aerodynamic component is necessary, the tandem, inline cylinder case is performed. Tandem, in-line cylinders is one of the most studied wake interaction problems. Its importance stems from the fact that the physics involved is applicable to a myriad of applications including aircraft landing gears, heat exchangers, etc. Even though, the application does not directly involve rotating bodies, the in-depth analysis performed by many researchers produced a very comprehensive data set that can be used for aero-acoustic simulation validation. As a result, this important problem was chosen before the simulation of rotating propellers was attempted to validate STAR-CCM+ as an appropriate simulation tool.

1.4 Thesis Outline

Chapter 2 introduces the numerical formulation the governing equations for fluid motion and the associated turbulence models used in this research. It also provides the acoustics formulation needed to estimate the noise generation. Chapter 3 discusses several processes that are used to develop and setup the simulation for turbomachinery. Chapter 4 and 5 displays two different simulation cases: tandem, inline cylinder case and SR-7A propeller case, respectively. Chapter 6 will provide the conclusions obtained from both simulations and the recommendations for future work.

Chapter 2

Numerical Formulation

2.1 Governing Equations of Motion

The basic equations of motion used to evaluate any flow problem are the continuity and momentum equations. Assuming no body forces, equations 1 and 2 show the compressible form of both equations, respectively.

$$\frac{\partial \rho}{\partial t} + \frac{\partial}{\partial x_i}(\rho u_i) = 0 \quad (1)$$

$$\frac{D(\rho u_i)}{Dt} \equiv \frac{\partial(\rho u_i)}{\partial t} + \frac{\partial}{\partial x_j}\left(\rho u_j u_i\right) = -\frac{\partial p}{\partial x_i} + \frac{\partial \tau_{ji}}{\partial x_j} \quad (2)$$

where, x_i (i = 1, 2, 3) are the Cartesian coordinates corresponding to (x, y, z). u_i is the Cartesian component of velocity, t is the time, p is the pressure, ρ is the density and τ_{ji} is the viscous stress tensor.

These equations form the basis for any fluid analysis. However, when turbulent flows are involved, more variables arise that cannot be solved due to the lack of equations. As a result, more equations are needed to resolve the turbulence closure problem.

2.2 Turbulence Modeling

This section will discuss the basis of the Reynolds Averaged Navier-Stokes (RANS) equations and the associated turbulence closure problem. The formulation of some turbulence models used in STAR-CCM+ simulations is also presented. These models are k-ω and its variation (k-ω SST), Large Eddy Simulation (LES), and Detached Eddy Simulation (DES). The advantages and disadvantages of each model are presented.

2.2.1 Reynolds-Averaged Navier-Stokes Modelling (RANS)

Reynolds-Averaged Navier-Stokes (RANS) equations deal with the unsteadiness of the flow in average terms. The flow variables are represented as a sum of two terms, a mean component and a fluctuating component, as shown in equation 3 and 4. Both equations represent the notation for the two different types of averaging – Reynolds averaging and Favre averaging, respectively.

$$u_i(x_i, t) = \bar{u}_i(x_i) + u_i'^{(x_i,t)} \quad (3)$$

$$u_i(x_i, t) = \tilde{u}_i(x_i) + u_i''^{(x_i,t)} \quad (4)$$

where, u_i' and u_i'' are the fluctuation about the averaged value for the different averaging types. There are two types of averaging used in order to solve $\bar{u}_i(x_i)$ in Reynolds averaging. One method is the time-averaged approach, shown in equation 5.

$$\bar{u}_i(x_i) = \lim_{T\to\infty} \frac{1}{T} \int_0^T u_i(x_i, t)\, dt \quad (5)$$

where, T is the averaging interval and is large compared to the typical time scale of the fluctuation. This is mainly used for steady flows.

For unsteady flows, another type of averaging is used – ensemble averaging. This concept involves the averaging of a large set of flows where all the variables are controlled and identical, but the initial condition for each flow is generated randomly. The mean flow under ensemble average is shown in equation 6, where N is the number of flows in the ensemble.

$$\bar{u}_i(x_i, t) = \frac{1}{N} \sum_{n=1}^{N} u_i(x_i, t) \quad (6)$$

Equations 5 and 6 are used for incompressible flows. For compressible flows, Favre averaging is used. It is defined as the density-weighted average with the fluid density denoted as $\rho(x_i\,, t)$. Equation 7 shows the solution for $\tilde{u}_i(x_i)$.

$$\tilde{u}_i(x_i) \equiv \frac{\overline{\rho u_i}(x_i\,, t)}{\bar{\rho}(x_i\,, t)} \quad (7)$$

Since this thesis is concerned with high speed, compressible flows, the Favre averaging will be utilized. After incorporating equation 4 and 7 into the equations of motion (equation 1 and 2) and then taking the Reynolds average, the Favre-averaged conservation of mass continuity and momentum are shown in equation 8 and 9.

$$\frac{\partial \bar{\rho}}{\partial t} + \frac{\partial}{\partial x_i}(\bar{\rho}\tilde{u}_i) = 0 \quad (8)$$

$$\frac{\partial(\bar{\rho}\tilde{u}_i)}{\partial t} + \frac{\partial}{\partial x_j}\left(\bar{\rho}\tilde{u}_j\tilde{u}_i\right) = -\frac{\partial \bar{p}}{\partial x_i} + \frac{\partial}{\partial x_j}\left(\bar{\tau}_{ji} - \overline{\rho u''_j u''_i}\right) \quad (9)$$

The term $\left(-\overline{\rho u''_j u''_i}\right)$ known as the Reynolds stress tensor, represents the apparent stress seen by the mean flow due to turbulent fluctuations. Its presence makes the turbulence problem difficult to solve due to the introduction of more unknown variables than available equations. The absence of additional equations is known as the Turbulence Closure Problem.

The Reynolds stress tensor cannot be solved in the same way the viscous stresses are. The reason behind this is that the viscous stress can be related directly to other flow properties using constitutive equations. This is possible because the closure approximations of a fluid are averaged over characteristic length and time scales that are much smaller than those of the flow we are interested in. At the same time, these scales are much larger than the molecular length and time scales that characterize the molecular interactions that cause momentum transfer. However, for Reynolds stress, it arises from the flow itself and the scales of the fluctuating motion of the flow are the scales we are interested in. As a result, the same closure concept from viscous stress will not work with Reynolds stress.

To close the system (to solve the turbulence closure problem), the Reynolds stress tensor needs to be modeled. One of the first people to tackle this problem is Boussinesq. He introduced the Boussinesq approximation with the model Reynolds stress tensor $\left(R_{ij}\right)$ replacing the exact Reynolds stress, as shown in equation 10.

$$R_{ij} = -\overline{\rho u''_j u''_i} \equiv 2\mu_t \tilde{S}_{ij} - \frac{2}{3}\bar{\rho}k\delta_{ij} \quad (10)$$

The eddy viscosity (μ_t) and the turbulent kinetic energy (k) would then be computed using the turbulence model to achieve turbulence closure. Even though this approximation is simple, it does provide the appropriate accuracy needed. It is fairly reasonable for simple shear flows where mean velocity gradients and turbulence develop slowly. The turbulence models needed for this thesis are discussed.

2.2.1.1 Standard k-ω model

The standard k- ω model is a two-equation model that solves two extra transport equations (turbulent kinetic energy, k and specific dissipation rate, ω) to account for the turbulence in the flow. This model was originally proposed by Wilcox [44]. Over time, various modifications have been introduced to it to account for compressibility, low-Reynolds number correction and a revised set of model coefficients.

The equations for k and ω are presented in equation 11 and 12, respectively.

$$\frac{\partial}{\partial t}(\bar{\rho}k) + \frac{\partial}{\partial x_j}(\bar{\rho}\tilde{u}_j k) = P_k - \beta^*\bar{\rho}\omega k + \frac{\partial}{\partial x_j}\left[\left(\bar{\mu} + \sigma^*\frac{\bar{\rho}k}{\omega}\right)\frac{\partial k}{\partial x_j}\right] \quad (11)$$

$$\frac{\partial}{\partial t}(\bar{\rho}\omega) + \frac{\partial}{\partial x_j}(\bar{\rho}\tilde{u}_j \omega) = \alpha\frac{\omega}{k}P_k - \beta\bar{\rho}\omega^2 + \sigma_d\frac{\bar{\rho}}{\omega}\frac{\partial k}{\partial x_j}\frac{\partial \omega}{\partial x_j} + \frac{\partial}{\partial x_j}\left[\left(\bar{\mu} + \sigma\frac{\bar{\rho}k}{\omega}\right)\frac{\partial \omega}{\partial x_j}\right] \quad (12)$$

The eddy viscosity (μ_t) is defined in equation 13.

$$\mu_t = \frac{\bar{\rho}k}{\hat{\omega}} \quad (13)$$

where,

$$\hat{\omega} = \max\left(\omega, C_{lim}\sqrt{\frac{2}{\beta^*}\tilde{S}_{ij}\tilde{S}_{ij}}\right)$$

$\beta^*, \beta, \alpha, \sigma^*$ and σ_d are calibration parameters, C_{lim} is the clip factor with a value of 10 for ω-based models and $\tilde{S}_{ij}$ is the modulus of the mean strain rate tensor.

2.2.1.2 k-ω SST model

Menter [35] introduced an alternative version to the original k-ω model. Both models looked similar with the exception that Menter's model contained an additional non-conservative cross-diffusion term. This addition allowed the model to produce similar results to another turbulence model (k-ε model). More information on the k-ε model is discussed in Jones & Launder [26].

With the proposed addition of a blending function that would be active only away from the wall, Menter's model would essentially be a k-ε model in the farfield and k-ω model near the wall. This combines the good characteristics of both models. It makes use of the major advantage of the k-ε model which is insensitive to the free-stream boundary conditions. At the same time, the shear-stress transport (SST) addition to the k-ω model modified the linear constitutive equation and made it possible to use the model to resolve viscous flows.

The two additional transport equations (k and ω) are shown in equation 14 and 15, respectively.

$$\frac{\partial}{\partial t}(\bar{\rho}k) + \frac{\partial}{\partial x_j}(\bar{\rho}\tilde{u}_j k) = P_k - \beta^*\bar{\rho}\omega k + \frac{\partial}{\partial x_j}\left[(\bar{\mu} + \sigma_k\mu_t)\frac{\partial k}{\partial x_j}\right] \quad (14)$$

$$\frac{\partial}{\partial t}(\bar{\rho}\omega) + \frac{\partial}{\partial x_j}(\bar{\rho}\tilde{u}_j \omega) = \alpha\frac{\omega}{k}P_k - \beta\bar{\rho}\omega^2 + 2(1-F_1)\sigma_{\omega 2}\frac{\bar{\rho}}{\omega}\frac{\partial k}{\partial x_j}\frac{\partial \omega}{\partial x_j} + \frac{\partial}{\partial x_j}\left[(\bar{\mu} + \sigma_\omega\mu_t)\frac{\partial \omega}{\partial x_j}\right] \quad (15)$$

P_k is the production rate of turbulence. Its value depends on which version of the k-ω SST model used ([33], [34], [35], and [37]). F_1 is the blending function and is shown in equation 16.

$$F_1 = \tanh(\arg_1{}^4) \quad (16)$$

$$\text{where,} \quad \arg_1 = \min\left(\max\left(\frac{\sqrt{k}}{0.09\omega d}, \frac{500\nu}{d^2\omega}\right), \frac{4\bar{\rho}\sigma_{\omega 2}k}{CD_{k\omega}d^2}\right)$$

Near the wall, the model behaves as a k-ω model with $F_1 = 1$. Far from the walls, the model behaves as a k-ε model with $F_1 = 0$. Using the value of F_1, the coefficients $\sigma_k, \sigma_\omega, \beta,$ and α can be solved using equations 17 – 20.

$$\sigma_k = F_1\sigma_{k1} + (1 - F_1)\sigma_{k2} \quad (17)$$

$$\sigma_\omega = F_1\sigma_{\omega 1} + (1 - F_1)\sigma_{\omega 2} \quad (18)$$

$$\beta = F_1\beta_1 + (1 - F_1)\beta_2 \quad (19)$$

$$\alpha = F_1\alpha_1 + (1 - F_1)\alpha_2 \quad (20)$$

$$\text{where,} \quad \alpha_1 = \frac{\beta_1}{\beta^*} - \sigma_{\omega 1}\frac{\kappa^2}{\sqrt{\beta^*}}; \quad \alpha_2 = \frac{\beta_2}{\beta^*} - \sigma_{\omega 2}\frac{\kappa^2}{\sqrt{\beta^*}}$$

$\sigma_{k1}, \sigma_{k2}, \sigma_{\omega 1}, \sigma_{\omega 2}, \beta_1, \beta_2,$ and κ are coefficients defined in the simulation software by default. In equation 16, d is the distance to the nearest wall, ν is the kinematic viscosity and $CD_{k\omega}$ is the positive part of the cross-diffusion term as shown in equation 21.

$$CD_{k\omega} = \max\left(2\bar{\rho}\sigma_{\omega 2}\frac{1}{\omega}\frac{\partial k}{\partial x_j}\frac{\partial \omega}{\partial x_j}, 0\right) \quad (21)$$

The k-ω SST model defines eddy viscosity (μ_t) as shown in equation 22.

$$\mu_t = \frac{a_1\bar{\rho}k}{\max(a_1\omega,\ \Omega F_2)} \quad (22)$$

where, a_1 is a calibration parameter. Ω is the magnitude of vorticity and is used to limit the production of turbulent kinetic energy at stagnation points due to the very high levels of shear strain rate. Ω will result in a small value because the deformation near a stagnation point is nearly irrotational. F_2 is another blending function that restricts the limiter to the wall boundary layer and is defined in equation 23.

$$F_2 = \tanh(\arg_2{}^2) \quad (23)$$

$$\text{where,} \quad \arg_2 = \max\left(\frac{2\sqrt{k}}{0.09\omega d}, \frac{500\nu}{d^2\omega}\right)$$

2.2.2 Advanced Approaches: LES and DES

Newer, more advanced turbulence modeling approaches have developed over the years in order to better simulate complex and real-life phenomena. These approaches are based primarily on unsteady, transient calculations and on average have higher computational costs than RANS models. The two approaches discussed in this section are large eddy simulation (LES) and detached eddy simulation (DES).

Large Eddy Simulation (LES)

Large Eddy Simulation (LES) is a transient approach that solves the large scales of turbulence and models the smaller scales. Therefore, by modelling less of the turbulence, this technique results in less error due to turbulence modeling. It is based on the idea that smaller eddies are self-similar thereby can be modeled with more universal models .

To achieve closure of the Navier-Stokes equations, the subgrid scale model is used to model the subgrid scale viscosity. The Boussinesq approximation is used to model the subgrid scale stresses. One major disadvantage of this model is that it is computational expensive. As a result, the detached eddy simulation (DES) was explored.

Detached Eddy Simulation (DES)

Detached Eddy Simulation (DES) is a non-zonal, hybrid approach that combines the features of the Reynolds Averaged Navier-Stokes (RANS) and Large Eddy Simulation (LES). The DES model was originally developed using the Spalart-Allmaras model before Menter & Kuntz [36] adopted the formulation to the k-ω SST model.

This approach has become well-known and proven for the prediction of massively separated flows at a lower computational cost than the LES model [43]. In this model, the dissipation term is modified, as shown in equation 24.

$$D_k = \beta^* \bar{\rho} \omega k \quad \rightarrow \quad D_k = \beta^* \bar{\rho} \omega k F_{DES} \quad (24)$$

The modification involves the addition of the F_{DES} term to distinguish between which model should be used. Equation 25 presents the definition of F_{DES} as a function of turbulent length scale (l_t) shown in equation 26, model constant (C_{des}), and the largest distance between the cell center under consideration and the cell centers of neighboring cells (Δ).

$$F_{DES} = \max\left[\frac{l_t}{C_{des}\,\Delta}, 1\right] = \begin{cases} 1, & if\ l_t < C_{des}\,\Delta \leftrightarrow RANS\ model \\ > 1, & if\ l_t > C_{des}\,\Delta \leftrightarrow LES\ model \end{cases} \quad (25)$$

$$l_t = \frac{\sqrt{k}}{\beta^* \omega} \quad (26)$$

The RANS model is employed in the regions near solid boundaries, where the turbulent length scale is less than the maximum grid dimension [41]. When these conditions are not in play, the

dissipation term in the k equation increases which in turn decreases k. As a result, the turbulent eddy viscosity decreases and the modelled dissipation decrease. This process resolves rather than models a large part of the turbulence, the concept of the LES subgrid scale model [29].

The formulation of the DES model is very helpful in reducing the computational cost while allowing the small-scale length scales to be resolved. This model will be used in the tandem, inline cylinder simulation as a test for its effectiveness.

2.3 Computational Aeroacoustics (CAA)

2.3.1 Background

Aeroacoustics is the study of noise generation that develops from turbulent fluid motion or though the interaction of flow and surfaces (aerodynamic forces). This field originated by Sir James Lighthill [30] where he studied the noise generation associated with jet engines. Since that time, this field has grown immensely until the 1980s when computational aeroacoustics (CAA) was developed.

Computational aeroacoustics is the subset of aeroacoustics that utilizes numerical methods to analyze noise generation. There are two methods that can be used under CAA: direct method and hybrid method. The direct method involves computing the flow and acoustic fields using the same computational domain using computational fluid dynamic equations. A large domain would be setup to include the receivers within and the mesh would have to be fine enough throughout the entire domain to prevent any dissipation. This is necessary in order to account for the large differences in length scale between the acoustic and the flow variables. As a result, the method is computationally expensive and impractical.

The alternative approach, hybrid method, splits the flow domain from the acoustic domain. The flow variables will be solved using the computational fluid dynamic equations. The flow field will then be used to calculate the acoustical sources, which in turn is used to propagate noise to the receiver location using an acoustic analogy. This allows the domain to be much smaller and reduces the computational cost significantly.

The hybrid approach is the basis for all commercial software including STAR-CCM+. The next two sections discuss the acoustic analogy developed by Lighthill and its modification to include moving surfaces referred to as Ffowcs Williams-Hawkings (FW-H) equation.

2.3.2 Lighthill's Acoustic Theory

Lighthill [31] introduced one of the simplest yet powerful concepts into the aeroacoustic world, known as the acoustic analogy. The purpose, at the time, was to understand and predict the noise generation by the jet of an aircraft turbojet engine. The idea of the acoustic analogy is to replace the regions of unsteady fluid flow by an equivalent distribution of sources in order to derive

linear perturbations from the base flow [31]. The formation of the analogy is based on manipulating the momentum and mass continuity equation to obtain a linear wave equation with nonlinear forcing terms that are independent of the far-field radiation.

In order to derive the acoustic analogy, consider a jet of air streaming into a quiescent medium with density ρ_0 and speed of sound c. Away from that jet, the perturbation pressure p' can be written in the wave equation form as shown in equation 27.

$$\blacksquare^2 p' = \frac{1}{c^2}\frac{\partial^2 p'}{\partial t^2} - \nabla^2 p' = 0 \quad (27)$$

Lighthill derived an exact relation for perturbation density (p') as shown in equation 28.

$$p' = c\rho' \quad (28)$$

Manipulating the mass continuity and momentum equations in [1] and [2], we get a rearranged combined equation shown in equation 29.

$$\frac{\partial^2 \rho'}{\partial t^2} = \frac{\partial^2}{\partial x_i \, \partial x_j}\left(\rho u_i u_j + P_{ij}\right) \quad (29)$$

Subtracting $\frac{\partial^2 p'}{\partial x_i^2}$ from both sides of equation 29 and using equation 28, we get an equation of the same form of equation 27 as shown in equation 30.

$$\blacksquare^2 p' = \frac{\partial^2 T_{ij}}{\partial x_i \, \partial x_j} \quad (30) \quad \text{where, } T_{ij} = \rho u_i u_j + P_{ij} - c^2 \rho' \delta_{ij}$$

In equation 30, T_{ij} is referred to as the Lighthill turbulence stress tensor. It is equal to zero at the far-field, thereby satisfying the definition in equation 27. However, its value is not equal to zero in the jet and acts as a quadrupole noise source that radiates sound in a radial direction [31].

2.3.2 Ffowcs Williams-Hawkings (FW-H) equation

The Ffowcs Williams-Hawkings (FW-H) equation is the generalization form of Lighthill's acoustic analogy (equation 23) and is derived primarily from Farassat's Formulation 1A [16]. It is the exact rearrangement of the generalized derivatives of the continuity and momentum equations into the form of the inhomogeneous wave equation.

To understand the formulation, consider a moving, impenetrable body described by $f(\mathbf{x}, t) = 0$, such that $f > 0$ is outside the body and $\nabla f = \hat{\boldsymbol{n}}$ (outward normal to $f = 0$). Inside the body, the fluid is at rest and with the same conditions as the formulation of Lighthill's acoustic analogy. Based on this setup, there is an artificial discontinuity at the body $(f = 0)$. To take into account the jump present at the surface, the mathematical concept of derivatives of generalized functions is used to make the required corrections to the conservation laws. The generalized conservation

laws of mass continuity and momentum are shown in equation 31 and 32, respectively. The bars over the derivatives denote generalized differentiation.

$$\frac{\bar{\partial}\rho'}{\partial t} + \frac{\bar{\partial}}{\partial x_i}(\rho u_i) = \rho_o v_n \delta(f) \quad (31)$$

$$\frac{\bar{\partial}}{\partial t}(\rho u_i) + \frac{\bar{\partial}}{\partial x_j}\left(\rho u_i u_j + P_{ij}\right) = l_i \delta(f) \quad (32)$$

where, $v_n = -\frac{\partial f}{\partial t}$ is the local normal velocity at the surface of the body, $l_i = P_{ij} n_j$ is the local force intensity that acts on the fluid, and $\delta(f)$ is the Dirac delta function. Taking the $\frac{\partial}{\partial t}$ of equation 31 and $\frac{\partial}{\partial x_i}$ of equation 32, and subtracting the result of the latter from the former, we get to equation 33.

$$\frac{\bar{\partial}^2\rho'}{\partial t^2} - \frac{\bar{\partial}^2}{\partial x_i\, \partial x_j}\left(\rho u_i u_j + P_{ij}\right) = \frac{\bar{\partial}}{\partial t}[\rho_o v_n \delta(f)] - \frac{\bar{\partial}}{\partial x_i}[l_i \delta(f)] \quad (33)$$

Substituting equation 28 into equation 33 and subtracting $\frac{\partial^2 p'}{\partial x_i \partial x_j}$ from both sides provides the general form of the FW-H equation as shown in equation 34.

$$\blacksquare^2 p' = \frac{\partial}{\partial t}[\rho_o v_n \delta(f)] - \frac{\partial}{\partial x_i}[l_i \delta(f)] + \frac{\bar{\partial}^2}{\partial x_i\, \partial x_j}\left[T_{ij}\, H(f)\right] \quad (34)$$

where, $H(f)$ is the Heaviside function. Using the free-space Green's function [16] to compute the sound pressure at the observer's location *x*, the solution of equation 34 can be formulated in the form shown in equation 35.

$$p'(\vec{x}, t) = p'_T(\vec{x}, t) + p'_L(\vec{x}, t) + p'_Q(\vec{x}, t) \quad (35)$$

$p'_T(\vec{x}, t)$ refers to the monopole (or thickness) term. It arises from the displacement of the fluid as the body passes through. $p'_L(\vec{x}, t)$ is the dipole (or loading term). It occurs from the unsteady motion of the force distribution on the body surface. Both of these noise sources are surface-related. Finally, $p'_Q(\vec{x}, t)$ is the quadrupole (volume source) term and results from the non-linearities present in the flow.

There are two types of surfaces that can be used in the formulation. An impermeable FW-H surface acts as a filter of wall boundary conditions from which the noise originates. This type will produce sound levels only from the monopole and dipole sources. A permeable FW-H surface acts as a filter of internal interface boundaries. This surface is a fine mesh region that surrounds all the sources of noise: monopole, dipole, and quadrupole.

In STAR-CCM+, FW-H model uses a concept developed by Brentner and Farassat [4] referred to as the advanced time approach or the source-time-dominant approach. The algorithm looks forward in time to see when the receiver perceives the generated sound waves. This advanced time algorithm makes a distinction between the emission and reception times. The emission times of the acoustic signal from each surface will be constant while the reception time for those signals will be different. As a result, the emission times are fixed and the signals arriving to the receiver are accumulated at their respective emission time slot. The overall acoustic signal at the receiver is the summation of the individual acoustic signal from each source surface during the same emission time.

The goal of FW-H model is to predict the small amplitude acoustic pressure fluctuations at the location of the desired receiver. It predicts the propagation of sound in free space using analytical integral solution to the generalized wave equation and does not include any effects such as reflections and refractions. This approach is used in the simulations performed in this thesis to predict noise levels of the receivers in the farfield.

Chapter 3

Simulation Processes in STAR-CCM+

3.1 Motion Techniques for Turbomachinary

This section discusses the numerical methods STAR-CCM+ employs to perform simulation on a rotating body. There are two approaches: Moving Reference Frame (MRF) and the Sliding Mesh (SLM). Both methods involve manipulating the equations of motion into the rotating frame in different ways.

3.1.1 Moving Reference Frame

Moving Reference Frame (MRF) method involves rewriting the time-averaged, steady-state form of the Navier-Stokes equations in a moving frame. For a rotating frame with constant rotational speed, the equations are transformed into a rotating frame to get a steady-state solution. It does not take into account any unsteady components of the flow field, thereby serving as a preliminary solution to unsteady problems. However, its versatility and low CPU demand makes it in widespread use in the turbomachinery industry.

Consider a coordinate system rotating at an angular velocity $\boldsymbol{\omega}$ relative to the stationary reference frame as shown in Figure 6. The origin of the rotating system is located a position vector $\boldsymbol{r_o}$ with $\boldsymbol{r}$ being the position of an arbitrary point from the origin of the rotating frame

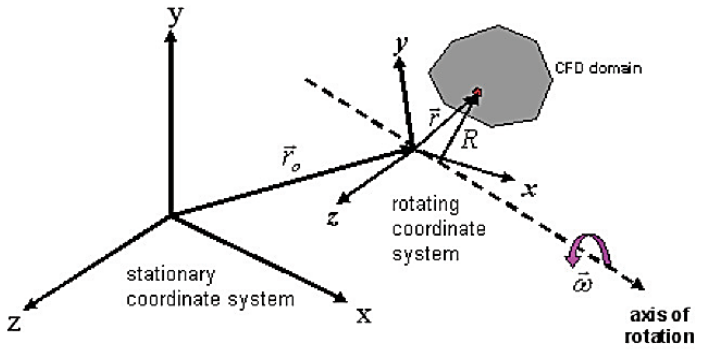

Figure 6: Rotating coordinate system in a moving reference frame [6]

To transform the equations of motion, the fluid velocities are written in a rotating frame, as shown in equation 36.

$$\boldsymbol{v_r} = \boldsymbol{v} - (\boldsymbol{\omega} \times \boldsymbol{r}) \quad (36)$$

where, $\boldsymbol{v_r}$ is the relative velocity viewed from the rotating frame and $\boldsymbol{v}$ is the absolute velocity viewed from the stationary frame. Using equation 36, the mass continuity and momentum equations are rewritten into equation 37 and 38, respectively.

$$\frac{\partial \rho}{\partial t} + \nabla \cdot \rho \boldsymbol{v_r} = 0 \quad (37)$$

$$\frac{\partial}{\partial t}(\rho \boldsymbol{v_r}) + \nabla \cdot (\rho \boldsymbol{v_r} \boldsymbol{v_r}) + \rho(2\omega \times \boldsymbol{v_r} + \boldsymbol{\omega} \times \boldsymbol{\omega} \times \boldsymbol{v_r}) = -\nabla p + \nabla \cdot \boldsymbol{\tau} \quad (38)$$

Two additional acceleration terms (Coriolis acceleration and centripetal acceleration) are introduced to the momentum equation. The remaining components of the equations remain consistent with the stationary frame Navier-Stokes equations except with the introduction of the relative velocity.

3.1.2 Sliding Mesh

Sliding Mesh (SLM) approach involves accurate time-dependent simulations where the unsteady interactions of the fluid flow are considered. This approach involves setting one grid domain inside the computational domain with a relative motion with respect to the adjacent grid domain. However, in order for the code to be able to transport fluid variables between both grid domains, an interface zone is introduced to perform the interpolation.

At every time step, the unsteady RANS equations are solved in each cell zone and the fluxes are calculated across the faces over the interface. However, at the next time step, the grid domain with a relative motion will move to a new location and the grid points are no longer aligned. This will require the interface zone to perform interpolation in order to transfer the fluxes between the two grid domains. This happens at every time step and hence makes this approach computationally highly demanding.

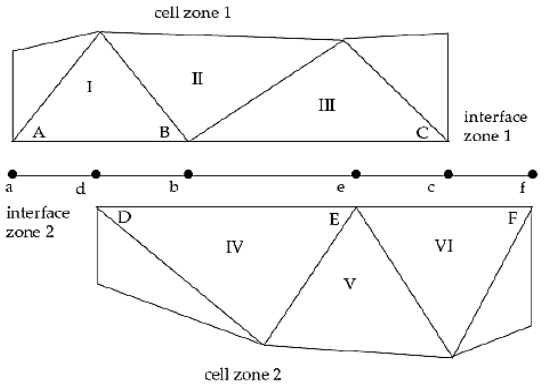

Figure 7: Sliding mesh between domains with different relative motions [6]

Figure 7 shows two grid domains with different relative motions. The intersection between the cell zones produces the faces *a-d*, *d-b*, *b-e*, *e-c*, and *c-f*. Sections where the cells overlap (*d-c*) form the interior zone. To compute the fluxes through Cell III, face B-C is ignored because the

grid points in cell zone 2 are not aligned with cell zone 1. In this case, the interface zone is used, and faces *b-e* and *e-c* are used to transport the information from Cell IV and VI, respectively.

3.2 Meshing Techniques

Meshing is one of the most integral pre-processing steps in performing a simulation. It consists of dividing up a domain into smaller cells, where the equations of motion are solved and the fluxes propagate. The type of mesher used and the quality of the generated mesh determine how accurate the results would be.

There is always a trade-off between the number of cells generated and the resulting computational time. Ideally, a dense mesh would produce the most accurate results. However, the computational time required to reach a solution would be large. On the other hand, a coarse mesh would take less time to solve, but will not provide accurate solutions. Therefore, knowing what type of mesher would be a good fit for the type of problem being solved is critical.

This section discusses a selection of meshers used in this thesis that STAR-CCM+ offers. It also discusses how STAR-CCM+ evaluates the quality of the mesh in order to allow the user to adjust the mesh parameters to reach a desired quality.

3.2.1 Types of Meshers

STAR-CCM+ has various built-in meshers to satisfy every purpose. The meshers discussed in the section are: polyhedral mesher, trimmer cell mesher, and the prism layer mesher. The method of each mesher generation along with the reasons of its choice in simulations is presented.

3.2.1.1 Polyhedral Mesher

The polyhedral meshing model uses arbitrary polyhedral cell shapes to build the core mesh, as shown in Figure 8. The quality of the polyhedral mesh depends on the initial surface preparation. Using a special dualization scheme, it is automatically created from an underlying tetrahedral cell-shaped surface mesh in STAR-CCM+. The resulting polyhedral cell has an average of 14 cells. Even though a tetrahedral mesh option is present in STAR-CCM+, polyhedral mesh is relatively more efficient to build, generating five times fewer cells than a tetrahedral mesh for a given starting surface.

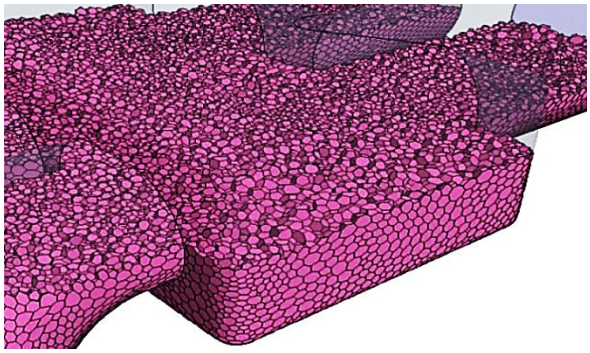

Figure 8: Polyhedral volume mesh of an arbitrary shape [5]

3.2.1.2 Trimmer Cell Mesher

The trimmer cell mesher is an efficient and robust model that is used to produce high quality grids. It is a hybrid meshing technique that combines a few highly desirable meshing properties in a single scheme. The trimmer meshing technique makes use of a template mesh constructed from hexahedral cells. From that template, the mesher 'trims' the required core mesh utilizing the starting geometry as reference. The resulting mesh is composed predominantly of hexahedral cells with trimmed cells close to the surface, as shown in Figure 9. These trimmed cells are polyhedral cells with one or more corners/edges cut off.

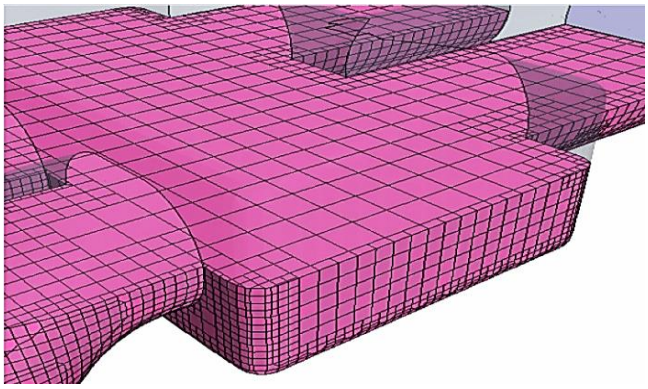

Figure 9: Trimmer volume mesh of an arbitrary shape [5]

The trimmer mesher primarily produces cells with minimal skewness that is independent of the initial surface quality. It also provides the ability to align the cells in any user specified coordinate system which minimizes errors. Due to these two major advantages, this type of mesher is used in the simulations of this thesis.

3.2.1.3 Prism Layer Mesher

Prism layer mesher is a complimentary model that is typically used after other volume meshers to generate orthogonal prismatic cells next to wall surfaces or boundaries. It is assigned by specifying its thickness, number of cell layers, the size distribution of the layers and the function that is used to generate the distribution. The number of prism layers is usually chosen depending on the turbulence model, wall functions, and Reynolds number of the flow. Figure 10 shows a volume mesh with two prism layers near wall surface.

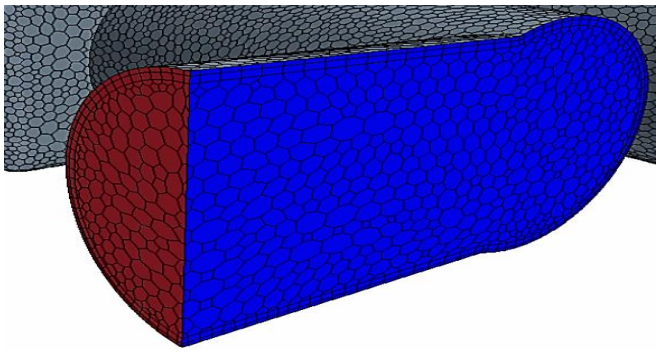

Figure 10: Prism layer mesh along the edge of the domain [5]

When the prism layer mesher is chosen, a subsurface is generated at the user specified prism layer thickness before the core volume mesh is developed. Using this subsurface, the core mesh is constructed by the any of the chosen volume meshers. The next step involves generating the prism layer mesh by extruding the cell faces from the generated core mesh (from subsurface) to the original starting surface.

The prism layer concept is used extensively in the simulations in this thesis for a couple reasons. This technique produces high-aspect ratio cells close to the wall, thereby providing better cross-stream resolution without sacrificing much of the stream-wise resolution. The near-wall mesh density reduces numerical diffusion (discretization error that smears discontinuities and steep gradients in a finite volume advection scheme) near the wall. This helps the solver resolve near-wall flow and the forces on walls accurately.

3.2.2 Evaluating Mesh Quality

Mesh quality is one of the most important checks that need to be performed before a simulation is started. A valid mesh is one that allows a solution to be achieved after it is initialized and run successfully. Even though a mesh can be valid and no errors exist in its generation, a poor mesh quality could negatively impact the solution data. There are five parameters that STAR-CCM+ uses to evaluate the quality of the meshes to insure that the flow phenomenon is not compromised.

Skewness angles of the cell are very important criteria. STAR-CCM+ has two skewness angles: cell skewness angle and boundary skewness angle. Cell skewness angle is designed to see whether the cells on either side of the face are formed in a way to permit diffusion quantities, without these quantities becoming unbounded. Figure 11 displays the skewness angle θ between the vector connecting the centroids of two adjacent cells **ds** and the normal vector **a** from the face between both cells. Each cell stores the worst skewness angle of all its faces.

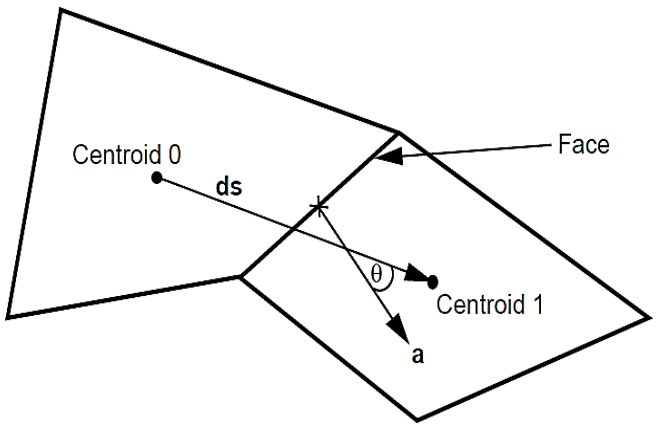

Figure 11: Sketch of the cell skewness angle [5]

An angle of zero corresponds to a perfectly orthogonal mesh, while an angle of 90 degrees or more (present in concave cells where both centroids lie on same side of boundary face) typically result in solver convergence issues. To make sure the robustness of data is not affected, the skewness angles will be monitored and the worst value should be lower than 85 degrees.

Boundary skewness angle is defined as the angle between the area vector and the vector connecting the cell centroid and the boundary face centroid, as shown in Figure 12. Boundary face skewness is important for laminar flows and heat transfer in solids but become less important in turbulent flows, where wall functions are used. Because all y+ wall treatment is employed in the simulations, this parameter will not be essential in this thesis.

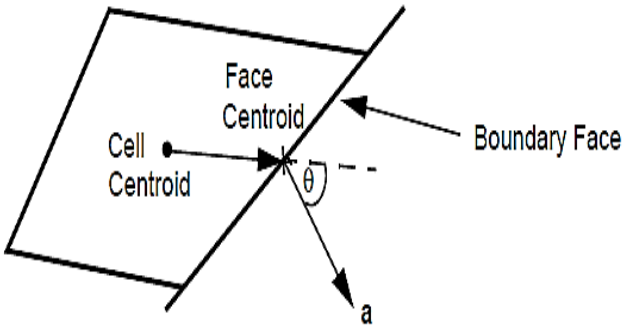

Figure 12: Sketch of the boundary skewness angle [5]

Face validity is an area-weighted measure of the correctness of the face-normal relative to their attached cell centroid, as shown in. In a good quality cell (face validity of 1.0), the face normals are correctly pointing outward, away from the cell centroid, shown in in Figure 13a. Values below 1.0 (Figure 13b) indicate some sort of concavity with some cell faces having normal pointing inward towards cell centroid. Values below 0.5 indicate the presence of negative volume cells. This will be an essential parameter to monitor during the development of the mesh.

a) **b)**

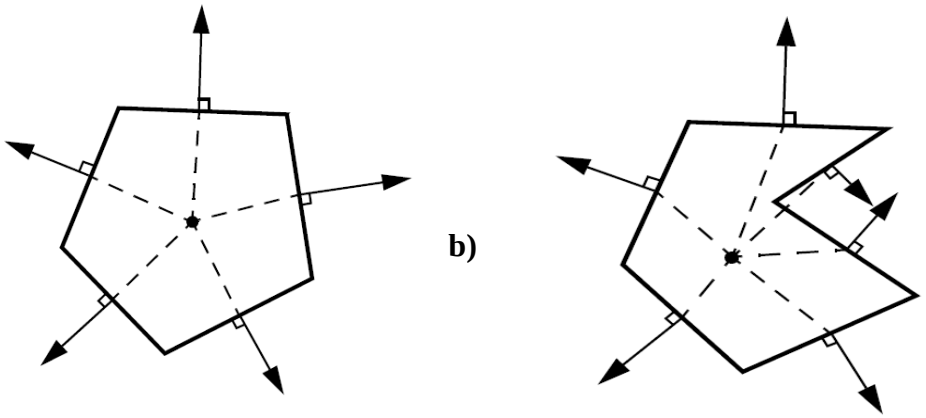

Figure 13: Face Validity of a cell a) Good cell; b) Bad cell [5]

Cell quality metric is a function of the orientation of cell faces and the relative geometric distribution of the cell centroids of the face neighbor cells. The algorithm used for cell gradient calculation is based on the hybrid of the Gauss and the least-squares methods.

A cell quality of 1.0 (Figure 14a) is considered a perfect cell whereas a degenerate cell has a cell quality approaching zero. Even though a poor quality cell quality (flat cells with highly non-orthogonal faces as shown in Figure 14b) can still be used to produce a solution, the robustness and accuracy of that solution is compromised. This parameter will be monitored during the development of the mesh.

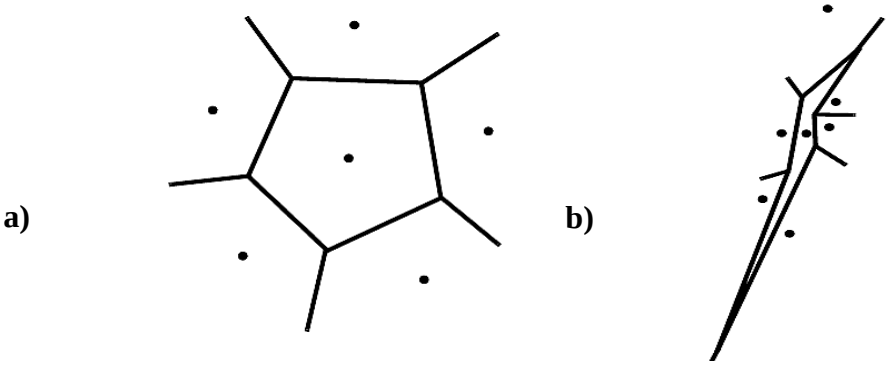

Figure 14: Cell quality a) Good cell; b) Bad cell [5]

Volume change metric is the ratio of the volume of a cell to that of its largest neighbor as shown in Figure 15. This metric is used to flag cells of decreasing cell volume relative to its neighbors. An abrupt change in the volume of one cell to another could cause instabilities and inaccuracies in the solver. This parameter will be monitored during the development of the mesh. A value higher than 1 E-05 is recommended. Any value of 1 E-05 or lower will be investigated and most likely adjusted.

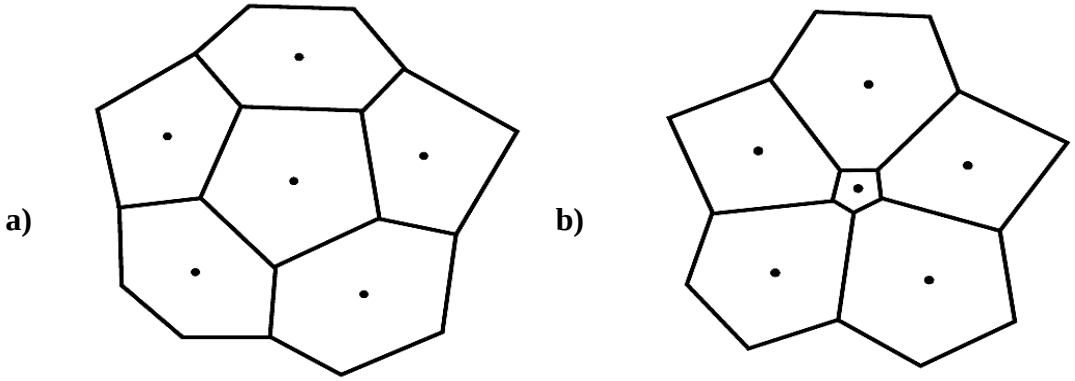

Figure 15: Volume change a) Good cell; b) Bad cell [5]

Chapter 4

Tandem, Inline Cylinder Case

Tandem, in-line cylinders is one of the most studied wake interaction problems. Its importance stems from the fact that the physics involved is applicable to a myriad of applications including aircraft landing gears, heat exchangers, etc. Even though, the application does not directly involve rotating bodies, the in-depth analysis performed by many researchers produced a very comprehensive data set that can be used for aeroacoustic simulation validation. As a result, this important problem was chosen before the simulation of rotating propellers was attempted to validate STAR-CCM+ as an appropriate simulation tool.

4.1 Background Overview

Both aerodynamic and acoustical experiments were performed on the tandem cylinder case to understand how the noise generation by bluff body wake interference occurs. The ultimate goal for all the experimentation and simulation is to design new, quiet technology.

4.1.1 Experimentation

Zdravkovich [48] was one of the first to research the tandem cylinder case. He classified the flows as a wake interaction problem and classified the type of wake interaction as a function of the separation distance between the cylinders. His experiments involved changing the distance between the upstream and downstream cylinder and analyzing the effect.

He noticed that vortex shedding from upstream cylinder is suppressed when the cylinders are close to one another. However, as the separation distance increased, the flow phenomenon changed. The upstream shear layer reattachment occurred first on the downstream cylinder and was followed by the development of the vortex shedding behind upstream cylinder. On the time domain, the impingement of the wake behind the upstream cylinder on the downstream cylinder creates high amplitude unsteady forces and intense radiated noise. This feedback loop continues as the separation distance becomes large enough for reattachment of the flow to happen on the downstream cylinder.

Jenkins et al. [25] performed two tandem cylinder experiments in the Basic Aerodynamic Research Tunnel (BART) as shown in Figure 16. The BART is an open-return wind tunnel used to perform experiments to explore complex flow field in subsonic and atmospheric conditions. It is located in the NASA Langley Research Center with the closed test section being 28 inches

high, 40 inches wide and 10 feet long [1]. The maximum operating Mach number is 0.17 corresponding to a maximum test section velocity of 185 feet per second (unit Reynolds number of 1.13 million per foot). Before the airflow enters into the test section, it passes through a honeycomb panel, four anti-turbulence screens, and an 11-to-1 contraction ratio in order to condition the flow's streamwise turbulence intensity to a level below 0.08%. The test model can be either mounted on the inbuilt support system in the tunnel or on the floor, ceiling, or sidewalls (after tunnel configuration).

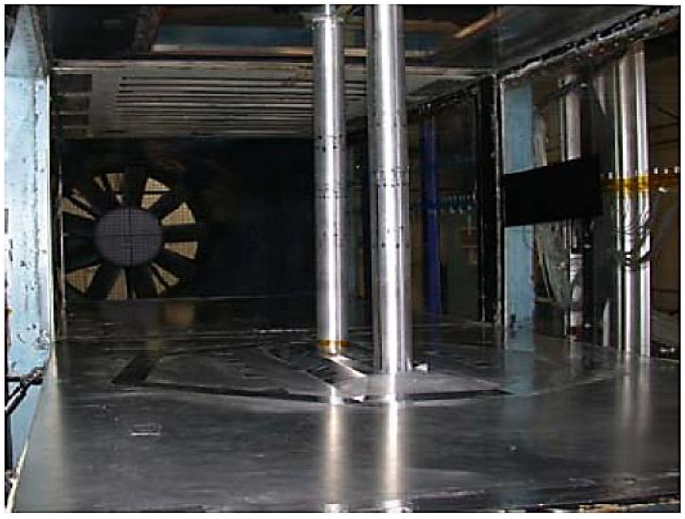

Figure 16: Tandem cylinder arrangement in Basic Aerodynamic Research Tunnel [1]

Using the dimensions of the BART, Jenkins et al. [25] installed two cylinders (D = 0.05715 m) with a separation distance (L) equivalent to 3.7D (spanning the height of the tunnel) in a free-stream velocity of 44 m/s to achieve a Reynolds number of 166,000 based on cylinder diameter. The free-stream turbulence level is less than 0.10%. At an azimuthal angle between 50 and 60 degrees from the leading stagnation point, the boundary layer on the upstream cylinder was tripped to ensure a fully turbulent shedding process. Theta (θ) is the angle measured positively in clockwise direction measured from the stagnation point on upstream cylinder as shown in the Figure 17.

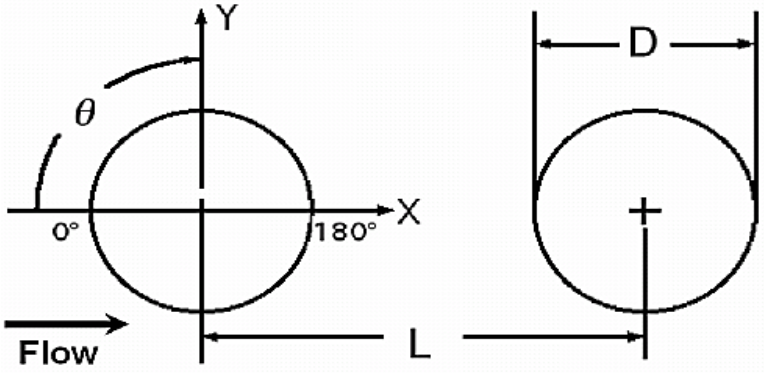

Figure 17: Tandem cylinder configuration [32]

Another group of researchers, Hutcheson and Brooks [23], performed experimentation on the tandem cylinder case in the Quiet Flow Facility (QFF) tunnel to understand the wake development as well as the radiated noise shown in Figure 18. The QFF is a 9.1m x 6.1m x 7.6m high anechoic open-jet facility located at NASA Langley Research Center, designed primarily for acoustic testing [1]. It is equipped with a 2-ft x 3-ft rectangular open jet nozzle with a maximum Mach number of 0.17 as well as flow-circuit turbulence screens and turning vanes to produce low turbulence air inflow. The free jet leaves the facility through an acoustically treated exhaust port in the ceiling. The facility is equipped with a small aperture directional array as well as a 2D array of 1/8-inch microphones for acoustical measurements. The anechoic room is mounted on springs to isolate it from any structure-borne vibrations that could be transmitted from the building.

Figure 18: Tandem cylinder arrangement in Quiet Flow Facility (QFF) [1]

Hutcheson and Brooks [23] used the same conditions in the QFF experiment as in the BART experiment conducted by Jenkins et al. The same trip arrangement on the upstream cylinder was also performed. The span (b) of cylinders are 3 ft (0.914 m) corresponding to an aspect ratio of b/D = 16. The nominal Mach number at 0.1274 (equivalent to 43.4 m/s) which was achieved by changing the speed in the tunnel to the shedding frequency is matched. The dynamic pressure is 0.166 psi (1145 Pa).

In addition to the aerodynamic results that both wind tunnels generated, the QFF provided valuable acoustical data. Three 1/8” microphones were mounted around the center of the span away from the jet flow. Table 1 defines the microphone locations in (x,y) coordinates and Figure 19 shows the schematic of the microphones with respect to the tandem cylinders.

Table 1: Location of microphones

Microphone	Location
A	(-8.33D, 27.815D)
B	(9.11D, 32.49D)
C	(26.55D, 27.815D)

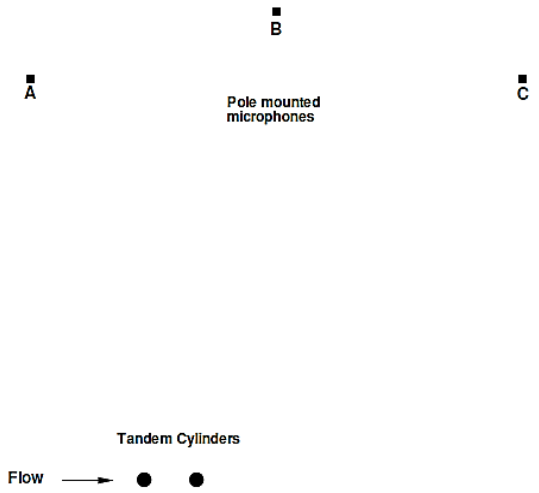

Figure 19: Schematic of microphone locations with respect to tandem cylinders [32]

For both experiments, a 64-channel, 16 bit transient data recorder controlled by a workstation was used to acquire data at a sampling rate of 25.6 kHz. High pass and low pass filters set at 5 Hz and 10 kHz were used to condition the outputs for the microphones. The noise spectra were obtained by partitioning each time signal into 1000 non-overlapping signals of 8192 segments. Each time history segment was Fourier transformed using the Hamming window for signal conditioning producing a frequency resolution of 3.125 Hz.

4.1.2 Simulations

To complement the experimental efforts, other researchers focused on performing simulations of the tandem cylinder case in an attempt to match aerodynamic and acoustic experimental results. These efforts involved both two-dimensional (2-D) and three-dimensional (3-D) simulations using various turbulence models.

Khorrami et al. [27] were one of the first research groups to perform simulations on the tandem cylinder case. They started with a 2-D, fully turbulent simulations using a standard, Unsteady Reynolds Averaged Navier-Stokes (URANS) equations in addition to Menter's Shear Stress Transport (SST) model. Two separation distances of L/D = 1.435 and 3.7 were simulated where L is the separation distance between both cylinder centroids and D is the cylinder diameter.

As noticed by Zdravkovich [48], at short separation distances less than 2.4, the two cylinders act as one single bluff body and shedding occurs behind downstream cylinder. At larger separation distances, both cylinders exhibit shedding.

The results obtained were satisfactory and captured some of the flow physics associated with this problem. However due to the shortcomings of the 2-D simulations and its inability to capture all the wake dynamics, some details like the mean streamwise velocity were not matched. They noticed that strong shedding were produced without any small scale vortices and concluded that this was due to the overly diffusive nature of the URANS model.

To solve those issues with two-dimensionality and turbulence model, Khorrami et al. [28] extended their model to 3-D and used a hybrid-zonal turbulence model which turns off turbulence production term everywhere except close to the cylinder walls. To minimize computational cost of the simulation, the spanwise extent of the cylinders was set to 3 cylinder diameters. The three-dimensionality of the flow was observed and the results were improved when compared to the 2-D simulations.

Lockard et al. [32] performed similar 3-D simulations as the ones performed by Khorrami et al. [28] with the addition of acoustical results. They used a three-dimensional Navier-Stokes solver CFL3D developed by NASA Langley Research Center (LaRC). Similar quasi-laminar approach described by Khorrami et al. [28] was used as the turbulence model. To account for the trip mechanism that was employed in the experiments, they ran the simulations in a fully turbulent mode and allowed it to transition on its own. They also explored the effect of the grid resolution and spanwise extent of the domain on the flow and the noise generation. The results concluded that the downstream cylinder dominated the noise radiation and the full length of the model span (16 cylinder diameters) captured the flow dynamics thereby producing good noise radiation levels.

Doolan [15] performed a 2-D, incompressible URANS simulation of the tandem cylinder case with the separation distance of 3.7 using an open source software called OPENFOAM. Some discrepancies were noticed between the experimental and simulation flow data. However, that was attributed to the lack of the spanwise velocity component in the simulation. On the other hand, the acoustical results matched well with the tone at the first harmonic.

Brès et al. [3] performed the simulations of the tandem cylinder case using the lattice Boltzmann method. They set up two cases: one with the use of spanwise periodic boundary configuration and another using the exact setup and geometry in the QFF experiment. Both simulations were using the spanwise dimension of 16 cylinder diameters. Overall, both cases provided good results in terms of the flow and noise predictions. However, the presence of the side walls (to support the experimental test model) improved the tonal peak amplitude compared to the periodic boundary condition. An increase of 1-2 dB was noticed on the harmonics and 2-3 dB on the broadband due to the wall reflections.

4.2 Computational Aspects

Figure 20 shows the computational domain along the midplane along with the dimensions of the domain. The diameter (D) of both cylinders is 0.05715 meters and the spanwise distance is 3D.

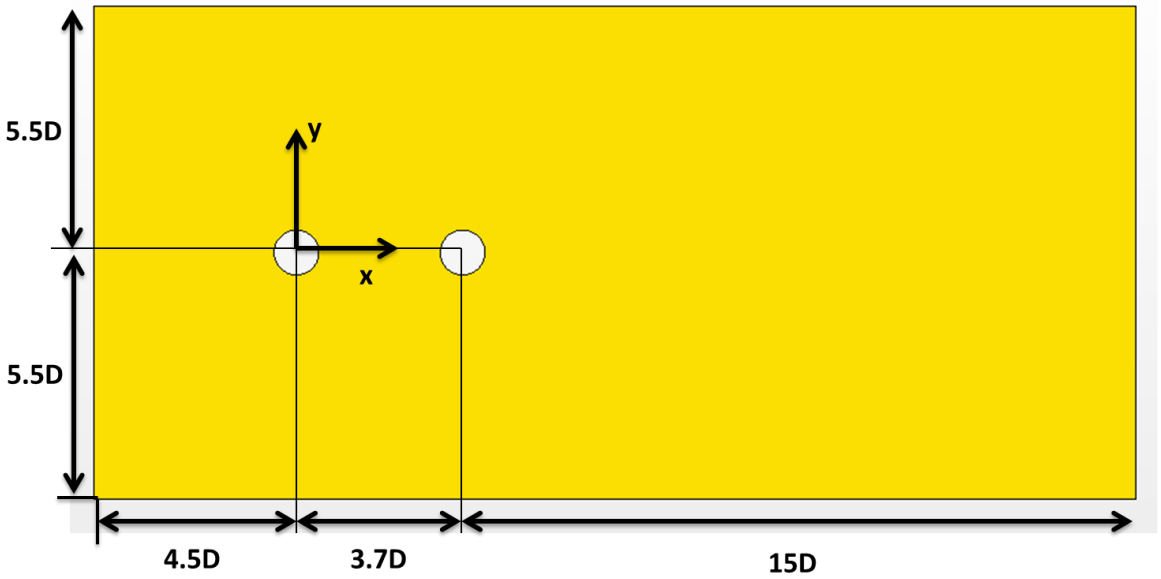

Figure 20: Computational domain of the tandem cylinder case

Table 2 lists the boundary conditions used along the surfaces of the domain. Table 3 lists the meshing parameters used in the simulation and Figure 21 (a, b, c) shows the mesh of the domain, zoomed view of the mesh around the two cylinders, and the mesh along the span of the domain, respectively.

Table 2: Boundary conditions of the tandem cylinder case

Boundary	Type	Value
Inlet	Free-stream	M = 0.128 Re # = 166,000
Outlet	Pressure Outlet	0 Pa
Two Cylinders	Wall	No – Slip smooth
Top and Bottom	Free-stream	M = 0.128 Re # = 166,000
Front and Back	Periodic	-

Table 3: Meshing parameters for the tandem cylinder case

Parameters	Values
Number of Cells	1,917,269
Mesher Type	Trimmer & Prism Layer Mesher
Number of Prism Layers	20
Prism layer thickness	0.0080 m
Thickness of near wall prism layer	1.0 E-5 m
Maximum Y+	1.39

a)

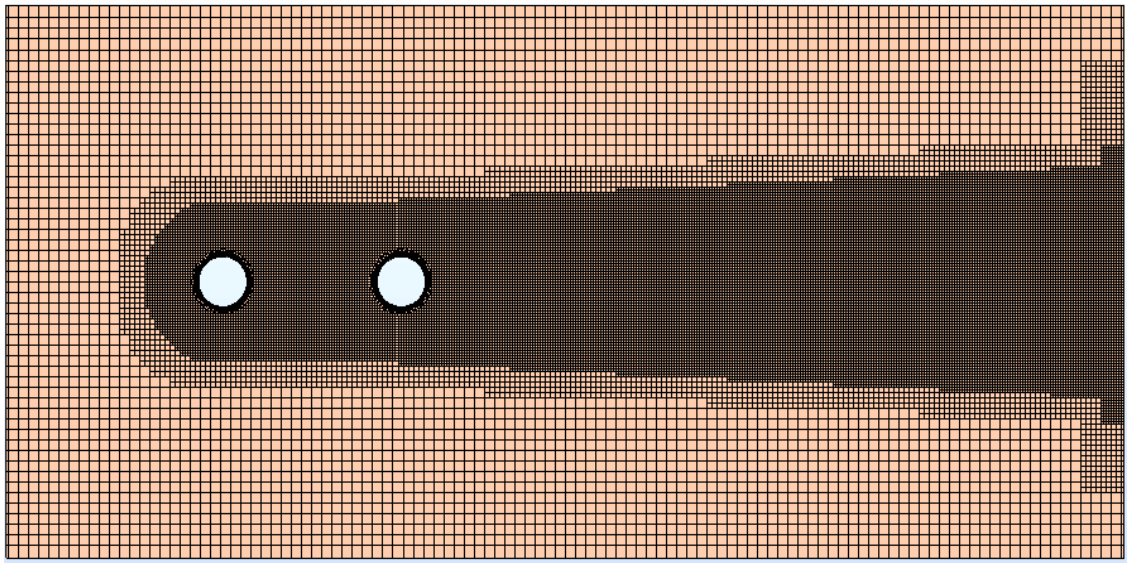

b)

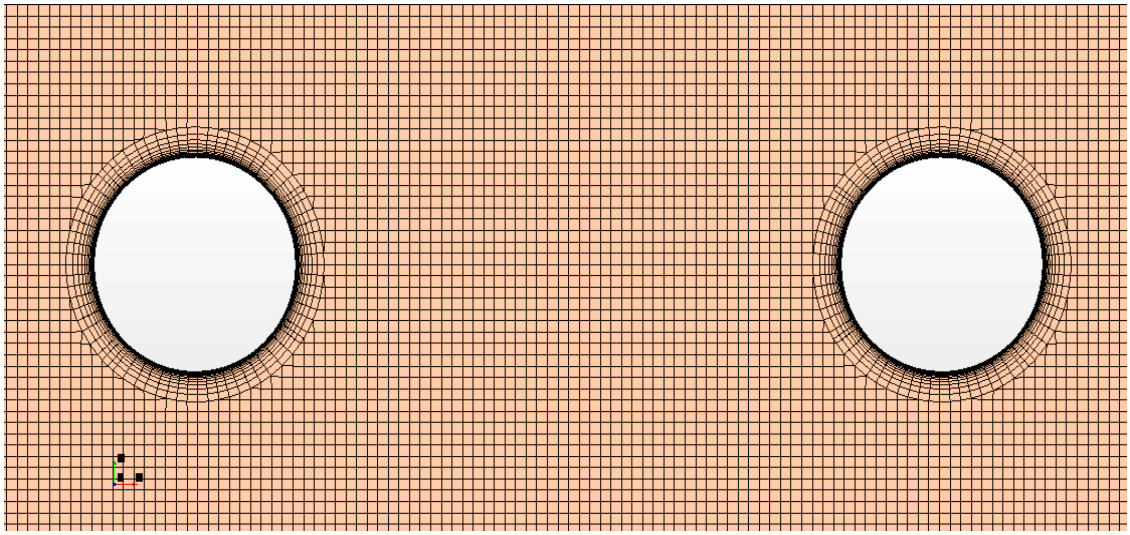

c)

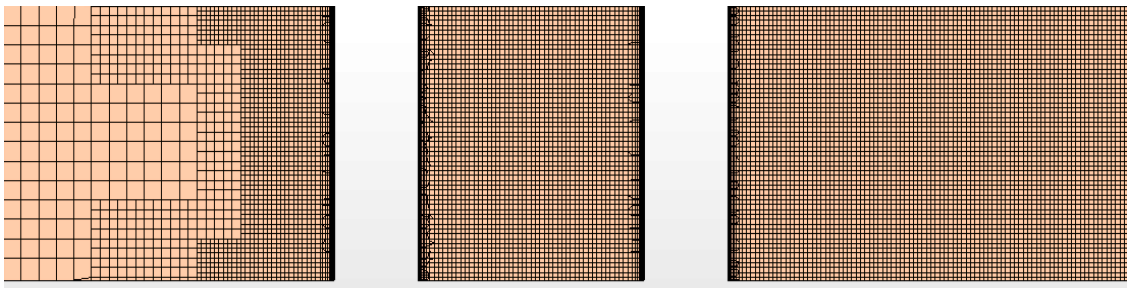

Figure 21: a) Mesh of the tandem cylinder domain; b) Zoomed view of mesh around both cylinders; c) Mesh along the spanwise direction of the domain

As shown in Figure 21, the mesh was refined around the cylinders and in the wake region behind both cylinders. This is required in order to capture the wake dynamics of the flow as well as to keep the y+ value less than 1. Figure 22 shows the y+ values on the span of the cylinder walls. The maximum value of y+ is 1.4. Even though it is greater than 1, it is an acceptable value to get

reasonable results without increasing the mesh cell numbers and computational cost. An all y+ wall treatment is used in the simulation which also justifies the why the mesh size is reasonable.

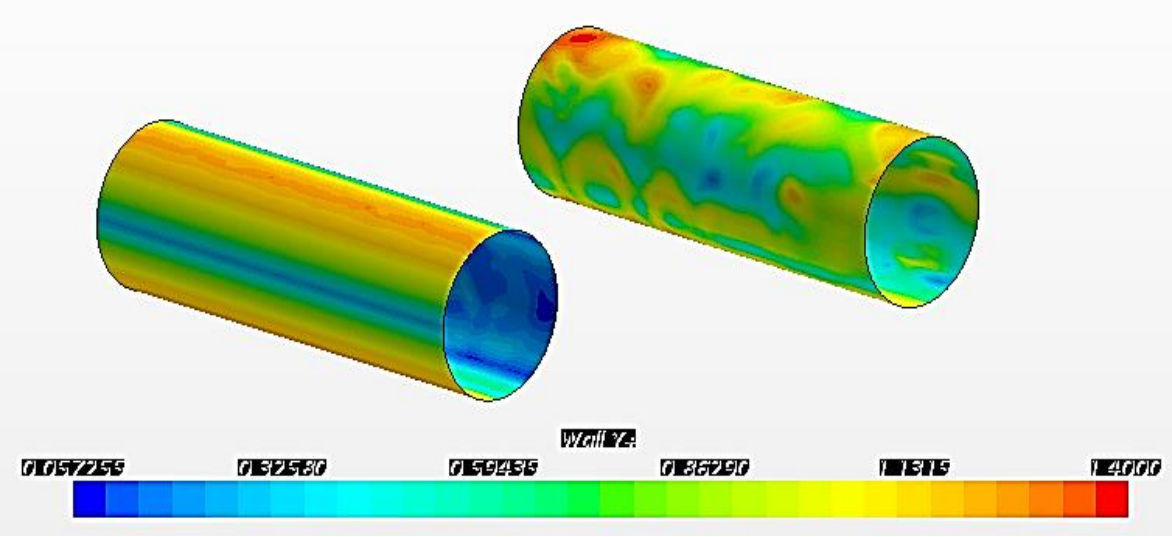

Figure 22: Y+ values on the cylinder wall

Table 4 and Table 5 list the physics model and the stoppage criteria used in the simulation of the tandem cylinder case, respectively. A steady simulation was initially run until convergence using the k-ω SST model in order to improve the initial conditions and speed up convergence in the unsteady calculation.

Table 4: Physics parameters for the tandem cylinder case

Parameter	Value
Turbulence Model	Detached Eddy Simulation (DES) with Menter's k-ω SST
Wall Treatment	All y+ wall treatment
Flow Regime	Turbulent Flow
Equation of State	Ideal Gas
Acoustics Model	Ffowcs Williams-Hawkings (FW-H)

Table 5: Stoppage criteria for the tandem cylinder case

Parameter	Value
Timestep size	1.0 E-5 s
Temporal Discretization	2nd order
Iterations per timestep	25
Number of timesteps	15,000

The microphones (x, y) positions are inputted into STAR-CCM+ at the same locations discussed in the QFF experiments shown in Table 1 and Figure 19. The z (spanwise) position of the microphones was set to be along the midspan. Impermeable surface of the upstream and

downstream cylinder were used to obtain the acoustical data at the microphones. Table 6 shows the computational cost for the tandem cylinder simulation.

Table 6: Computational cost of the tandem cylinder simulation

Parameters	Value
Total run time	0.15 s
Total wall clock time	115.17 hrs
Number of CPU	100
Wall clock time per timestep	27.64 sec

4.3 Aerodynamic Analysis of Results

Figure 23 shows the instantaneous density contour around the cylinders. It can be seen that the Kelvin-Helmholtz type instabilities grow on the shear layer extending from the cylinders. Eventually, the shear layers roll-up forming the shedding frequency. However, the roll-up is irregular and inconsistent, sometimes forming a strong vortex while being weak at other times. A similar behavior can be observed in the lift and drag coefficients for the upstream and downstream cylinder shown in Figure 24a and Figure 25a, respectively. The lift and drag coefficients are shown after the 5000th timestep to remove any transient effects and continue until the end of the simulation at 15,000th timestep. Lockard et al. [32] observed a similar behavior in their simulation as shown in Figure 24b and Figure 25b even after running it for more simulation time (equivalent to 30,000 timesteps).

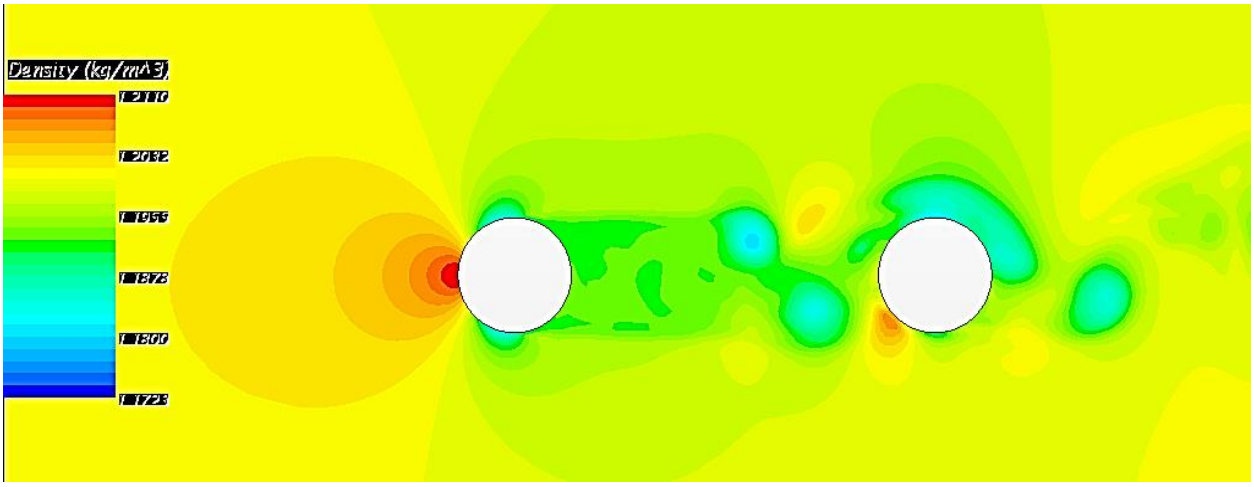

Figure 23: Instantaneous density contour around the cylinders

The lift and drag coefficients were calculated using the equation 39 and 40, respectively with the area (A) being the diameter multiplied by the span of the cylinder/domain.

$$C_L = \frac{Lift}{\frac{1}{2}\rho {U_o}^2 A} \qquad (39)$$

$$C_D = \frac{Drag}{\frac{1}{2}\rho {U_o}^2 A} \qquad (40)$$

a)

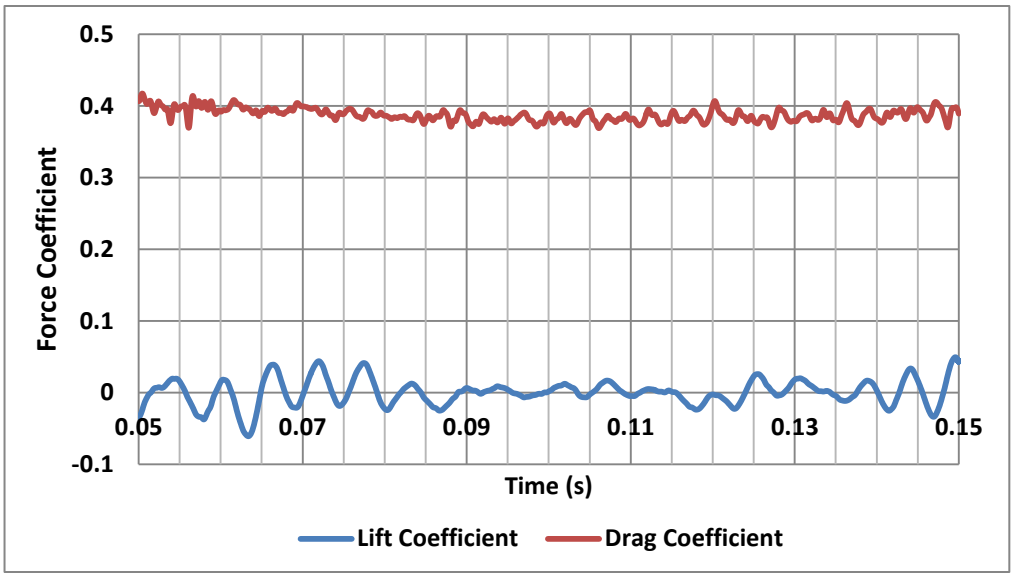

b)

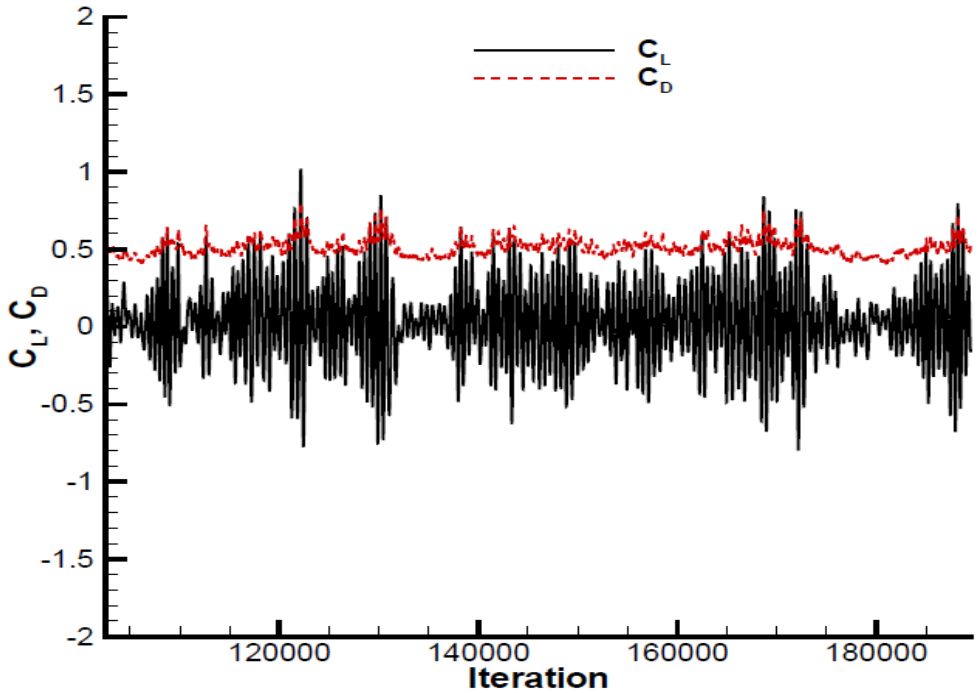

Figure 24: Lift and Drag Coefficient for Upstream Cylinder; a) Time history using STAR-CCM+ b) Results based on Lockard et al. [32]

a)

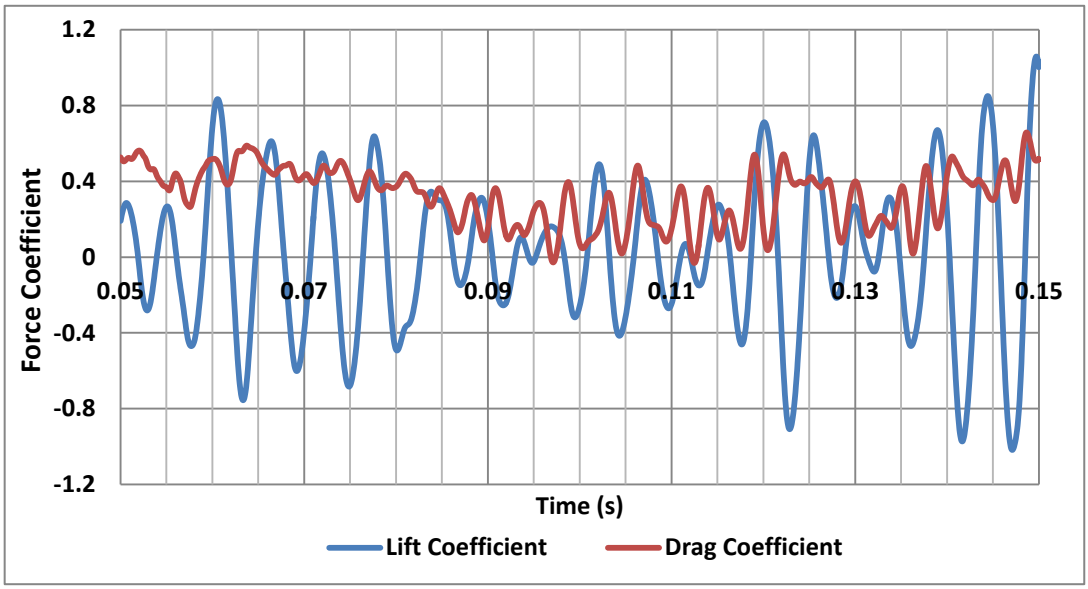

b)

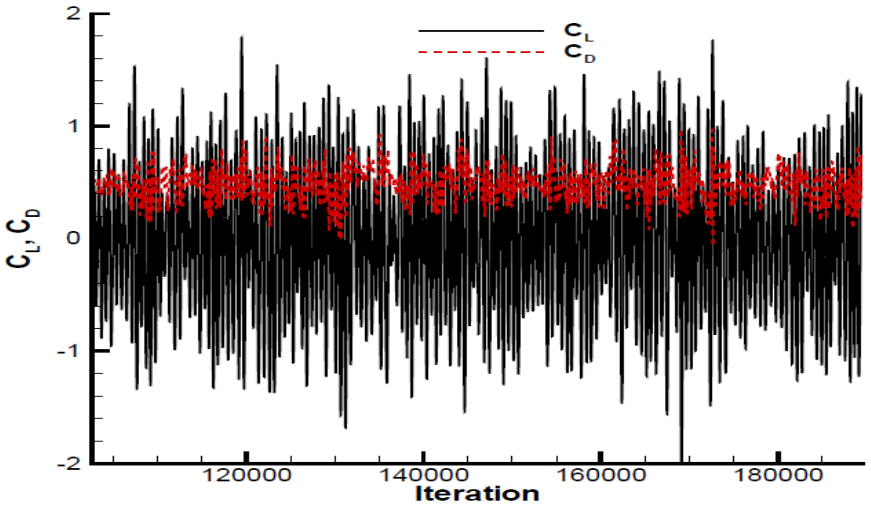

Figure 25: Lift and Drag Coefficient for Downstream Cylinder a) Time history on STAR-CCM+ b) Results based on Lockard et al. [32]

The drag coefficient for both cylinders oscillates around 0.4 with the downstream cylinder having higher amplitude of oscillations. This observation is also consistent in the lift coefficient with the mean being around zero. This is consistent with Lockard et al. [32] results shown in Figure 24b and Figure 25b. Figure 26 (a & b) shows the velocity contour plot along the midspan plane and the zoomed in view around the cylinders. Similar to the density plot in Figure 23, the shear layers emanate from the upstream cylinder and cause a separation between the high velocity and low negative velocity. That pressure gradient causes this separation and causes the roll-up to occur close to the downstream cylinder as shown in Figure 27.

a)

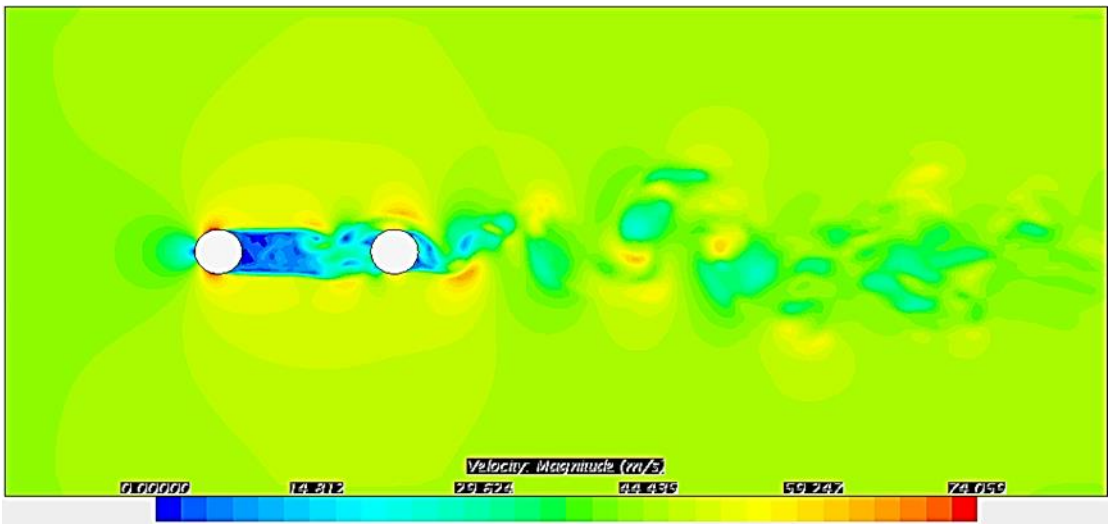

b)

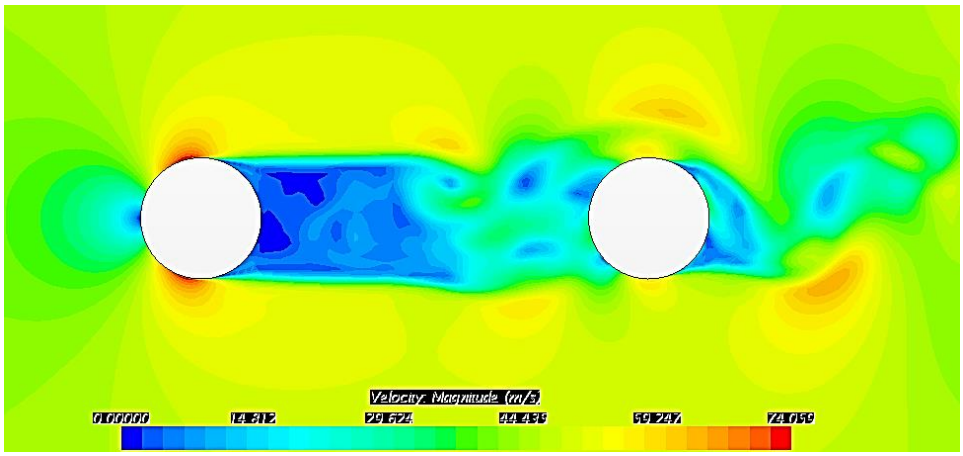

c)

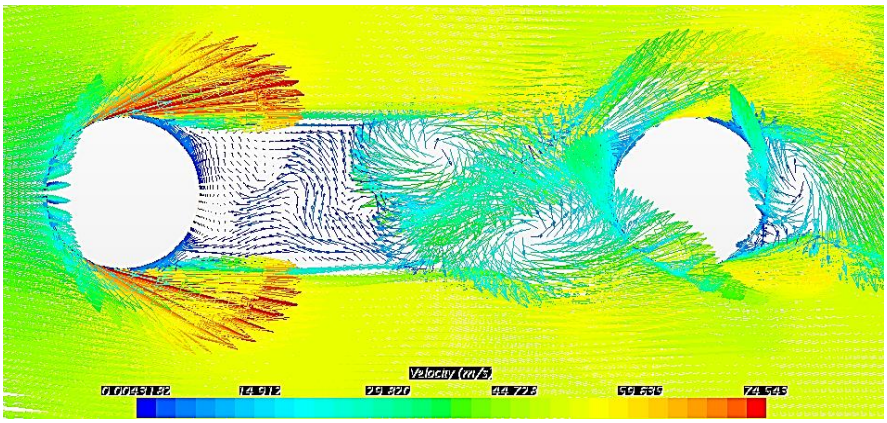

Figure 26: a) Instantaneous velocity plot along the midspan plane; b) Zoom around the tandem cylinders; c) vector plot around the tandem cylinders

Figure 26 (c) shows the vector plot of around the tandem cylinders. There is negative close-to-stagnant flow behind the upstream cylinder. After that region, two vortices occur in front of the downstream cylinder each with opposite rotational orientation. This is fully explained by both

the streamwise adverse pressure gradient and the simultaneously favorable pressure gradient along the crossflow direction.

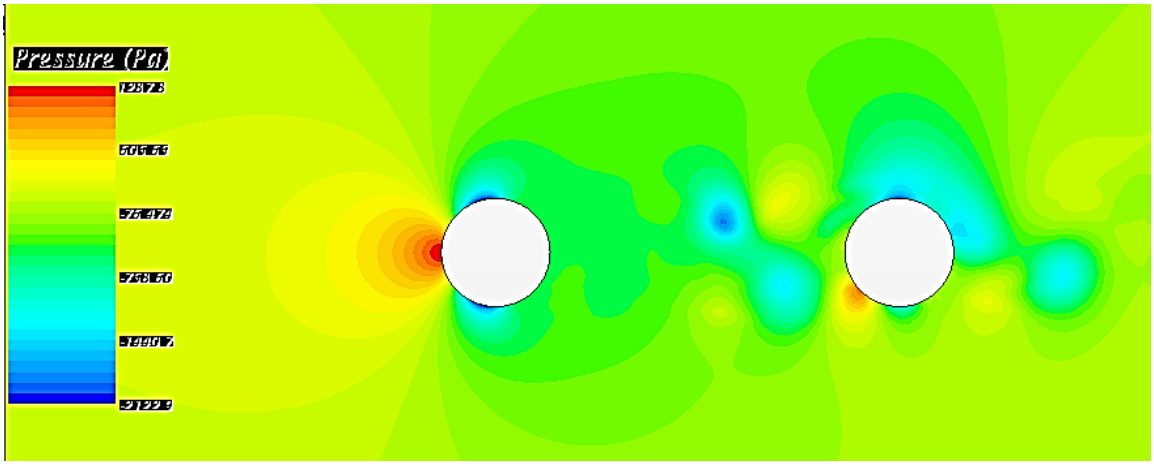

Figure 27: Pressure contour of the tandem cylinder case

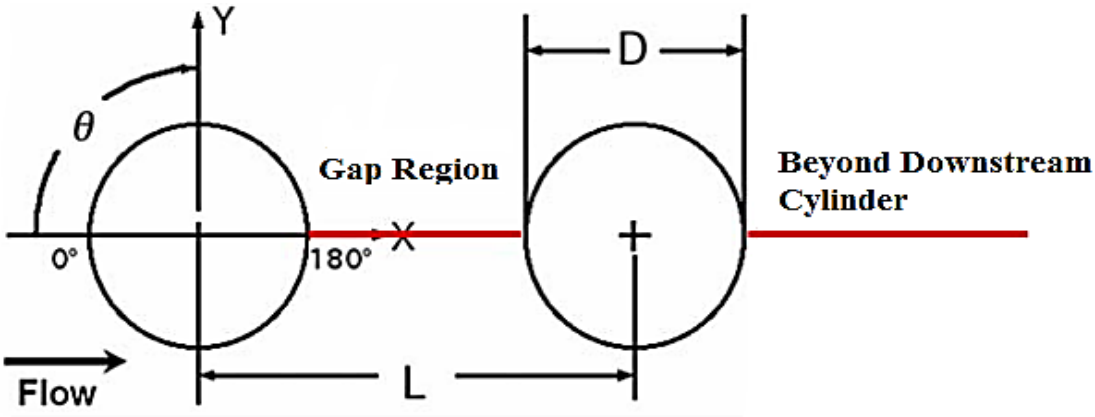

Figure 28: Sketch of the regions of interest for streamwise velocity and turbulent kinetic energy comparison [32]

Figure 29 shows the time-averaged mean streamwise velocity along the gap region between the two cylinders and beyond the downstream cylinder as shown in the sketch in Figure 28. U_o is defined as the free-stream velocity and is equivalent to 44 m/s. The results were time-averaged over 15,000 timesteps. Compared to the BART experimental results and the simulation results presented by Lockard et al. [32] in Figure 30, the flow at the gap region follows the same trend but magnitude of the scaled velocity is way off. This suggests that the flow in the gap region has not developed fully yet due to the high entrainment rate of flow in that region. However, the region beyond the downstream cylinder matches the experimental results more closely with a slight over-estimation at around 5.25D.

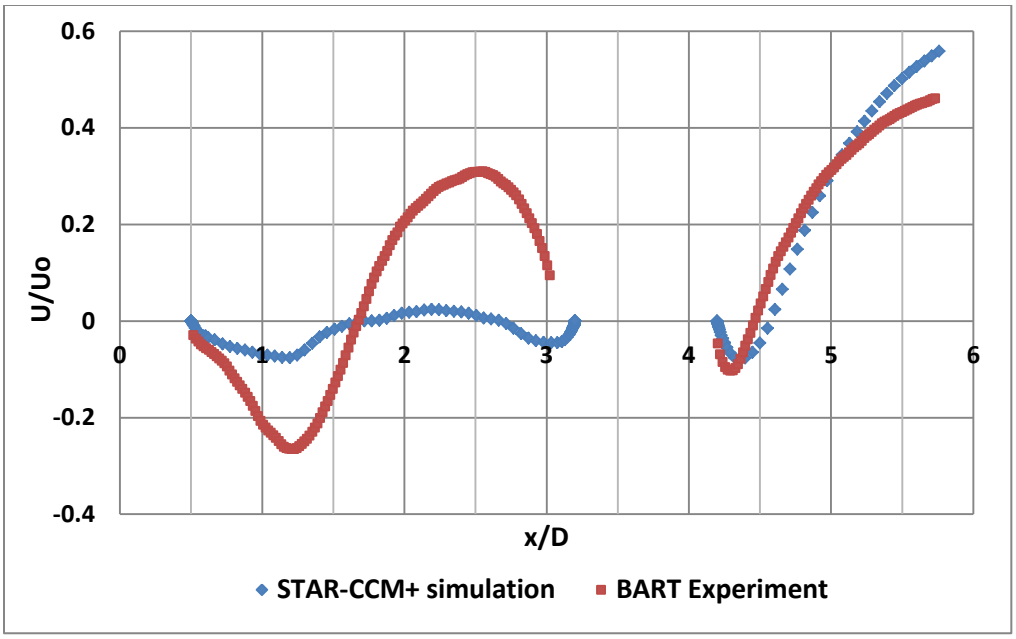

Figure 29: Mean streamwise velocity at gap region (left) and beyond downstream cylinder (right) on z = 0 plane

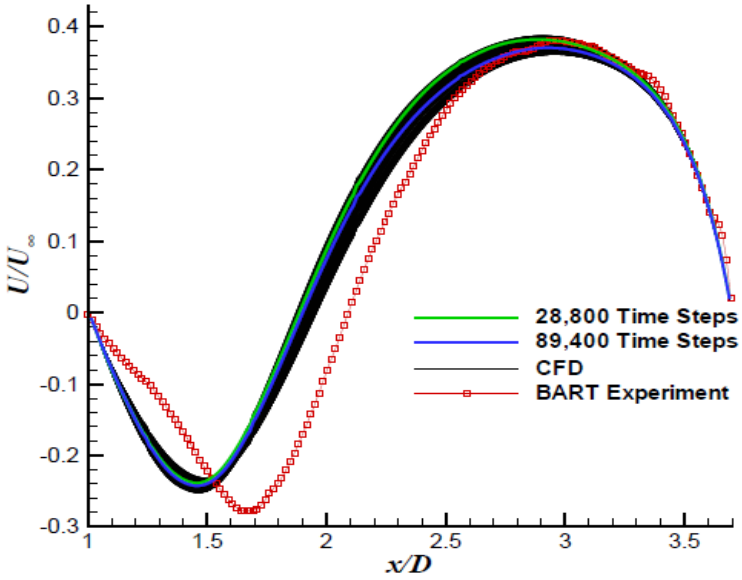

Figure 30: Mean streamwise velocity at the gap region from simulation by Lockard et al. [32]

Figure 31 displays the 2-D mean turbulent kinetic energy (tke) at the gap region and beyond the downstream cylinder as shown in the sketch in Figure 28. It can be seen that the simulation results match the BART experimental results towards the beginning and end of the gap region. The simulation results are also underestimated. However, beyond the downstream cylinder, the simulation results match the experimental results up to 4.5D followed by an overestimation of the simulation results. The trend of the simulation results is in good agreement with the BART experiments.

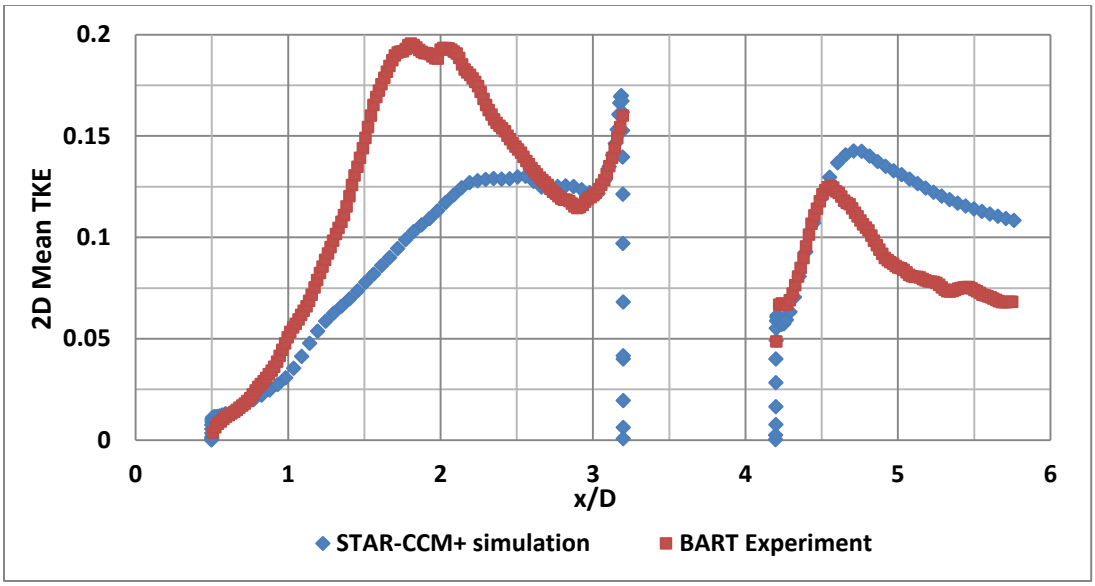

Figure 31: 2-D mean turbulent kinetic energy (tke) at the gap region (left) and beyond downstream cylinder (right) along z = 0 plane.

Figure 32 and Figure 33 shows the mean pressure coefficient (C_p) along the upstream and downstream cylinder with the angle (θ) measured clockwise from the stagnation point as shown in Figure 28.

It can be seen that the mean pressure coefficient on the upstream cylinder matches the results from the BART and QFF experiments relatively well. The flow separation took place at around 75° in the simulation compared to 80° in the experiments. This difference affects the flow in the gap region and beyond the downstream cylinder. This has been observed and discussed in Figure 29. Lockard et al. [32] noticed that if the separation point occurs before it should, the wake that develops behind the upstream cylinder would attach to the downstream cylinder. This would make both cylinders act as a single bluff body with wake happening only beyond downstream cylinder. Given the delayed roll-up of the wake behind the upstream cylinder, it suggests that even a 5° difference in the separation point would totally affect the flow downstream.

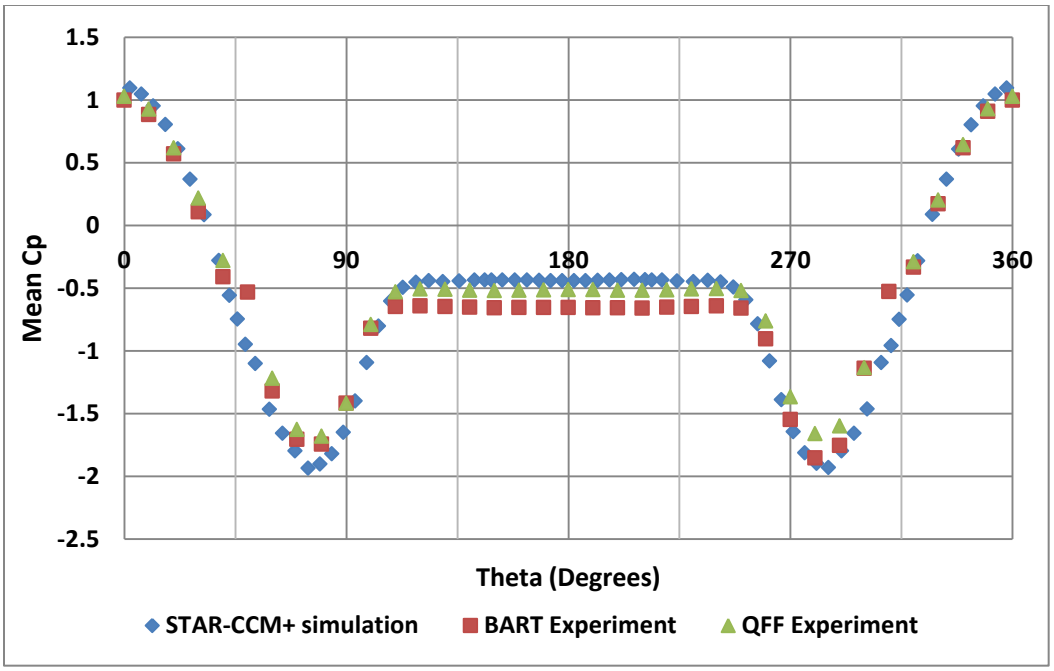

Figure 32: Mean pressure coefficient (C_p) of upstream cylinder

As expected, the mean pressure coefficient on the downstream cylinder (Figure 33) would not match the results of the BART and QFF experiments. There is an underestimation on the first 45°, followed by an overestimation between 135° and 225°, and finally an underestimation between 315° and 360°.

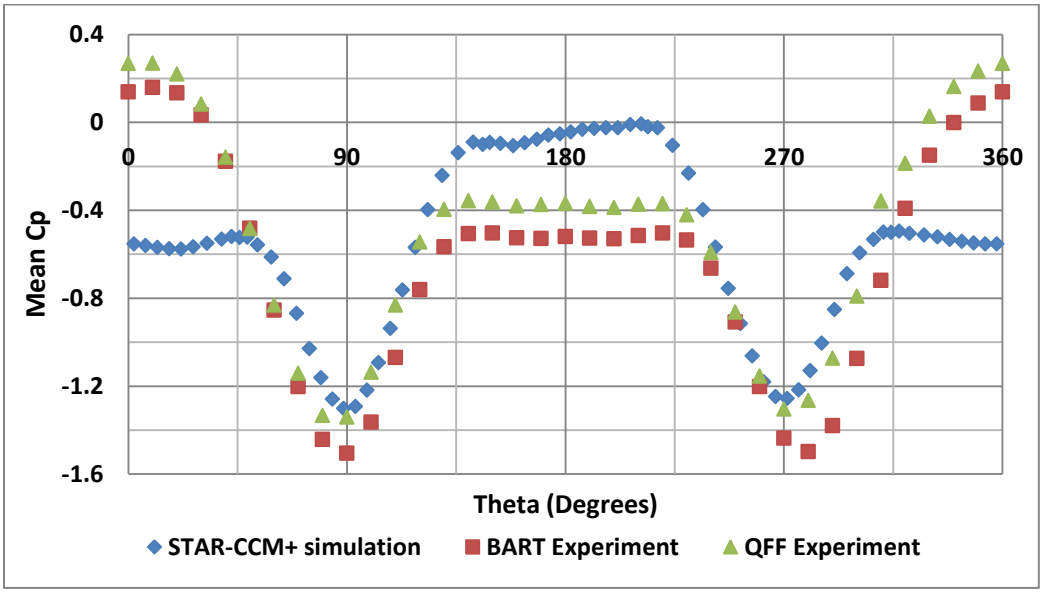

Figure 33: Mean pressure coefficient (C_p) of downstream cylinder

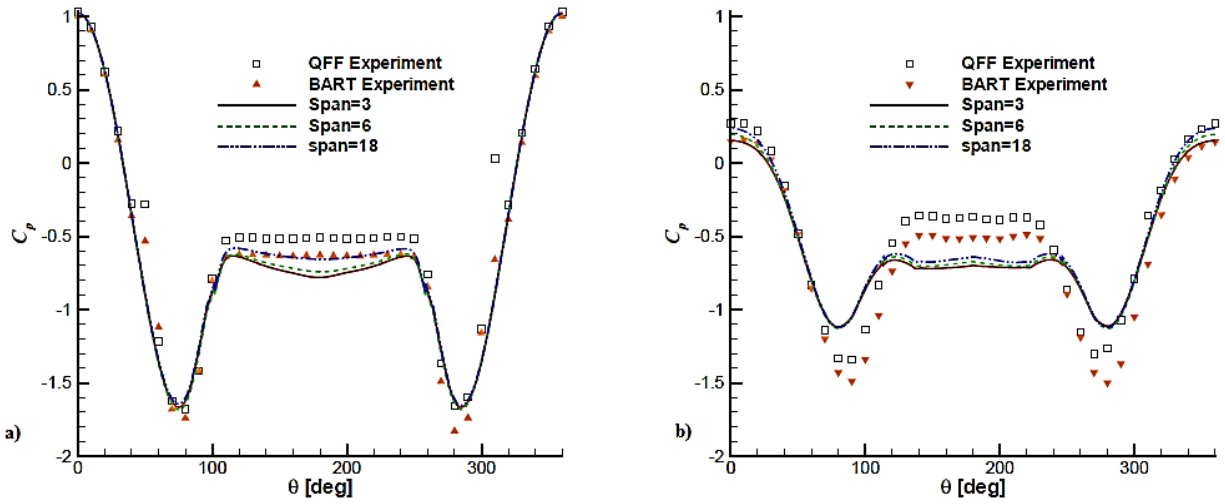

Figure 34: Mean pressure coefficient (C_p) from simulations by Lockard et al. [32] a) Upstream cylinder; b) Downstream cylinder

Figure 34 (a & b) shows the mean pressure coefficient results at the three different span distances from the simulations performed by Lockard et al. [32]. The results from Span = 3 are only used for this analysis. Using the BART results as a benchmark, it can be seen that at 80° and 280° on the upstream cylinder, the pressure coefficient is slightly under predicted in STAR-CCM+ simulation while it was over predicted in Lockard et al. [32]. Whereas, between about 100° and 250°, it is slightly over predicted in STAR-CCM+ simulation while it was under predicted in Lockard et al. [32]. At 80° and 280° on the downstream cylinder, the pressure coefficient is over predicted in STAR-CCM+ and Lockard et al. [32]. However, between about 100° and 250°, the results are over predicted in STAR-CCM+ but under predicted in Lockard et al. [32].

4.4 Acoustical Analysis of Results

Figure 35 shows the sketch of the location where the pressure spectra is measured on the upstream and downstream locations.

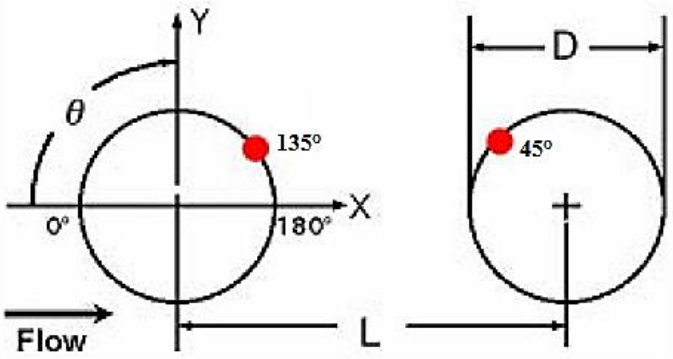

Figure 35: Locations where the pressure spectra is measured on upstream and downstream cylinders [32]

Figure 36 and Figure 37 show the pressure spectra at 135° and 45° on the upstream and downstream cylinder, respectively. They were analyzed using data from 0.05s to 0.15s time period of simulation. From both results, it can be seen that there is no distinct peak at the shedding frequency or the harmonics that follow. This is expected based on the aerodynamic analysis performed on the wake and mean pressure coefficient on the cylinders. A larger and more converged sample of data is needed for the analysis of the spectra.

It can also be seen that there is more fluctuation in the broadband of the signal. This is expected when using the detached eddy simulation model. However, the magnitude of the broadband is mostly lower than the experimental results in the upstream cylinder. It is higher than the experimental results in the downstream cylinder up to a 1000 Hz and then falls slightly lower than experiments afterwards.

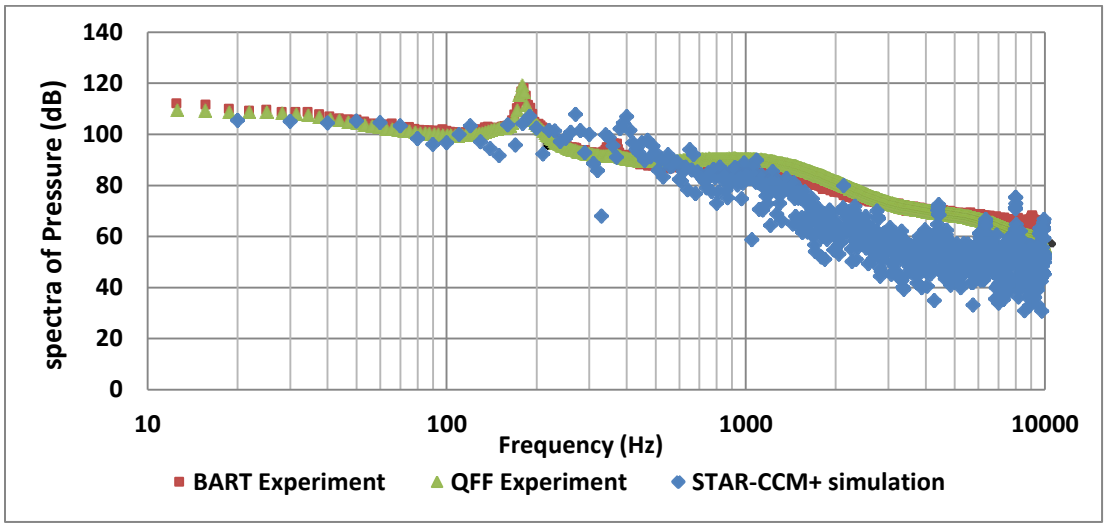

Figure 36: Spectra of pressure at 135 degrees on the upstream cylinder

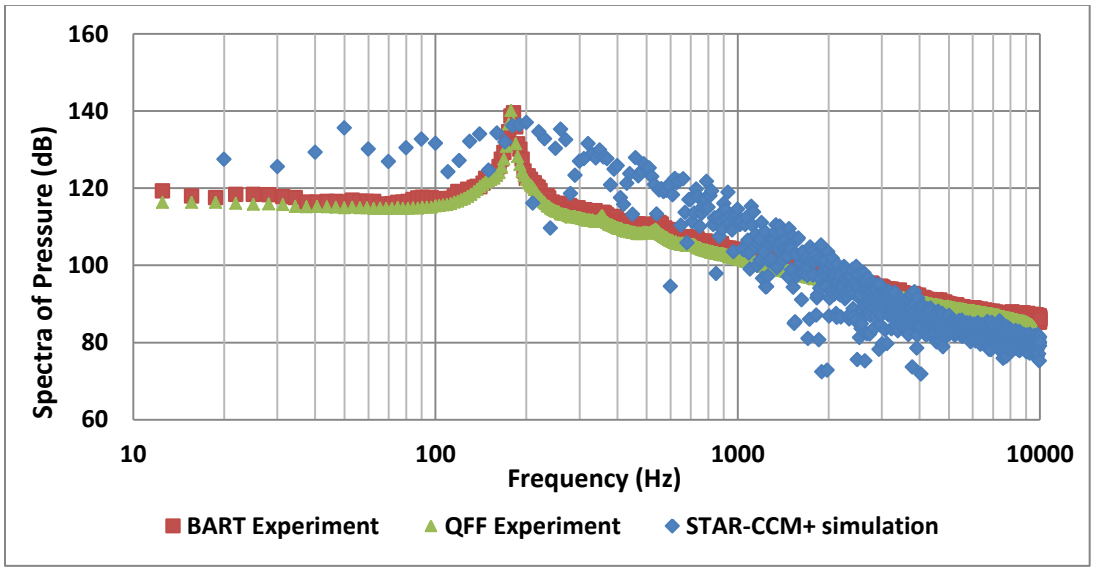

Figure 37: Spectra of pressure at 45 degrees on the downstream cylinder

Figure 38 to Figure 40 show the results of the sound pressure level (SPL) at the three microphone locations (A, B, and C). The exact location of the microphones is shown in Figure 19 and Table 1. A distinct peak is captured at the shedding frequency at each of the microphones. When compared to the QFF experimental results, the magnitude of the peak is about 10 dB lower. Due to the fluctuations in the broadband of the acoustic signal, it cannot be determined whether the harmonics of the simulation are distinct peaks as well. However, the magnitude of the broadband matches the QFF results relatively well. The QFF results have a frequency resolution of 3.125 Hz compared to about 10 Hz for the simulation. As a result, the discrepancies are likely due to the need for a larger and more converged sample.

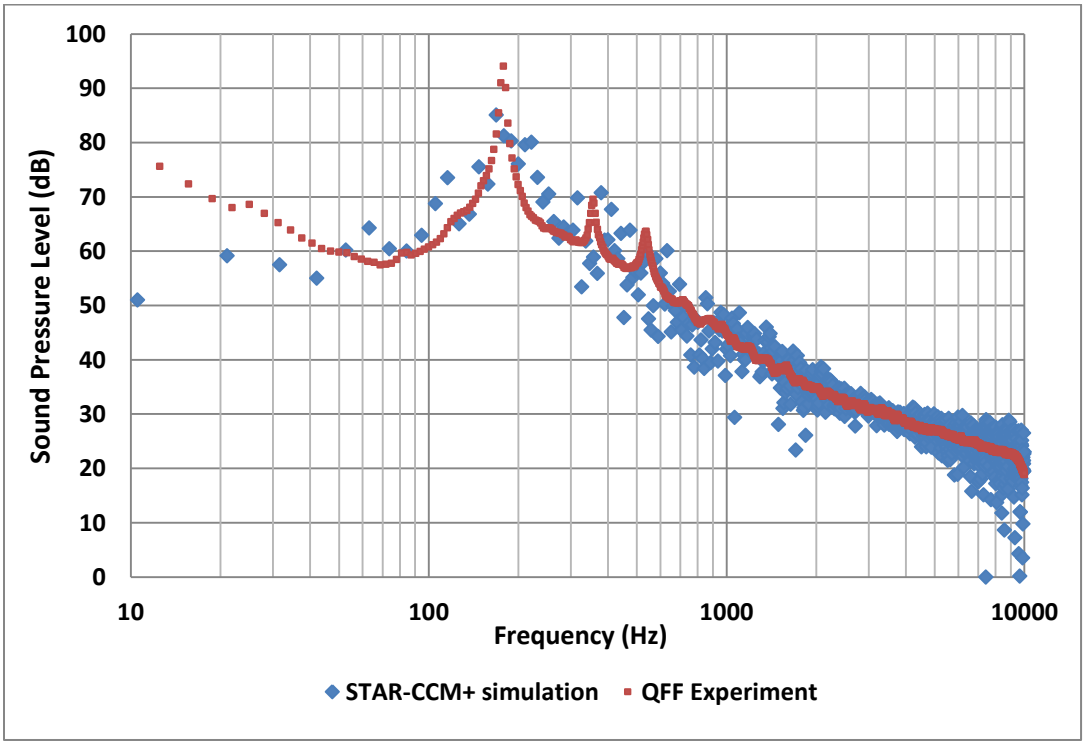

Figure 38: Sound Pressure Level (SPL) at Receiver A

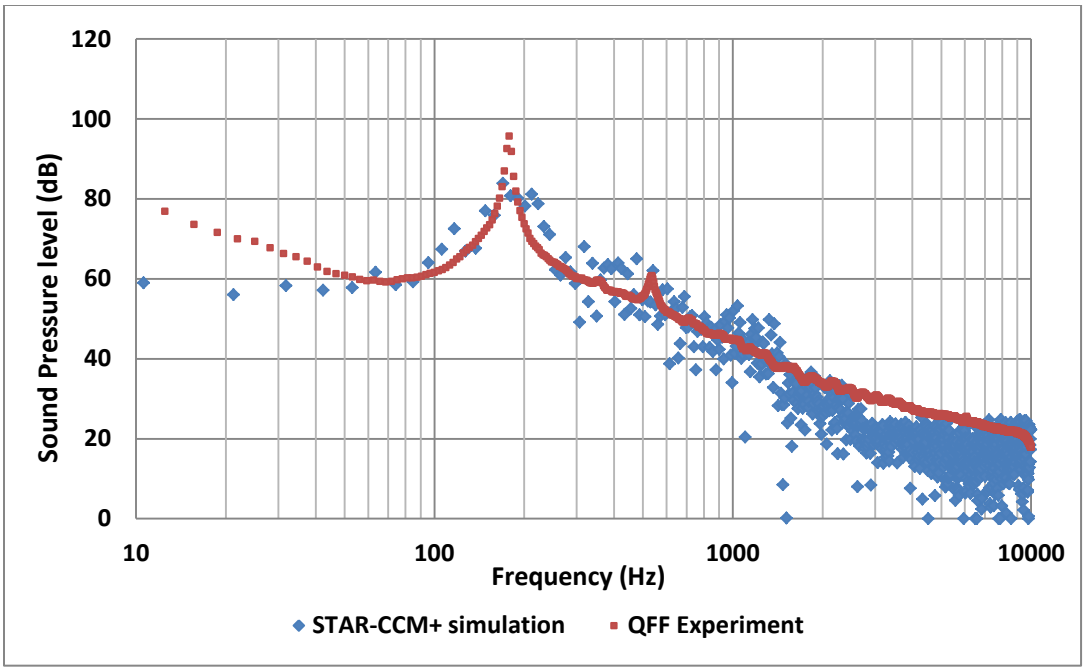

Figure 39: Sound Pressure Level (SPL) at Receiver B

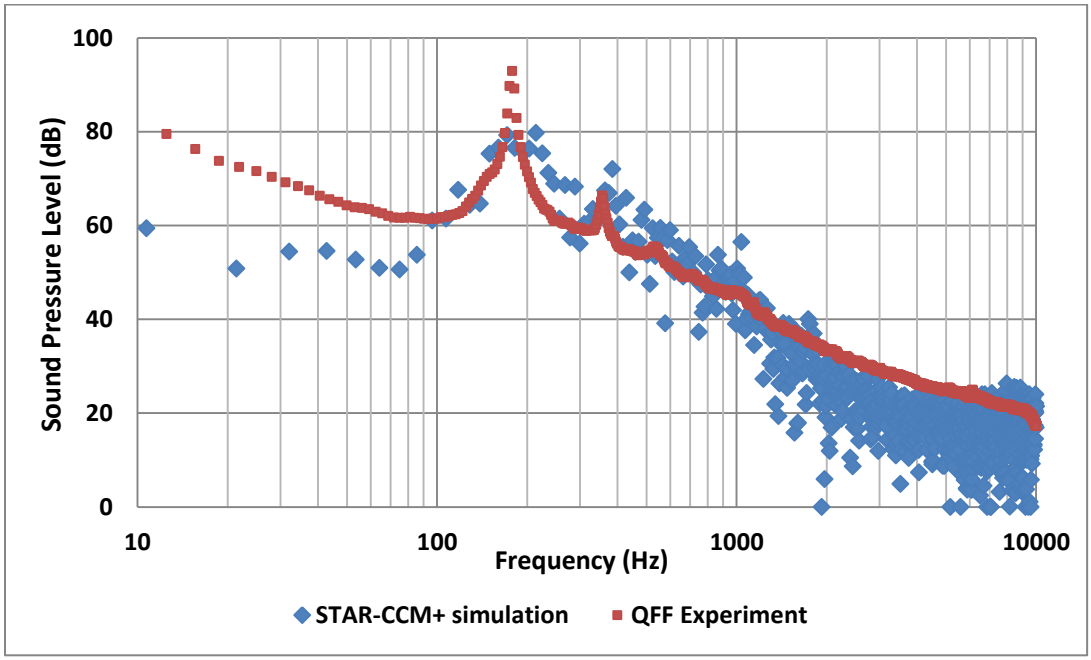

Figure 40: Sound Pressure Level (SPL) at Receiver C

Chapter 5

NASA SR-7A Propeller Case

NASA performs many experiments in wind tunnel settings in order to understand the flow phenomena around the propellers. One of those propellers that NASA investigated is the SR-7A. The 0.622 m diameter SR-7A model propeller was developed to enable the early determination of the aero-elastic characteristics of the full size 2.74 m diameter SR-7L propeller [42]. It is also used to perform tests to determine the aerodynamic and acoustic performance of the propeller at cruise conditions.

Figure 41 shows the shape of the SR-7A propeller blade. The airfoil sections used to design the SR-7A blade comprise of NACA 16 from the tip to the 57% radius of blade and NACA 65 with circular arc mean chamber lines from 41% radius to the root of blade. A transition section is located between 57% radius and 41% radius. These airfoils were used because of their high critical Mach number and wide, low drag buckets [42]. It has a tip sweep angle of 41 degrees measured from planform. The propeller has 8 blades with a designed tip speed of 244 m/s at cruise conditions (35,000 ft).

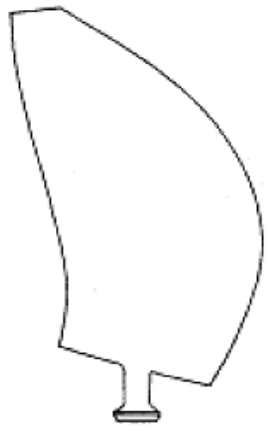

Figure 41: Shape of the SR-7A propeller blade [42]

5.1 Background Overview

Dittmar [12] conducted an experiment in the NASA Lewis Wind Tunnel to measure the noise levels of the SR-7A propeller. Five pressure transducers were installed, flush at the tunnel's ceiling. The view of the propeller in the test section and the location of the microphones are shown in Figure 42. The tests were conducting with the blade setting angle of 57.3 degrees with

the design advance ration of 3.06. The wind tunnel was operated at a Mach number ranging from 0.5 to 0.9 with 0.05 intervals.

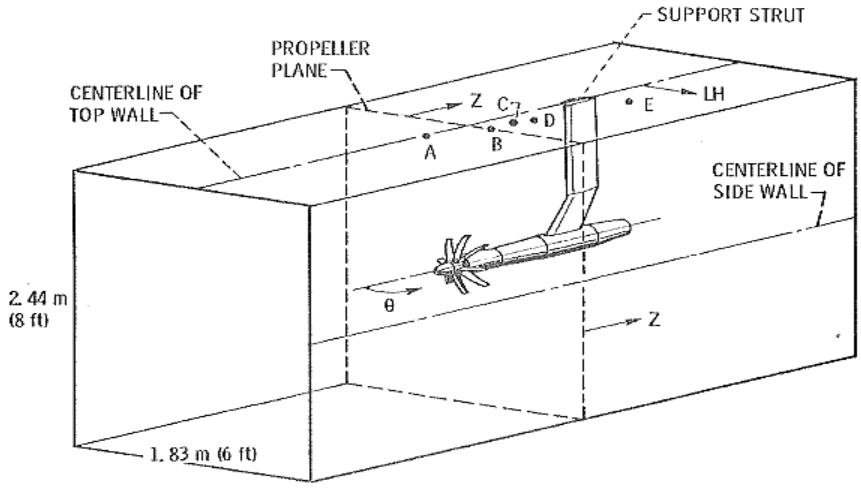

POSITION	TRANSDUCER (1 1/2 DIAMETER FROM TIP)				
	A	B	C	D	E
	TRANSDUCER POSITION, cm (in.)				
Z LH	-33.0(-13.0) 4.83(1.9)	0.953(0.375) 10.2(4.0)	23.9(9.4) 2.54(1.0)	45.2(17.8) 7.62(3.0)	107.4(42.3) 31.5(12.4)
NOMINAL ANGLE, θ, deg.	75	90	101	110	131

Figure 42: Pressure transducer locations with respect to SR-7A propeller in wind tunnel test section [14]

The signals from the transducers were recorded on magnetic tape. The narrowband range was from 0 to 10,000 Hz with a bandwidth of approximately 26 Hz. Higher resolution spectra was needed to isolate the propeller tonal signal at low Mach numbers because the blade passing frequency was close to the wind tunnel compressor tonal (0 to 1000 Hz with a 2.6 Hz bandwidth). The results were corrected to include the wind tunnel effects as well as difference in altitude.

Dittmar [14] observed that there is an increase in the sound pressure level (SPL) as helical tip Mach number (M_{ht}) increases. The increase reaches a peak at M_{ht} of 1.15 where the SPL starts decreasing after. He concluded that a possible reduction in SPLs could be attained by using faster rotating propellers. The results also indicated a strong directivity pattern, with a drop in SPL at Transducer C followed by a rise in SPL at Transducer D to the same level as Transducer B. This lobed pattern was consistent between Mach number 0.7 to 0.85 with 0.05 intervals. However, this pattern was not apparent at Mach numbers below 0.7 and higher than 0.85.

Stefko et al. [42] conducted aerodynamic performance tests at a range of Mach numbers (0.45 to 0.90) and advance ratios on the model SR-7A propeller. They computed the elemental thrust and power coefficients from a translating wake survey probe measurements and compared them with the thrust and torque on the propeller measured using a rotating balance. The results agreed reasonably well and indicated that the SR-7A propeller is performing well aerodynamically.

They also performed a flow visualization study on the SR-7A blades in order to determine if any leading edge vortices exist at two Mach numbers (0.6 and 0.8). The results showed a small leading edge vortex on both Mach numbers that would affect the blade loading distribution. Based on these results, they concluded that the full-scale SR-7L propeller will also perform well aerodynamically.

Due to the lack of detailed aerodynamic results on the SR-7A propeller blades, Heidelberg and Nallasamy [21] performed an experiment to measure the unsteady blade surface pressure at 9 different blade stations on the suction and pressure sides of the blade. The tests were also conducted in NASA Lewis 8 by 6 foot supersonic wind tunnel at a Mach number of 0.8. The advance ratio used is 3.06 and the inflow angle was set at 1.5°. The experiment was performed at cruise conditions with a blade setting angle of 60.1°.

Figure 43 shows the location of the pressure transducers on the suction surface of the blade. The transducers measuring the suction surface were installed on one blade and the ones measuring the pressure side were placed on the second blade. Both blades were mounted on the spinner at 180° apart.

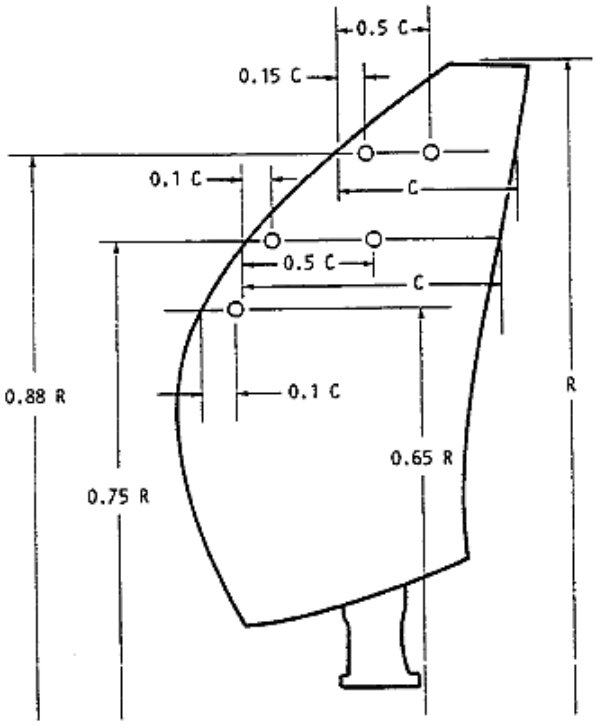

Figure 43: Pressure transducer locations on the SR-7A blade [21]

They compared the unsteady pressure coefficient at each of those locations with respect to the azimuth angle shown in Figure 44. These results were compared to an unsteady Euler code solution with the inflow angle set to 1.6°. The code predicted the shape of the waveforms accurately but over-predicted the magnitude in most cases.

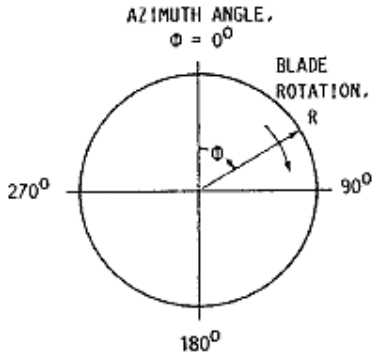

Figure 44: Reference of the azimuthal angles (view looking downstream) [21]

Woodward & Loffler [47] extended the experiments to the full-scale 2.4-m diameter, eight bladed SR-7L propeller in order to map the propeller source noise directivity patterns under actual flight conditions. The propeller was installed on the Gulfstream II aircraft wing and seven different test conditions were tested.

Flush-mounted microphones on the aircraft fuselage and an outboard microphone boom were installed as shown in Figure 45. In addition, the NASA Lewis Learjet was used as a tool to allow the measurement of acoustical radiation. The Learjet aircraft was flown close to the Gulfstream II aircraft and was equipped with flush-mounted wingtip and nose side microphones. Figure 46 shows the Gulfstream II aircraft and the Learjet aircraft in-flight. Additional microphones on the nose top and cabin roof were installed in order to measure propeller noise field below the Gulfstream II aircraft. The location of the acoustic instrumentation on the Learjet aircraft is shown in Figure 45.

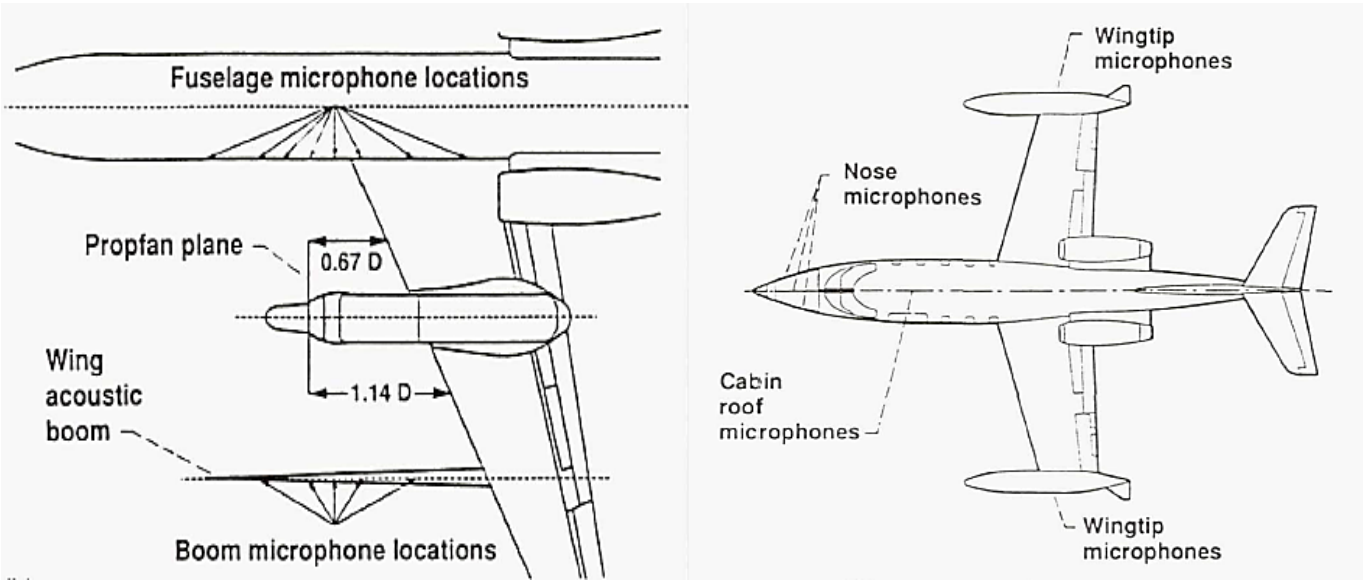

Figure 45: Acoustic Instrumentation on Gulfstream II (left) and Learjet (right) aircrafts [47]

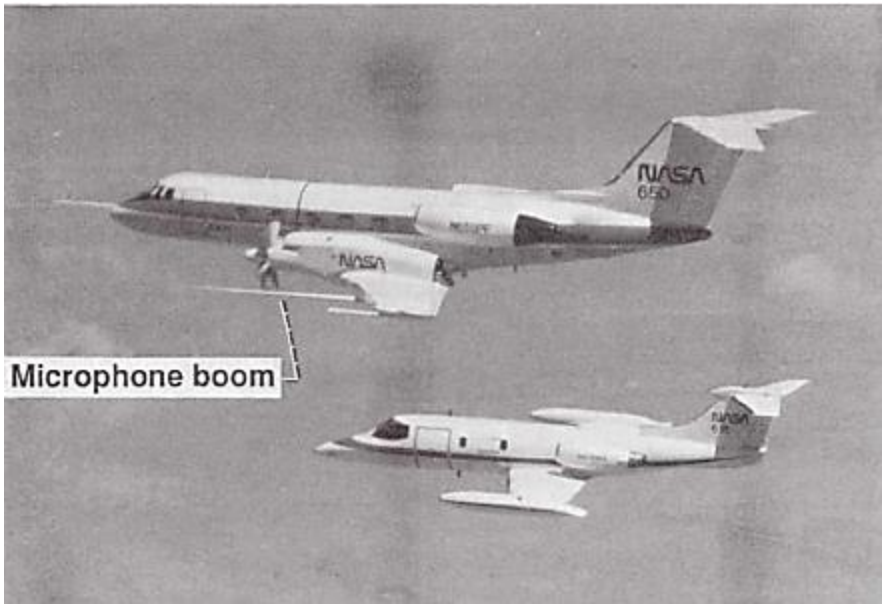

Figure 46: Inflight photograph of the Gulfstream II (top) and Learjet (bottom) aircrafts [47]

They concluded that the sideline directivities measured by the Learjet aircraft showed maximum noise levels at 105° from the upstream propeller axis. As for the azimuthal directivity, they concluded that the highest levels of noise occurred below the Gulfstream II aircraft. They also investigated the effect of the propeller tip speed and concluded that the reduction of tip speed resulted in a reduction in noise levels. However, this reduction was more significant along the horizontal plane than below the Gulfstream II aircraft.

De Gennaro et al. [6] presented the only available simulation results of a NASA propeller case using a commercial code, ANSYS FLUENT. Even though the researchers were using the NASA SR2 propeller, the simulation technique employed would be useful for the simulation of the SR-7A propeller. The aim of their simulation is to match the aerodynamic and acoustical results with NASA experiments.

They used periodic rotational boundary conditions to simulate only one blade of the propeller and employed the multiple reference frame (MRF) approach. The aerodynamic simulation was performed using Reynolds Averaging Navier-Stokes (RANS) model with the k-ω SST turbulence model for Mach numbers of 0.6 and 0.8. The acoustical calculations were performed using the Ffowcs Williams-Hawkings (FW-H) acoustic analogy to obtain the sound pressure levels at 12 pressure transducers as shown in Figure 47.

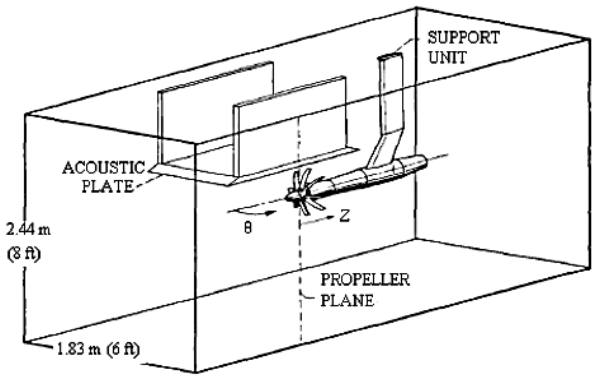

Microphone ID											
1	2	3	4	5	6	7	8	9	10	11	12
Transducer Distance from Propeller Plane, Z [cm]											
-46.7	-41.7	-30.5	-16.0	-8.9	0.8	8.9	12.4	18.0	25.0	28.7	42.4
Visual Angle θ, from upstream (0 in front) [deg]											
46.8	50.0	58.5	72.2	80	90.9	100	104	110	116.8	120	130.4

Figure 47: Microphone locations with respect to the SR2 propeller in test section [11]

The triangular surface mesh was employed on the blade, followed by a volume mesh consisting of 40 prism layers close to the blade surface and tetrahedral cells in the rest of the domain. A y+ value less than 1 was ensured. A total of 10.5 million cells were generated per periodic domain.

The power coefficient was the only parameter used for aerodynamic comparison with experiments. In order to match the results, De Gennaro et al. [6] changed the blade angle of the experiment by 1 degree. Out of the 12 microphone locations, only 5 locations were analyzed. In order to compare the simulation results with the experimental results, the simulation results were scaled to wind tunnel conditions. Table 7 lists the different corrections that are used and the corresponding sound pressure level correction. More details about each type of correction are explained in De Gennaro et al. [6].

Table 7: Sound pressure level (SPL) corrections added to CFD results

Correction Parameter	Ma = 0.6	Ma = 0.8
Plate device interference	8 dB	8 dB
Pressure loss in wind tunnel	-1 dB	-2.5 dB
Near-field/Far-field SPL scaling	26 dB	26 dB
Pseudo-noise	1 dB	1.5 dB
Wind tunnel effect	5.5 dB	2.5 dB
Non-linear effects	1 dB	3 dB
TOTAL	**40.5 dB**	**38.5 dB**

After applying these corrections, the sound pressure level of the blade passing frequency at the 5 chosen microphones matched relatively well with experimental data at both Mach numbers. The discrepancies of SPL (if any) were less than 2 dB difference.

5.2 Computational Aspects

The SR-7A blade is comprised of two airfoils: NACA 16 from the tip to the 57% radius of blade and NACA 65 with circular arc mean chamber lines from 41% radius to the root of blade. A transition section is located between 57% radius and 41% radius. It has a tip sweep angle of 41° measured from planform. The propeller diameter (D) is 0.622 meters. Figure 48 (a & b) shows the front and side view of the SR-7A propeller with spinner. The dimensions for the propeller and spinner are detailed in Stefko et al. [42] and Dittmar [11].

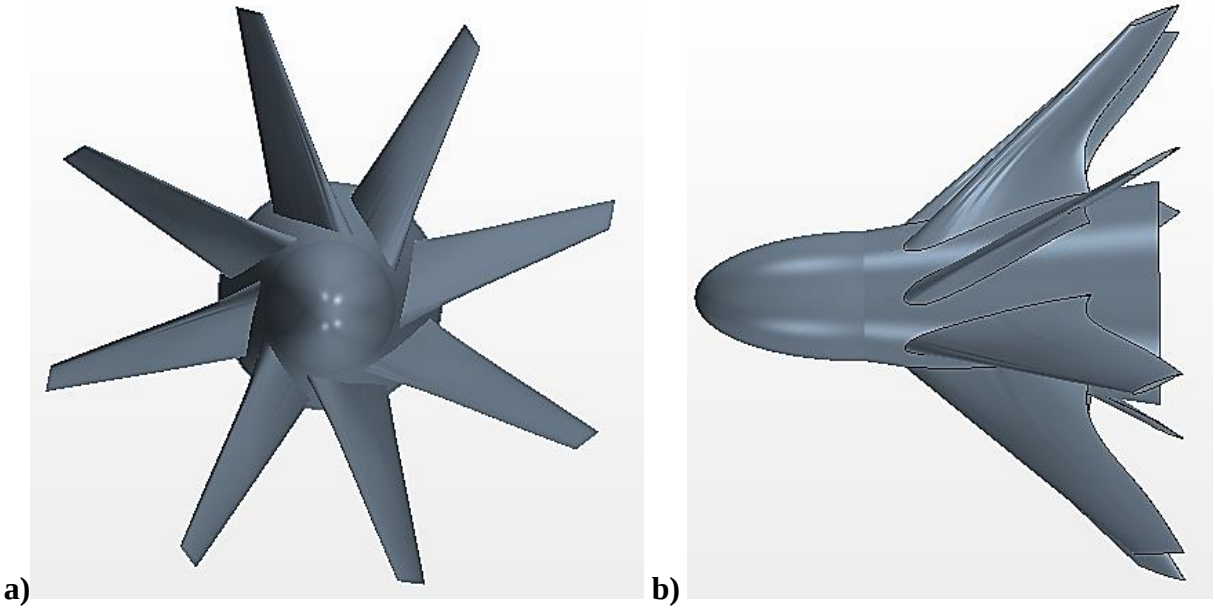

a) **b)**

Figure 48: SR-7A propeller with spinner a) Front view; b) Side view

A cylindrical shape is used to create the extents of the domain. The domain is divided into three regions: the outer domain, the rotating domain, and the permeable domain. The computational

domain of each region is shown in Figure 49. Figure 50 shows the vertical and horizontal view of the mesh distribution across the computational domain along with the location of each region. Table 8 lists the meshing parameters used to generate the mesh. This mesh is used in all simulations, unless otherwise stated.

The outer domain specifies the volume of air in which the propeller rotates. This volume should be large enough in order for the boundary conditions set to be satisfied at the boundaries. The permeable domain is created for acoustical purposes. In order to include the quadrupole sources (volume sources) in the prediction of the noise levels, a permeable surface needs to be created. This surface's diameter is set to be at 1.5D of the propeller and extends downstream of the propeller to include the tip vortices generation. Another advantage is that the mesh in this domain can be dense enough to avoid acoustic dissipation, while maintaining a relatively coarser mesh in the outer domains. This reduces the number of cells of the mesh and eventually reducing computational cost of the simulation. The rotating domain is used to specify the rotational speed of the propeller. It is set away from the propeller in order to ensure that there are no changes in the parameters across the interface.

One option was to make the permeable domain larger and set the rotational speed of the propeller in that domain, thereby avoiding the presence of the rotating domain. The permeable surface would rotate after every timestep, causing a re-mesh and change in the computation of fluxes at the interface. This effect of the sliding mesh would cause dissipation of the noise information that collects on the permeable surface from the volume it encompasses. As a result, this strategy is dismissed.

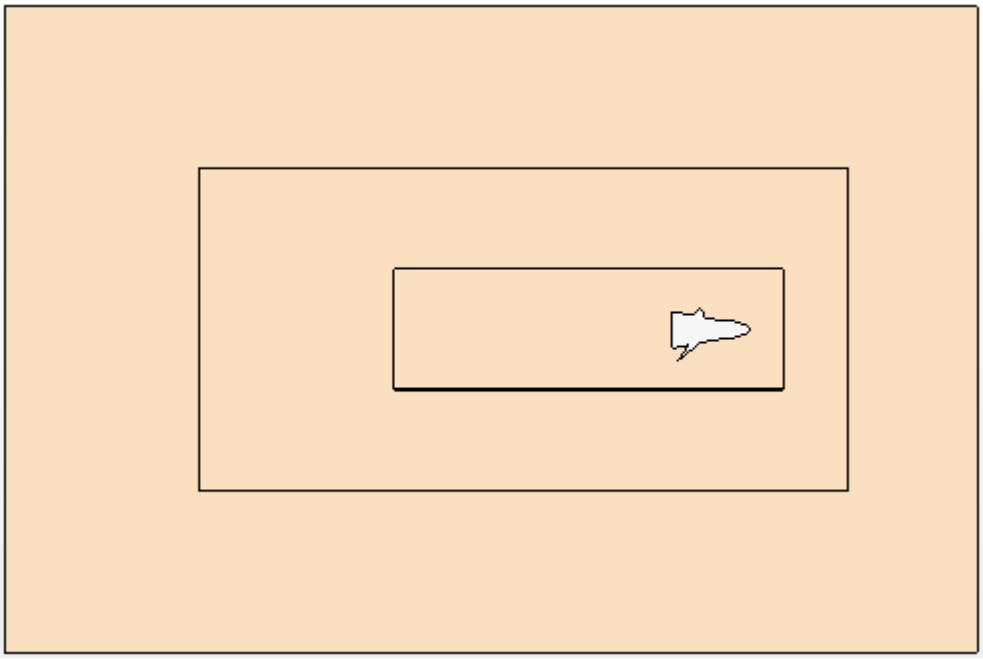

Figure 49: Computational domain of the SR-7A propeller

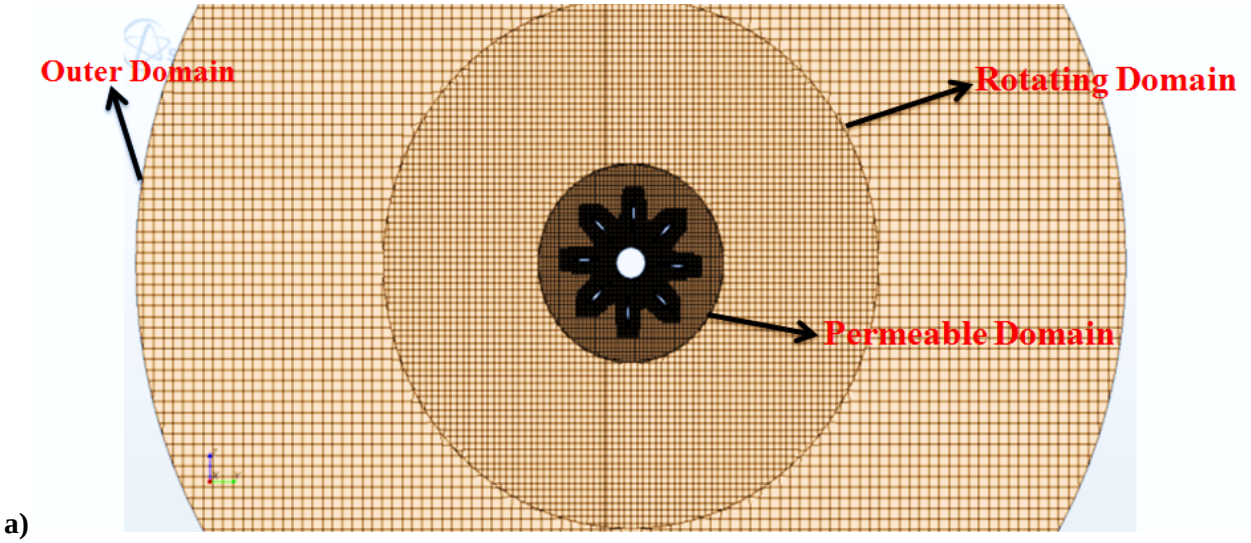

a)

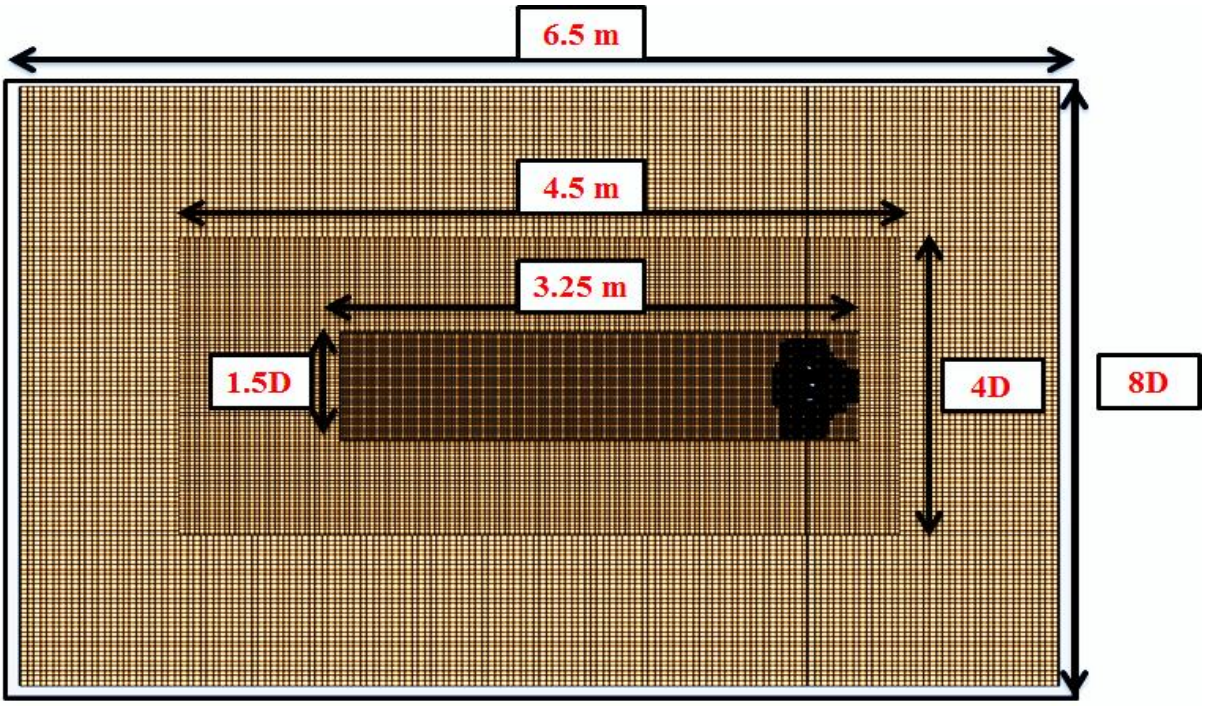

b)

Figure 50: a) Vertical mesh of the SR-7A propeller domain; b) Horizontal view of SR-7A propeller domain

Table 8: Meshing parameters for the NASA SR-7A propeller case

Parameters	Values
Number of Cells	3,977,977
Mesher Type	Trimmer & Prism Layer Mesher
Number of Prism Layers	10
Prism layer thickness	0.05 m
Thickness of near wall prism layer	0.005 m
Maximum Y+	254

5.3 Aerodynamic Analysis of Results

In order to achieve the ultimate goal of obtaining accurate noise levels at receivers' locations, the flow physics has to be captured accurately. This requires a thorough aerodynamic analysis. However, experimental results that would validate the simulation case are very scarce.

The most common experimental result available is the power coefficient. Despite its importance, it is an integral solution that could provide reasonable results for the wrong reasons (for example, through cancellation of forces, etc.). As a result, it does not provide enough details on the flow field around the propeller. Because acoustic results are highly dependent of the aerodynamics of the propeller, it is imperative that another parameter is analyzed. Heidelberg and Nallasamy (1990) presented experimental unsteady pressure coefficient results (the only other aerodynamic comparison present in literature) on the blade surface of the propeller. These experimental results will be used to give better understanding and confidence in the simulation results.

One of the most important parameters used in the aerospace/turbomachinery industry to define an operating condition is the advance ratio (J). It is a non-dimensional parameter that is defined as the ratio of the distance the propeller moves forward in one revolution and the diameter of the propeller, as shown in equation 41. n is the rotational speed in revolutions per second (rps), U_0 is the inlet velocity in m/s, and D is the diameter of the propeller in meters.

$$J = \frac{U_0}{nD} \qquad (41)$$

Different operating conditions will be simulated, as shown in Table 9. The operating conditions are performed at cruise conditions at 35,000-ft altitude. As a result, the speed of sound is 295.5 m/s and the freestream temperature is 217.0 K.

Table 9: Operating conditions for the SR-7A propeller

Operating Condition	Mach Number	Advance Ratio (J)	Rotational Speed (rpm)
1	0.6	3.06	5582
2	0.7	3.06	6520
3	0.8	3.06	7455

In this thesis, the power coefficient and the unsteady pressure coefficient on the blade surface will be analyzed and compared to the NASA experimental results.

5.3.1 Power Coefficient (C_{power})

The power coefficient is the first parameter that is used to analyze the aerodynamic flow field. It is defined in equation 42, where P is the power produced by the propeller and ρ_0 is the free-stream density at cruise conditions.

$$C_{power} = \frac{P}{\rho_0 n^3 D^5} \quad (42)$$

Power coefficient is presented in the literature as a function of the blade setting angle (β) and the advance ratio (J). The blade setting angle is the angle between the chord of the blade (usually measured at the 0.75R) and the rotational plane. For this thesis, the advance ratio is set to 3.06 and the blade setting angle is set to 60.2°. Table 10 shows the physics parameters that were used to obtain the power coefficient at the operating conditions.

Table 10: Physics parameters for the power coefficient simulation

Parameter	Value
Model	k-ω SST
Rotation Model	MRF then Sliding Mesh
Wall Treatment	All y+ treatment
Flow Regime	Turbulent
Equation of State	Ideal Gas

Table 11 shows the results of power coefficient at the different operating conditions. It can be seen that the power coefficient obtained from the simulations matched the experimental results closely at all Mach numbers.

Table 11: Power coefficient (C_{power}) at different Mach numbers

Operating Condition	Mach Number	Experimental C_{power}	Simulation C_{power}	Tip Speed (m/s)
1	0.6	1.88	1.91	182.3
2	0.7	1.75	1.78	212.1
3	0.8	1.55	1.57	243.5

Another important parameter related to power coefficient is the tip speed. The speed at the tip of the propeller blades matches the design tip speed. This is important because the noise generation due to tip vortices is an essential component of the quadrupole noise source. As a result, predicting the right helical tip Mach number is very critical.

5.3.2 Unsteady Pressure Coefficient ($C_{pressure}$)

Unsteady pressure coefficient ($C_{pressure}$) is the second parameter used to evaluate the aerodynamic flow field around the propeller. Heidelberg and Nallasamy [21] performed an experiment to measure the unsteady blade surface pressure at different blade stations on the suction and pressure sides of the blade. The location of the pressure transducers on the blade are shown in Figure 43. This simulation is intended to mimic this NASA experiment and provide unsteady pressure coefficient at the same locations for comparison purposes.

To obtain these results, the same computational setup, shown in Figure 49, is used. The inflow angle is changed from 0° to 1.6° with a 0.8 Mach number. Figure 51 shows how the inflow angle is implemented in the experiment. However, instead of tilting the propeller to achieve this change, the propeller is kept the same and the inflow angle is implemented on the flow field itself. Both these procedures are identical since the angle is relative to the position of propeller.

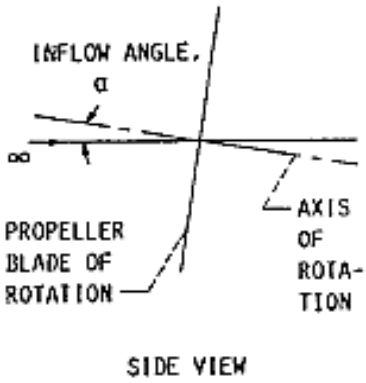

Figure 51: Inflow angle implementation in experiments [21]

Due to the high computational cost of the simulation, the pressure and suction surfaces of one location (0.65R at 0.1c) will be evaluated. Table 12 and Table 13 list the physics parameters and resulting stoppage criteria that were used in the simulation. A steady solution was run before it was switched to an unsteady solution of 5 complete propeller revolutions with a 0.5° interval per timestep to improve convergence. The computational cost for the SR-7A simulation is shown in Table 14.

Table 12: Physics parameters for unsteady pressure coefficient simulation

Parameter	Value
Model	-
Rotation Model	MRF then Sliding Mesh
Wall Treatment	-
Flow Regime	Inviscid
Equation of State	Ideal Gas

Table 13: Stoppage criteria for unsteady pressure coefficient simulation

Parameter	Value
Timestep size	1.120071685 E-5 s
Temporal Discretization	2nd order
Iterations per timestep	20
Total physical time	0.04032258 s
Number of timesteps	3,600

Table 14: Computational cost of the unsteady pressure coefficient simulation

Parameter	Value
Total run time	0.04032258 s
Total wall clock time	40.16 hrs
Number of CPU	64
Wall clock time per timestep	33.46 s

Figure 52 shows the streamlines on the suction surface on the propeller blade at 0.65R at 0.1c. *R* refers to the radius of propeller blade and c refers to the length of the chord from the leading edge.

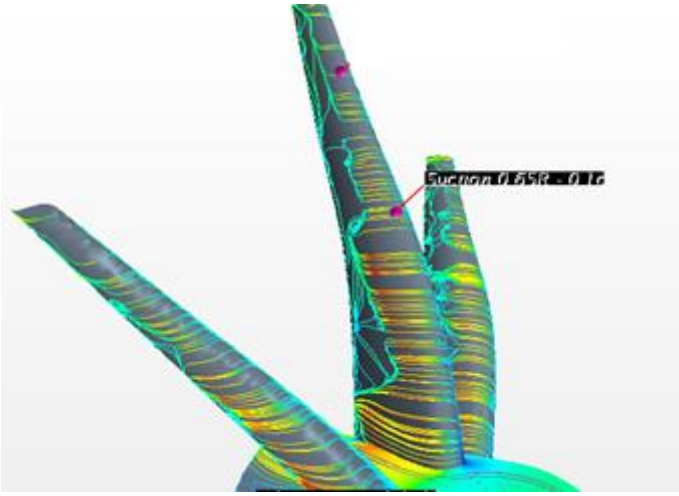

Figure 52: Streamlines on the suction surface of the propeller blade

As shown in Figure 52, there is a lot of separation along the suction surface of the propeller blade. This is an unexpected behavior given the chosen inviscid flow model. No separation should take place because there is no viscosity in the flow. This indicates that some other phenomenon is taking place and further investigation is required. The unsteady pressure

coefficient is analyzed to see if this behavior affects the results. It is plotted with respect to the azimuth angle (shown in Figure 44) and the results are compared to the unsteady Euler code solution presented in Heidelberg & Nallasamy [21]. The unsteady pressure coefficient is calculated using equation 43.

$$C_p = \frac{\text{Unsteady Pressure}}{(\text{Local Dynamic Pressure})_i} \qquad (43)$$

Where, $\text{Local Dynamic Pressure} = \frac{1}{2}(\gamma)(\text{Static Pressure})(\text{Local Mach Number})^2$

$i = $ local azimuthal angle, and

$\gamma = $ ratio of specific heat

Figure 53 shows the streamlines close to the transducer location at 0.65R – 0.1c on the suction side. A lot of separation is shown towards the trailing edge of the propeller. As discussed earlier, this phenomenon is not expected because of the model used for this simulation. There appears to be artificial viscosity that forms due to the 2nd order truncation error. This would affect the unsteady pressure coefficient results shown in Figure 54. Compared to the NASA Euler code results, it can be seen that the STAR-CCM+ results experience a lot of fluctuation. The trend is somewhat captured but the magnitude is way off. The magnitude error is likely due to the type of normalization used in the unsteady pressure coefficient. Both the 4th and 5th revolution results are plotted on the same plot to see if the solution has converged. It can be seen that more time is needed for the solution to reach to that stage.

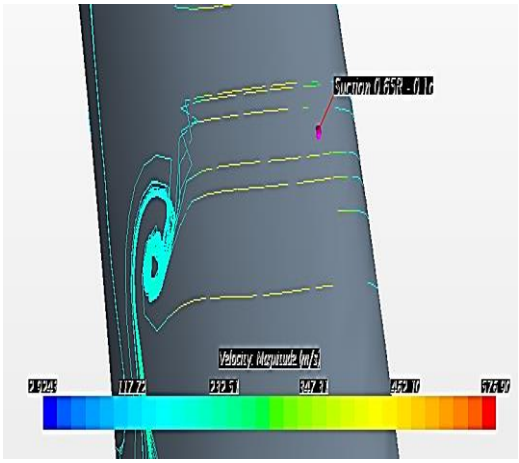

Figure 53: Streamlines close to the transducer location at 0.65R-0.1c on suction surface

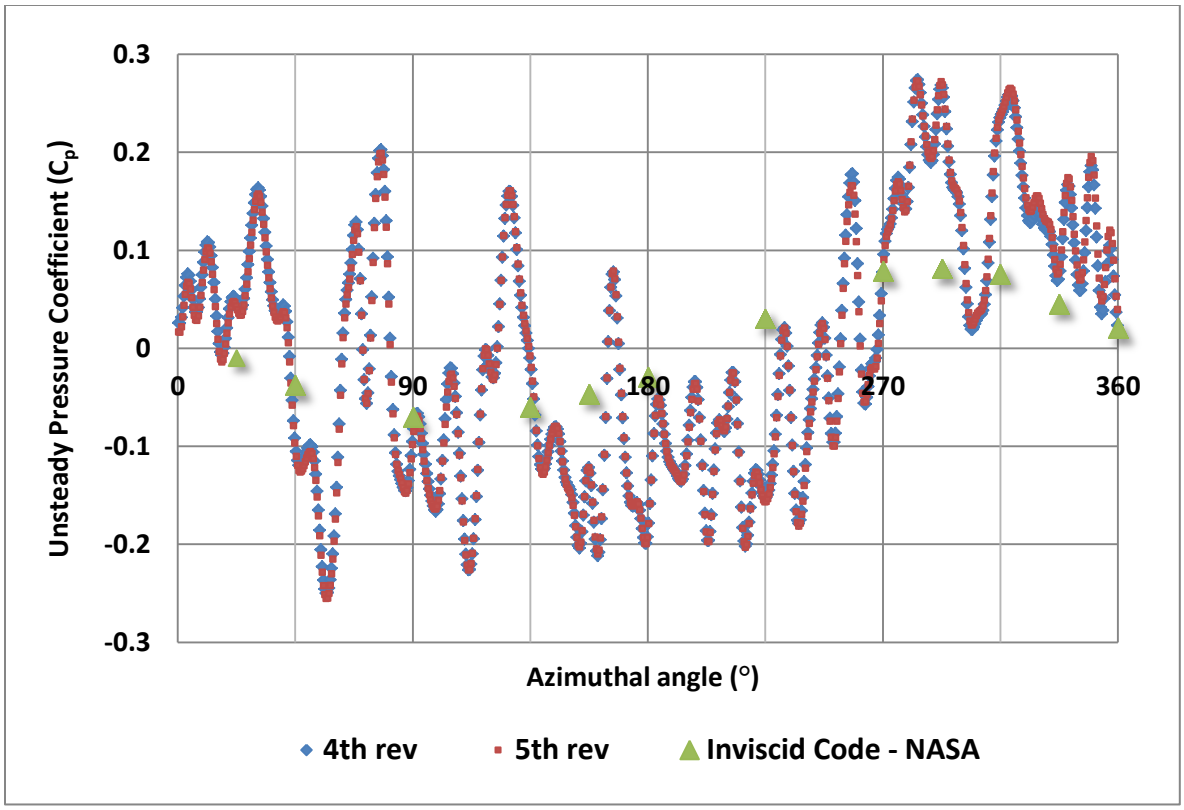

Figure 54: Unsteady pressure coefficient at the azimuthal angle on suction surface at 0.65R – 0.1c

Figure 55 shows the zoomed view of the streamlines close to the 0.65R – 0.1c transducer location on the pressure surface of the blade. The streamlines are smooth with no separation at all. This is expected because of the inviscid code used in the simulations. The plot for the unsteady pressure coefficient is compared to the NASA Euler code results as shown in Figure 56. It can be seen that the trend and magnitude of unsteady pressure coefficient is somewhat captured. However, the fluctuations in the results remain.

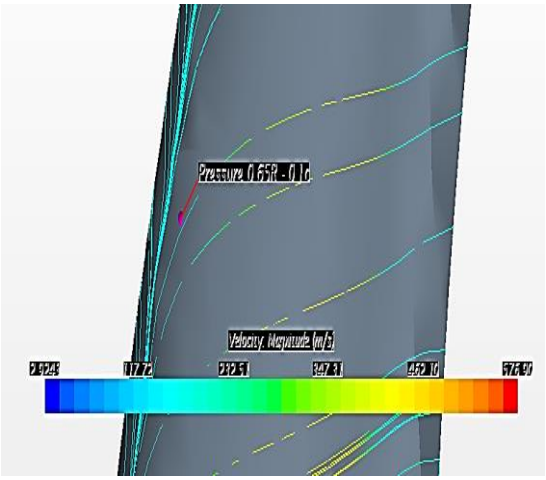

Figure 55: Streamlines close to the transducer locations on pressure surface of 0.65R-0.1c

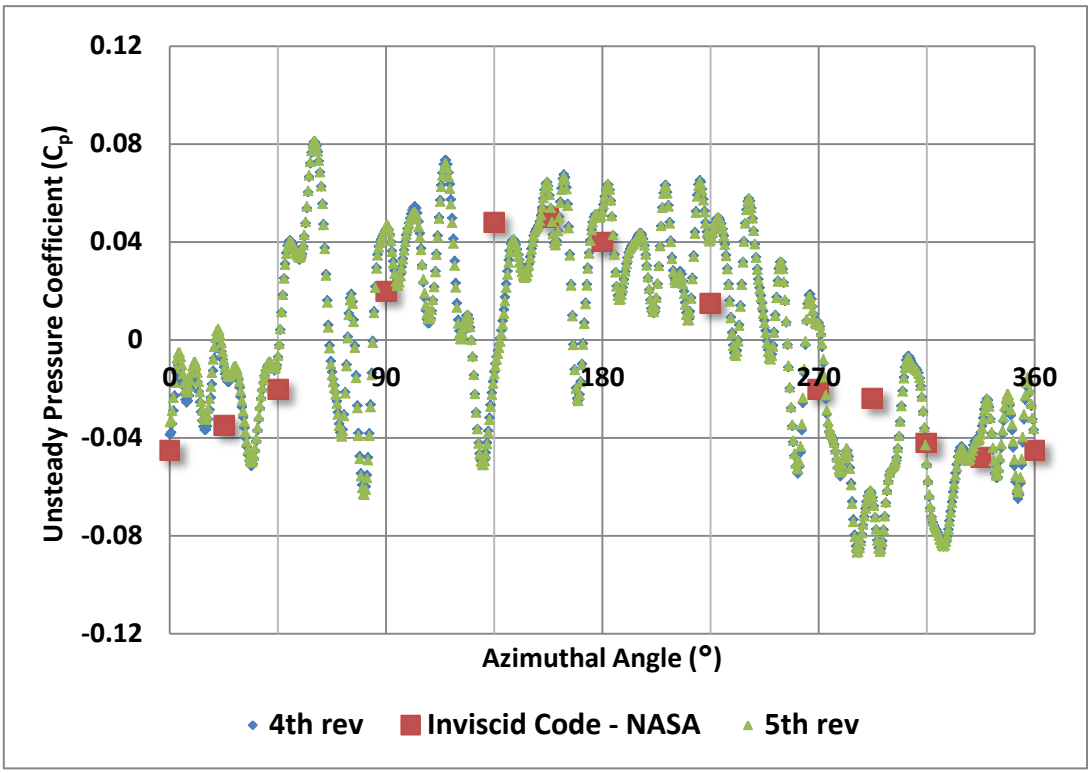

Figure 56: Unsteady pressure coefficient at the azimuthal angle on pressure surface at 0.65R – 0.1c

The fluctuations observed in the unsteady pressure coefficient plots on the transducer on the suction and pressure surface is likely due to the density of the mesh close to the blade. When using a sliding mesh approach, the propeller and the associated mesh is moving at a specified rotational speed. A poor mesh close to the blade would lead to quick and sudden changes in the pressure as the angle of attack of the fluid changes relative to the blade rotation.

In order to test our hypothesis that the meshing is causing the fluctuations in the unsteady pressure coefficient, a new simulation was performed using a finer mesh close to the blades. The normalization used to find the unsteady pressure coefficient was also changed. Table 15 shows the new meshing parameters used. Table 16 and Table 17 show the stoppage criteria and the computational cost for the new three-revolution simulation.

Table 15: Meshing parameters for the modified unsteady pressure coefficient simulation

Parameters	Values
Number of Cells	5,104,324
Mesher Type	Trimmer & Prism Layer Mesher
Number of Prism Layers	12
Prism layer thickness	1E-4 m
Thickness of near wall prism layer	1E-7 m

Table 16: Stoppage criteria for modified unsteady pressure coefficient simulation

Parameter	Value
Timestep size	1.120071685 E-5 s
Temporal Discretization	2nd order
Iterations per timestep	20
Total physical time	0.02419355 s
Number of timesteps	2160

Table 17: Computational cost of the modified unsteady pressure coefficient simulation

Parameters	Value
Total run time	0.02419355 s
Total wall clock time	61.27 hrs
Number of CPU	96
Wall clock time per timestep	102.12 s

The unsteady pressure coefficient is calculated in the same way as shown in equation 43 with one exception: the local dynamic pressure is calculated differently, as shown in the equation 44. This is essential because STAR-CCM+ did not calculate the previous definition in the correct, intended manner.

$$\text{Local Dynamic Pressure} = \text{Local Total Pressure} - \text{Local Static Pressure} \quad (44)$$

Figure 57 and Figure 58 show the streamlines on the suction and pressure surface of the propeller using the finer mesh, respectively. There is still some separation available on the suction side of the blade, but it has reduced greatly when compared to Figure 52. However, the streamlines are smooth on the pressure side of the blade.

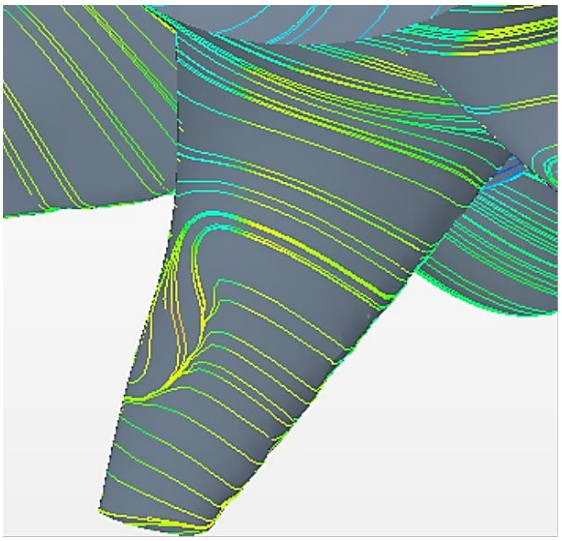

Figure 57: Streamlines on the suction surface of the propeller blade

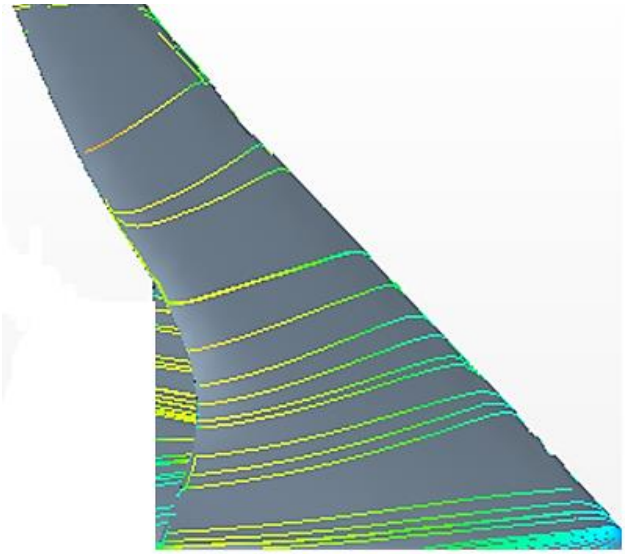

Figure 58: Streamlines on the pressure surface of the propeller blade

The unsteady pressure coefficient results for the suction and pressure surface are shown in Figure 59 and Figure 60, respectively. It can be seen that there is barely any fluctuations along the azimuthal angle as compared to previous plots. Both the trend and magnitude are well captured using the normalization definition of local dynamic pressure. However, the waveform does not follow the NASA code at a couple locations. The unsteady pressure coefficient is higher that the code from 22.5° to about 90° in both the suction and pressure surface. Around 135°, the waveform becomes steeper until it reaches 180° before it follows the same slope as the NASA code results.

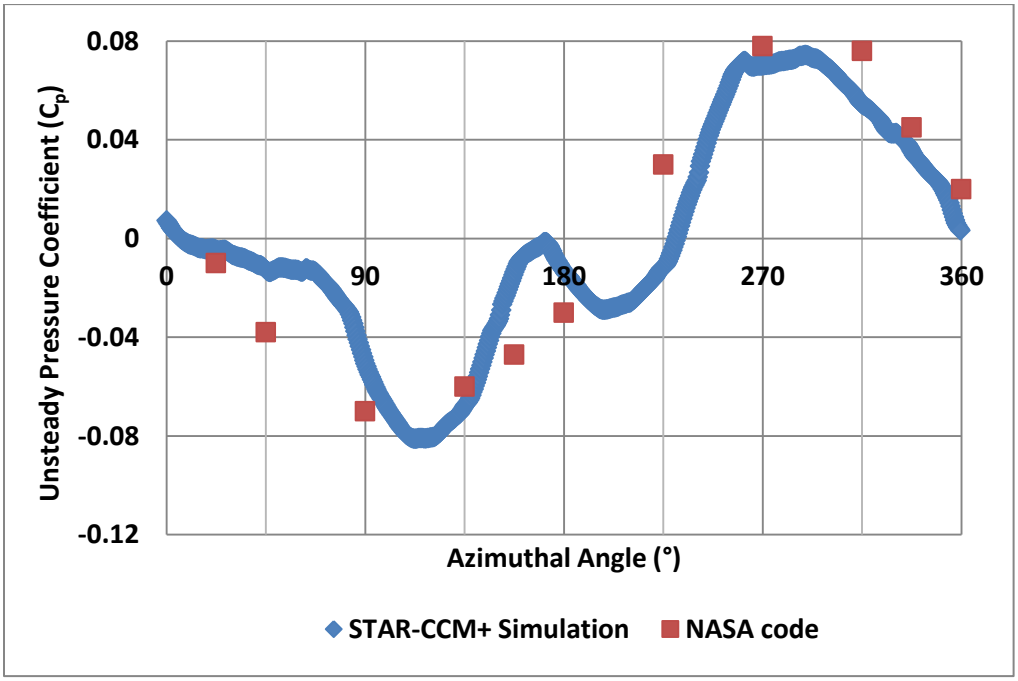

Figure 59: Unsteady pressure coefficient at the azimuthal angle on suction surface

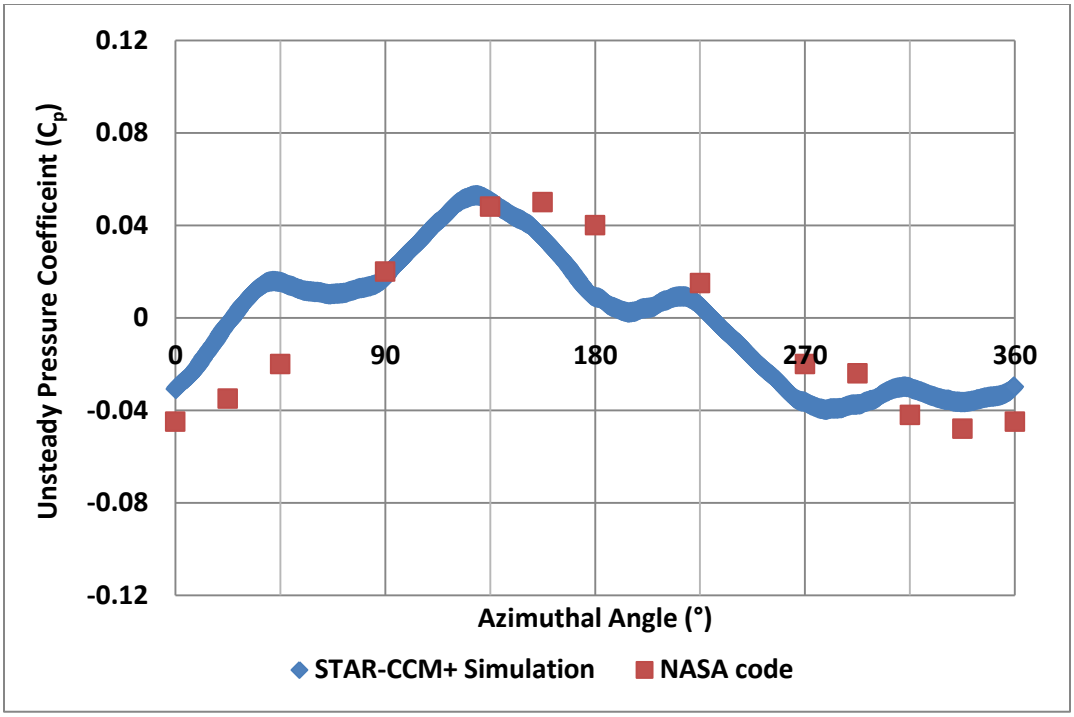

Figure 60: Unsteady pressure coefficient at the azimuthal angle on pressure surface

After obtaining the results of the unsteady pressure coefficient using two mesh densities around the propeller blades, it is apparent that extreme care should be exercised in choosing the mesh sizing and density. The cell size of the mesh is even more important in order to resolve the contribution of the noise sources accurately. Equation 45 represents the formula used to determine the cell size needed inside the permeable region. Since FW-H equation is used to propagate the noise levels from the permeable surface to the receivers, the mesh sizing outside the permeable region is not too critical.

$$Cell\ size\ in\ permeable\ region = \frac{c}{(F * M)} \quad (45)$$

c is the speed of sound (m/s), F is the frequency needed to be resolved (Hz), M is the number of recommended cells per acoustical wavelength. In this simulation, the mesh sizing is resolved up to 3000 Hz (about 3 blade passing frequency) with a STAR-CCM+ recommendation of 20 cells per acoustical wavelength [5]. As a result, it would be ideal if the cell sizing in the permeable region is 0.004925 m.

5.4 Acoustical Analysis of Results

The aerodynamic results confirmed that the physics involved in the rotation of the SR-7A propeller have been captured. At this point, an acoustical simulation for Mach number of 0.6 and 0.7 can be obtained using the same computational setup as in Figure 49 with the permeable surface used for acoustic propagation. The experimental results from Dittmar [12] are used as a basis of comparison. The same receiver locations shown in Figure 42 are used in this simulation.

However, due to the presence of the receivers in the near-field and the utilization of FW-H equations to propagate the sound waves, the receiver locations were moved upward from 2D (near-field) to 16D (in freestream) from propeller center. Table 18 shows the coordinate locations of the five receivers at 16D from propeller centerline. As a result, two corrections are used to account for the differences between cruise and wind tunnel conditions.

Table 18: Coordinates for the five receiver location for acoustic simulation

Receiver	X (m)	Y (m)	Z (m)
A	-0.33	0.0643	10.223
B	0.00953	0.118	10.223
C	0.239	0.0414	10.223
D	0.452	0.0922	10.223
E	1.074	0.331	10.223

Two major corrections are made to account for differences in altitude and distance to transducers. The altitude corrections involve adjusting the wind tunnel conditions to cruise conditions. The wind tunnel operating pressure is 76,500 Pa while the simulation pressure at cruise conditions is 23,800 Pa. Equation 46 is used to calculate the change in sound pressure level (SPL) that is needed. This change is then added to the raw wind tunnel results presented in Dittmar [12].

$$\Delta SPL\ (dB) = SPL_{Cruise} - SPL_{WindTunnel} = 20 \log\left(\frac{P_{Cruise}}{P_{WindTunnel}}\right) \quad (46)$$

The second correction is to account for the differences in the location of the transducers. The transducers are located at 16D from propeller centerline in the simulations because the acoustic model (FW-H) is originally developed for farfield. However, the transducers are located on the ceiling of the wind tunnel wall at 1.5D from propeller tip. As a result, the simulation results need to be adjusted to the wind tunnel transducer locations. Equation 47 is used to calculate the change in the sound pressure level (SPL) and then added to the simulation results.

$$\Delta SPL\ (dB) = SPL_{2D} - SPL_{16D} = 20 \log\left(\frac{16D}{2D}\right) \quad (47)$$

Table 19 lists the different SPL corrections that will be used to adjust the experimental and simulations results, accordingly. In the SR-2 simulation of De Gennaro et al. [6], they used various corrections (shown in Table 7) based on literature to adjust the computed sound pressure level. It was observed that some of these corrections were based on estimates and were not used to correct the results in this thesis.

Table 19: Sound pressure level (SPL) corrections

Correction Parameter	Application	Ma = 0.6	Ma = 0.8
Pressure loss (dB)	Subtract from wind tunnel results	10	10
Near-field/Far-field SPL scaling (dB)	Add to simulation results	20	20

Table 20 lists the physics parameters that were used in the acoustic simulation. A steady solution was run before it was switched to an unsteady solution of 13 complete propeller revolutions with a 4° interval per timestep. The resulting stoppage criteria for the simulation is shown in Table 21.

Table 20: Physics parameters for the acoustic simulation

Parameter	Value
Model	k-ω SST
Rotation Model	MRF then Sliding Mesh
Wall Treatment	All y+ treatment
Flow Regime	Turbulent
Equation of State	Ideal Gas

Table 21: Stoppage criteria for the acoustic simulation

Parameter	Value
Timestep size	9.0 E-5 s
Temporal Discretization	2nd order
Iterations per timestep	30
Total physical time	0.108 s
Number of timesteps	1,200

Table 22: Computational cost of the acoustic simulation

Parameters	Value
Total run time	0.108 s
Total wall clock time	61.27 hrs
Number of CPU	96
Wall clock time per timestep	102.12 s

Figure 61 – Figure 65 show the corrected experimental and simulation results at the 0.7 Mach number for the five receivers. It can be seen that the blade passing frequencies and their associated harmonics were well captured for all receivers. The sound pressure levels were well captured for the most part at Receivers A to D, with a maximum deviation of 5 dB below NASA results at Receiver D. For the third harmonic, the simulation results deviated by about 5 dB

below the corrected NASA wind tunnel experiments at all receivers. The sound pressure levels at Receiver E were about 15 dB below the NASA results for the blade passing frequency. The gap continued to increase at the second and third harmonics.

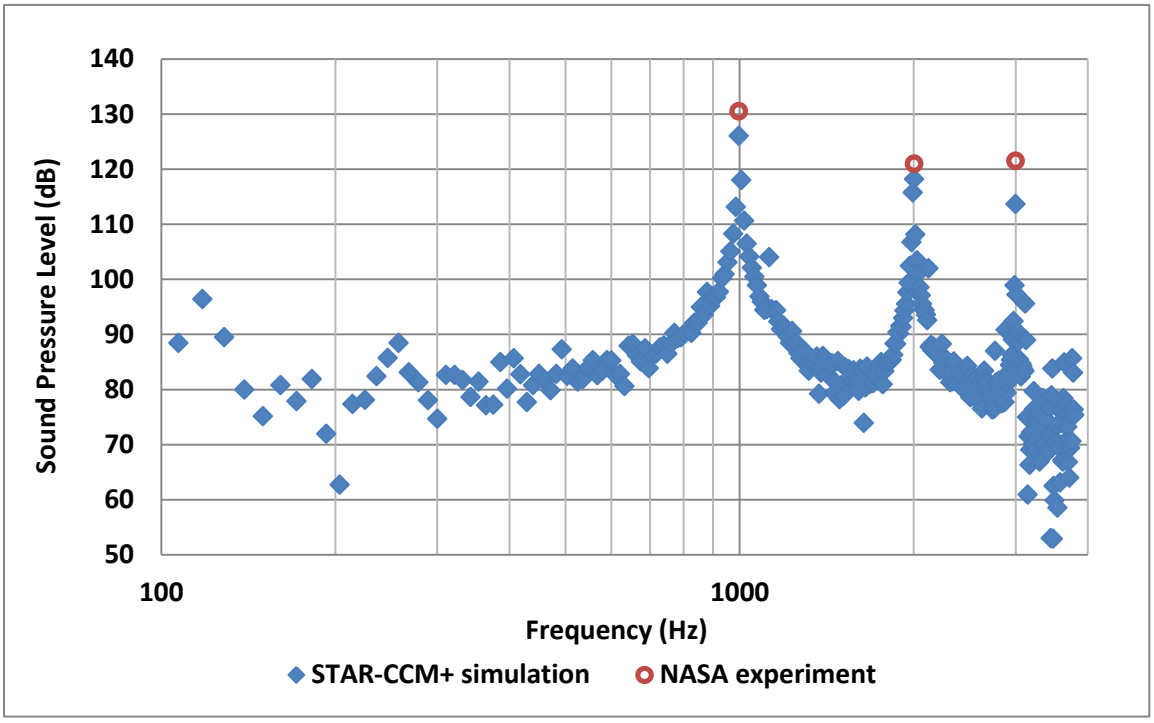

Figure 61: Sound Pressure Level (SPL) at Receiver A for 0.7 Mach number

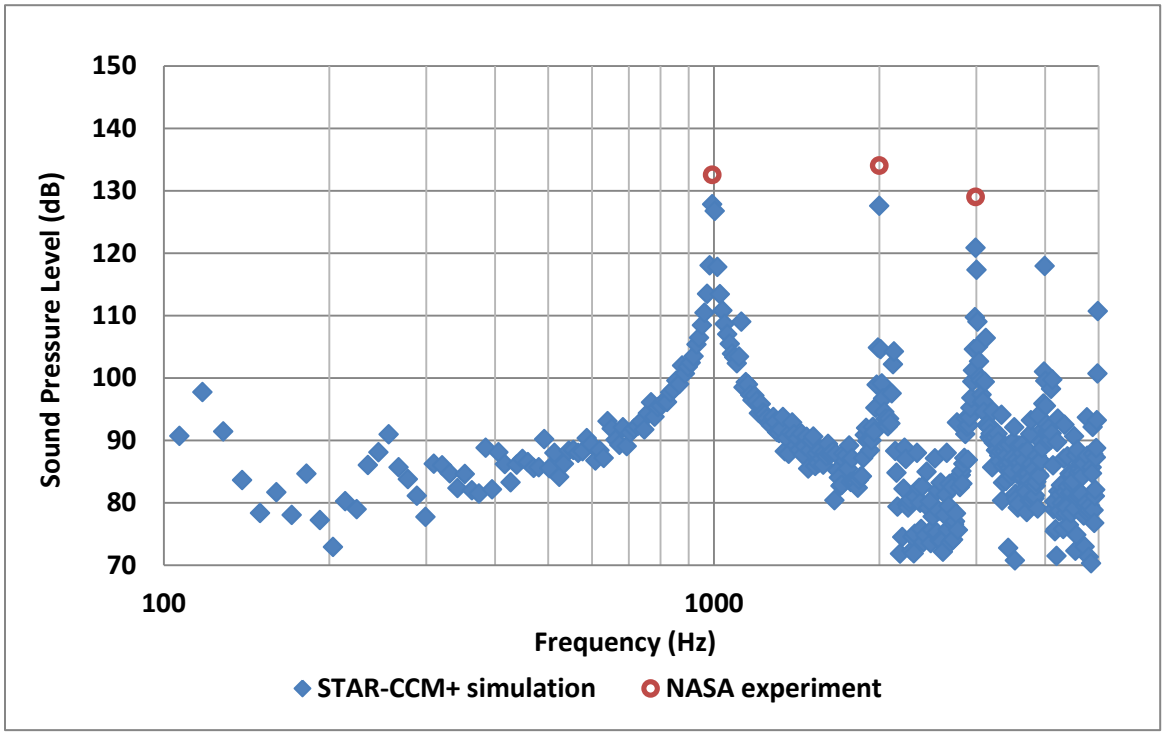

Figure 62: Sound Pressure Level (SPL) at Receiver B for 0.7 Mach number

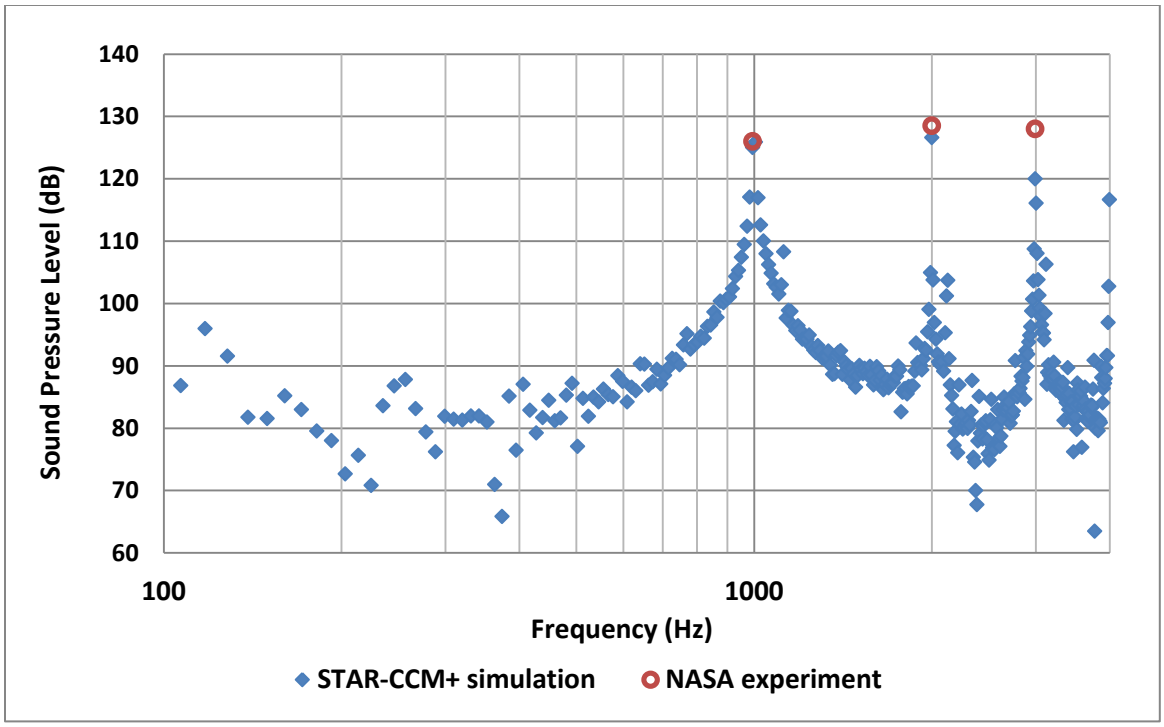

Figure 63: Sound Pressure Level (SPL) at Receiver C for 0.7 Mach number

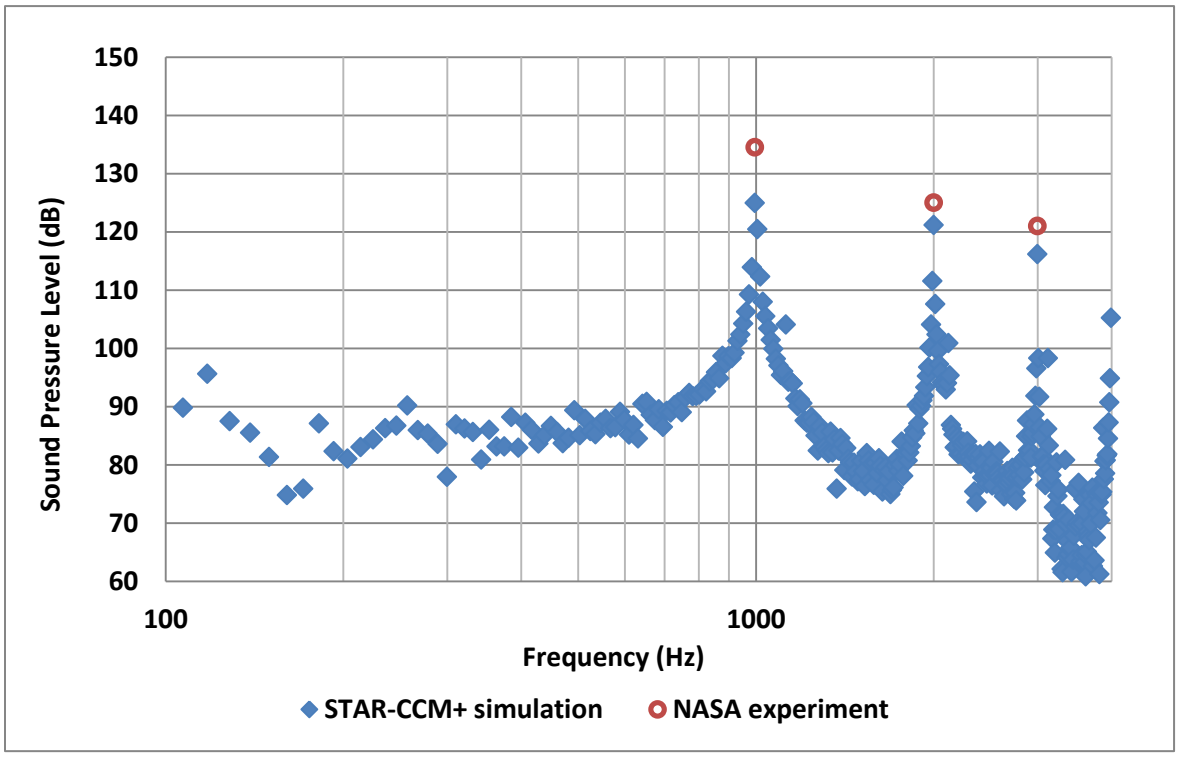

Figure 64: Sound Pressure Level (SPL) at Receiver D for 0.7 Mach number

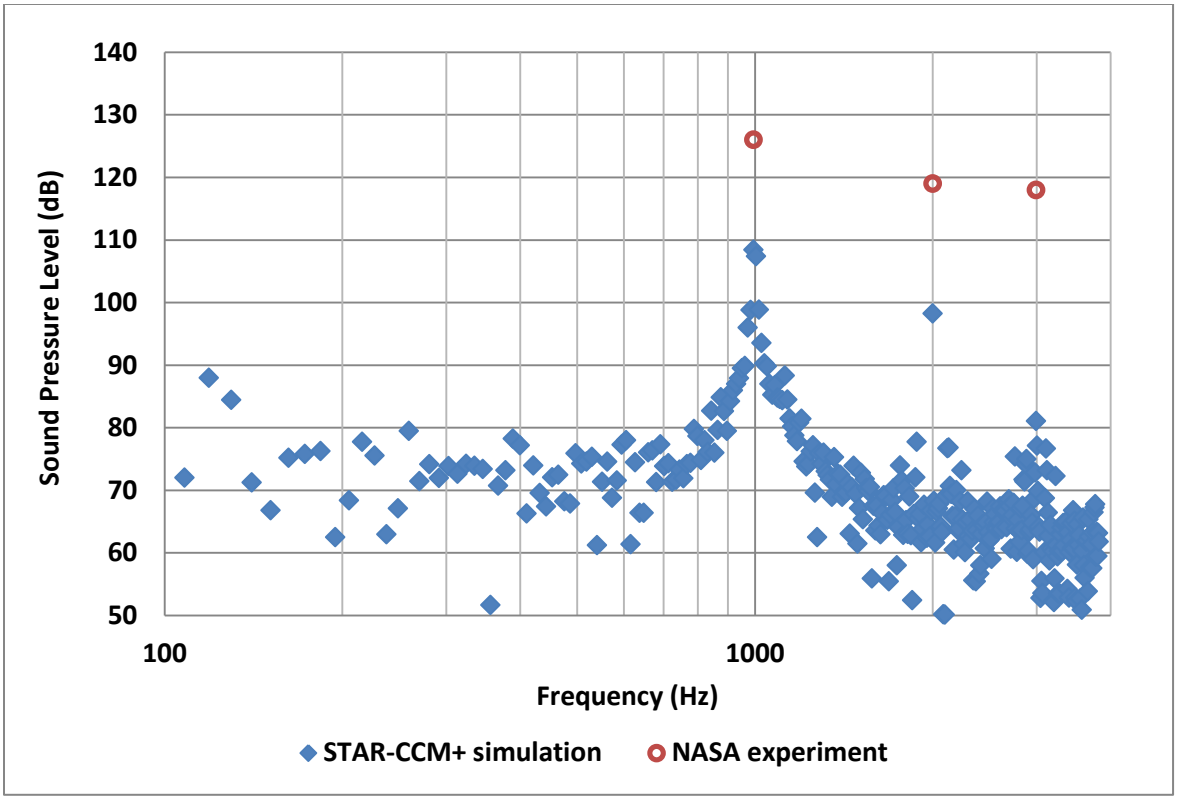

Figure 65: Sound Pressure Level (SPL) at Receiver E for 0.7 Mach number

Figure 66 – Figure 70 show the corrected experimental and simulation results at the 0.6 Mach number for the five receivers. Similar to the 0.7 Mach number results, the blade passing frequencies and their associated harmonics were well captured for all receivers. The sound pressure levels deviated by an average of 5 dB at Receivers A to D. The sound pressure levels at Receiver E were about 15 dB below the NASA results for the blade passing frequency. This is consistent with the results in Figure 65.

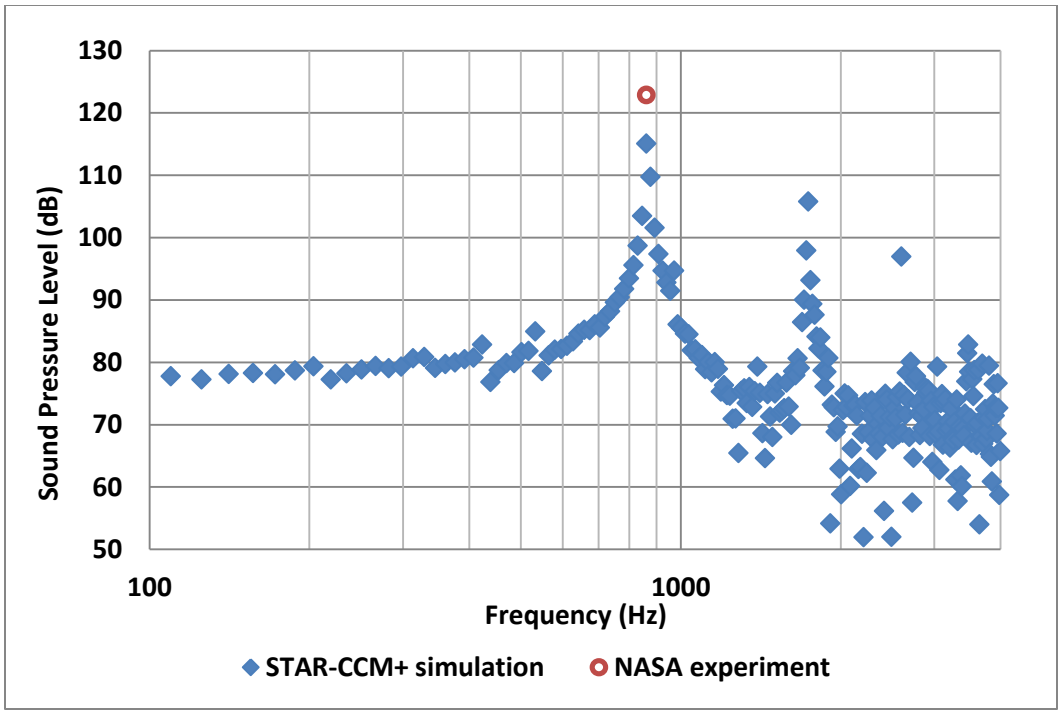

Figure 66: Sound Pressure Level (SPL) at Receiver A for 0.6 Mach number

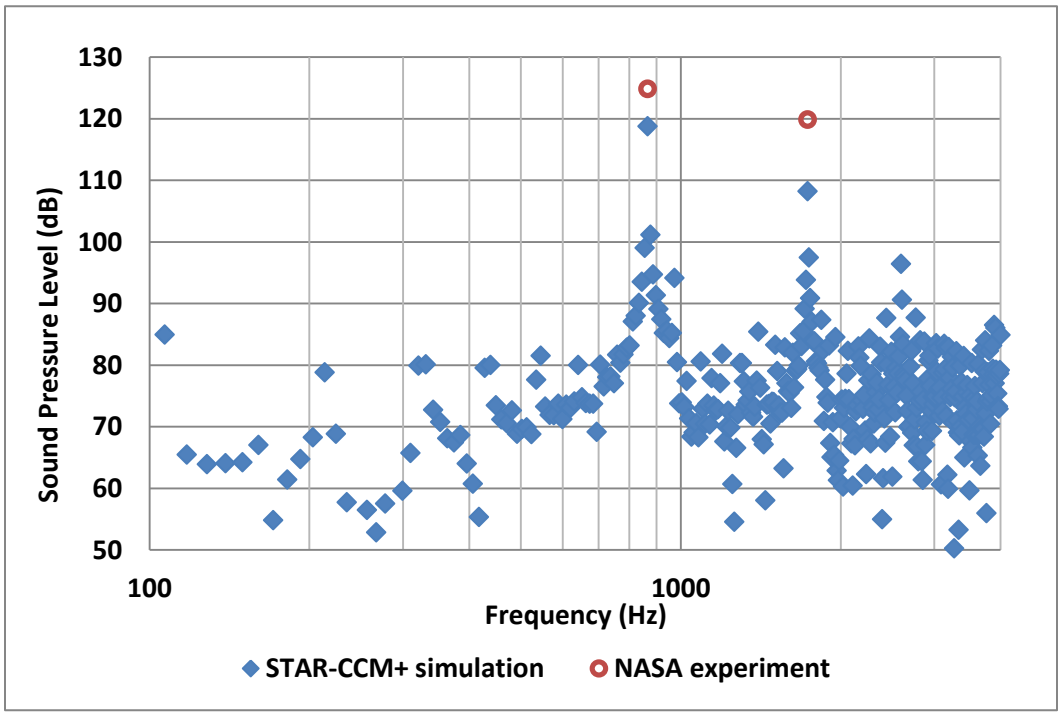

Figure 67: Sound Pressure Level (SPL) at Receiver B for 0.6 Mach number

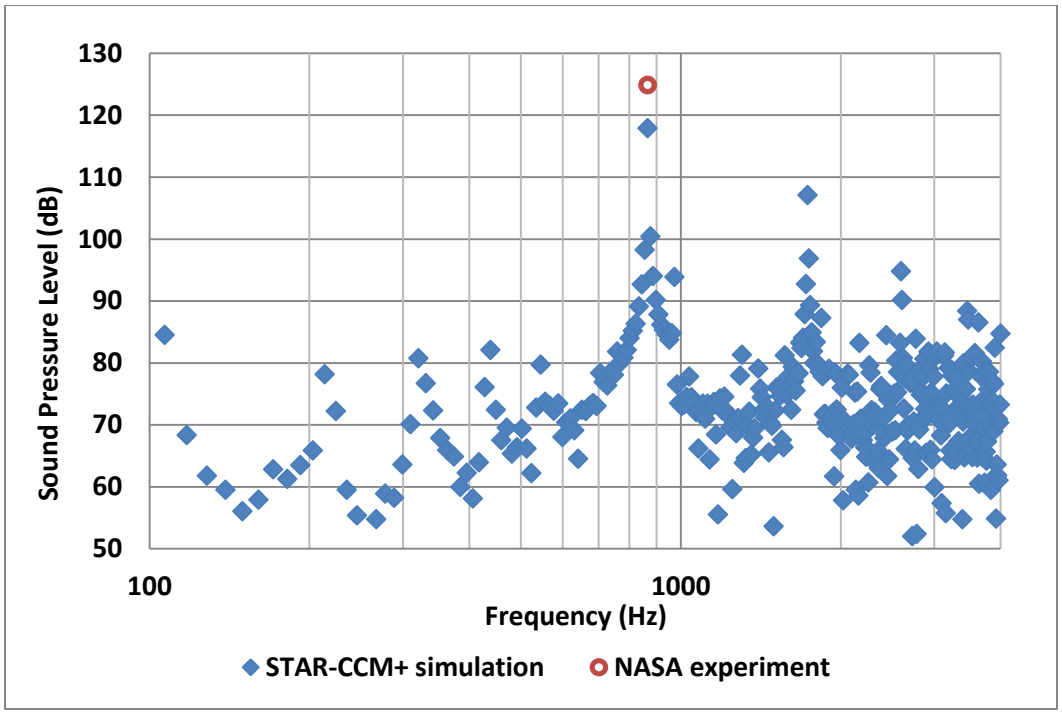

Figure 68: Sound Pressure Level (SPL) at Receiver C for 0.6 Mach number

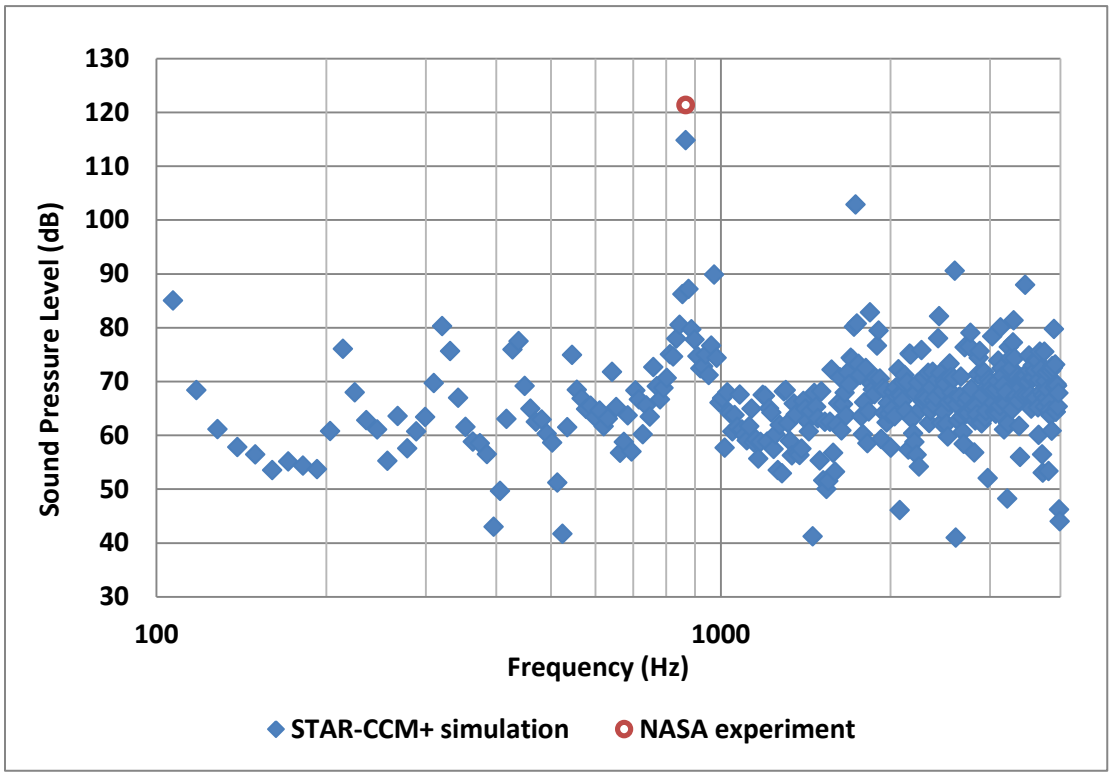

Figure 69: Sound Pressure Level (SPL) at Receiver D for 0.6 Mach number

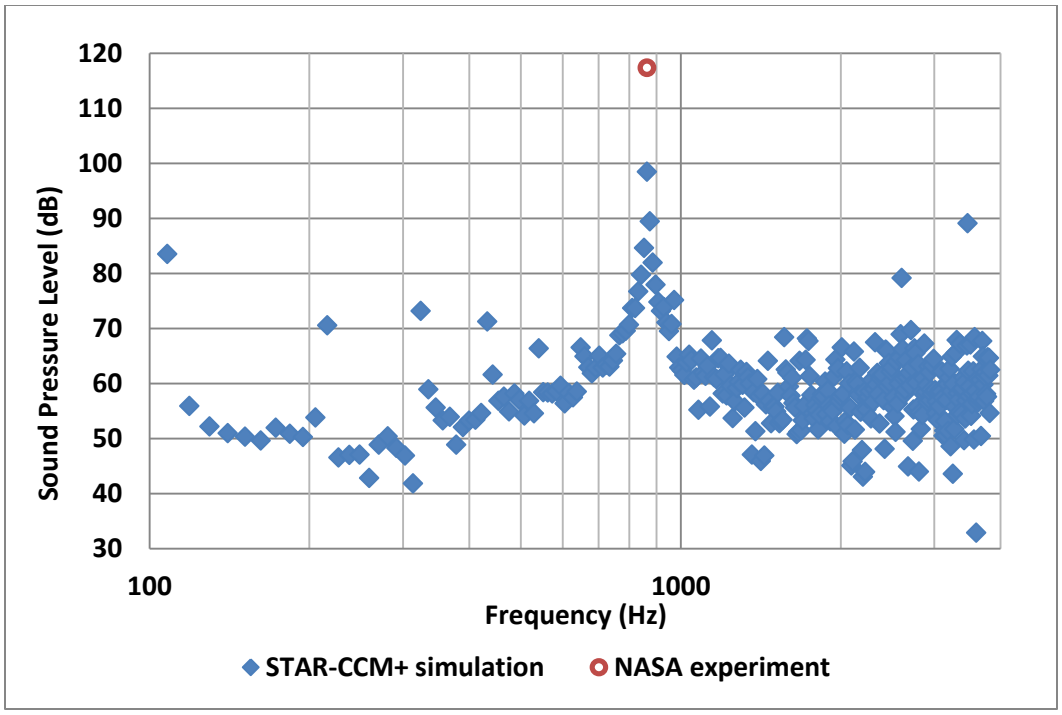

Figure 70: Sound Pressure Level (SPL) at Receiver E for 0.6 Mach number

Figure 71 and Figure 72 show the blade passing tone directivities at the 0.6 and 0.7 Mach numbers. At 0.6 Mach number, the simulation results captured the directivity trend relatively well. However, the magnitude of the sound pressure level is lower as discussed earlier. The is a sharper decrease in sound pressure level between 110° and 131° compared to the NASA results. With an exception to 131°, the directivity is relatively flat. This is consistent with Dittmar [12] observations for axial Mach number less than 0.65.

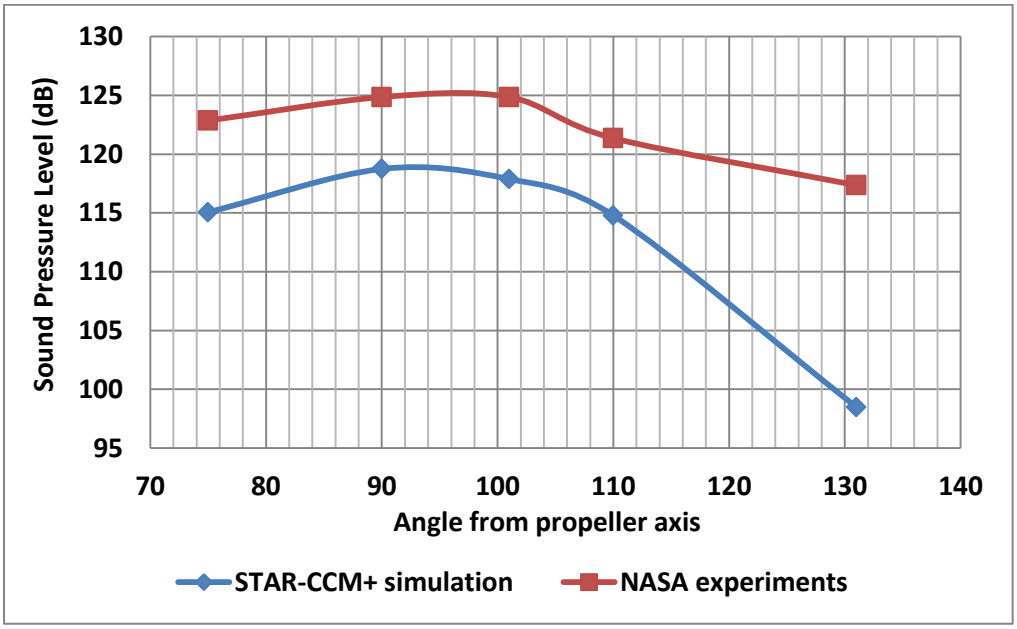

Figure 71: Blade passing tone directivities at 0.6 Mach number

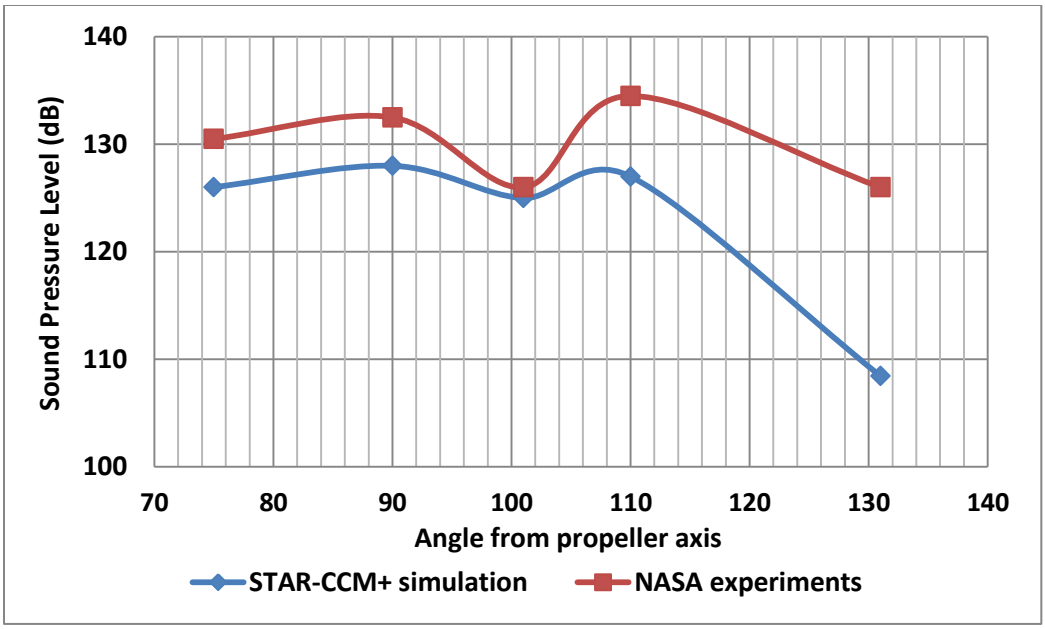

Figure 72: Blade passing tone directivities at 0.7 Mach number

For 0.7 Mach number, the trend for the blade passing tome directivities is somewhat captured. This lobed pattern is consistent with the NASA results presented in Dittmar [12]. There is a slight drop in sound pressure level at 100° from propeller axis followed by a rise in the sound pressure level at 110° to the same level as it was at 90°. Similar to 0.6 Mach number, the magnitude of the sound pressure level is lower except at 100°. The is a sharper decrease in sound pressure level between 110° and 131° compared to the NASA results.

These acoustic results could have been improved if the recommended cell size of the mesh in the permeable region was employed. This step would have prevented some of the noise dissipation across the mesh and allowed for better sound pressure levels.

Chapter 6

Conclusions and Recommendations for Future Work

The aerospace industry has been concerned with the noise issue for many years. The International Civil Aviation Organization (ICAO) introduced Annex 16 in order to set the standards of noise levels. It forces the aircraft and engine manufacturers to abide by these rules and dictates airports to monitor noise levels at and around airports during the take-off and landing situations. The introduction of Chapter 4 regulations in 2006 is the strictest noise protection standard currently in force. They are expected to become more and more stringent with the introduction of more Chapters. This continuous revision and modification of Annex 16 is allowing more and more research funds to be allocated for the field of aeroacoustics.

This research involved simulating two cases: tandem, in-line cylinder case and the NASA SR-7A propeller case. Due to the lack of extensive aerodynamic results for the SR-7A propeller and since predicting the appropriate physics for the aerodynamic component is necessary, the tandem, inline cylinder case is analyzed. The in-depth analysis performed by many researchers on this case produced a very comprehensive data set that can be used for aero-acoustic simulation validation. As a result, this important problem was chosen before the simulation of rotating propellers was attempted to validate STAR-CCM+ as an appropriate simulation tool.

6.1 Tandem In-line Cylinder Case

The tandem cylinder case involved simulating two cylinders equal in diameters (D = 0.05715m) at a separation distance of 3.7D from center-to-center in a flow with Re # = 166,000 corresponding to Mach number of 0.128. The spanwise dimension of the domain was set to 3D to reduce the number of mesh cells and the resulting computational cost.

A Detached Eddy Simulation (DES) coupled with a k-ω SST turbulence model was used to model this case. The acoustic results were obtained using the Ffowcs Williams-Hawkings model. The aerodynamic and acoustic results were compared to the experimental results performed in the Basic Aerodynamic Research Tunnel (BART) and Quiet Flow Facility (QFF) test facilities.

The results showed that there was negative flow behind the upstream cylinder. This caused the shear layers to extend further downstream and eventually lead to the delayed roll-up with the presence of adverse streamwise and favourable crossflow pressure gradients. This affected mean pressure coefficient in the downstream cylinder. No clear distinct peaks are available in the sound pressure level analysis of the receiver locations due to the low sampling time. However,

the primary shedding frequency matches the QFF results with the trends and broadband being reasonably captured.

In order to improve and extend on this simulation, a couple adjustments could be implemented. DES simulations require more time in order to get a fully converged solution. The tandem, in-line cylinder case was run for 0.15s. This does not provide enough time for the physics phenomena to fully develop and resulted in a relatively small sampling time for acoustical purposes.

The experimental results of BART and QFF have been performed using the spanwise distance as 12 D or 16D. The literature review investigation of this case found that the simulations using a 16D spanwise distance provided the most accurate results. Even with a spanwise distance of 12D, the results produced still matched experimental results. The effect of changing this parameter would be very insightful to analyze. However, this would increase the computational cost dramatically.

6.2 NASA SR-7A Propeller Case

The second more important case, SR-7A propeller simulation, was simulated on STAR-CCM+ to produce three different results – power coefficient, unsteady pressure coefficient, and the sound pressure level at receiver locations. All the simulations used the same computational setup and meshing parameters, unless otherwise stated. The moving reference frame approach was employed followed by the sliding mesh approach for the unsteady simulation. The k-ω SST turbulence model was employed at cruise conditions with an advance ratio of 3.06.

The power coefficient results were obtained for 0.6, 0.7, and 0.8 Mach numbers and were compared to NASA experimental results. The simulation results matched the experimental results closely at all Mach numbers. This was the first step in validating the aerodynamics of the case. The unsteady pressure coefficient results would provide a second step.

The unsteady pressure coefficient results were obtained using the inviscid code with a 0.8 Mach number at freestream in order to match the aerodynamic results predicted by NASA Euler code. The inflow angle was set to 1.6° and the results were compared at one transducer location on the suction and pressure surface of the blade (2 locations in total).

Two different meshes were employed on the same domain setup. The coarser mesh did not produce reasonable results. Unusual separation was noticed primarily on the suction surface of the blade and it translated in the unsteady pressure coefficient to be wrongly predicted. There was extensive fluctuation on the waveform and the magnitude were an order of magnitude higher at times. After analysis, it was apparent that the mesh is a major factor and a relatively finer mesh was developed. The results improved significantly at the 0.65R – 0.1c transducer location. The trend was well captured and the fluctuations ceased on the suction and pressure surfaces.

The acoustic simulations involved obtaining the sound pressure levels at 0.6 and 0.7 Mach numbers for the five receiver locations and comparing it to NASA wind tunnel experimental results. At both Mach numbers, the blade passing frequencies and their associated harmonics were well captured for all receivers. The sound pressure levels were well captured for the most part at Receivers A to D, with a maximum deviation of 5 dB below NASA results at Receiver D. At 0.7 Mach number, the simulation results deviated by about 5 dB below the corrected NASA wind tunnel experiments at all receivers for the third harmonic. At Receiver E, the sound pressure levels were about 15 dB below the NASA results for the blade passing frequency for Both Mach numbers. However, the gap continued to increase at the second and third harmonics for 0.7 Mach number.

The directivity results were promising. At the 0.6 Mach number, the simulation results captured the directivity trend relatively well. The is a sharper decrease in the sound pressure level between 110° and 131° compared to the NASA results. With an exception to 131°, the directivity is relatively flat. This is consistent with Dittmar (1985b) observations for axial Mach number less than 0.65.

For 0.7 Mach number, the directivity trend for the blade passing tome directivities is somewhat captured. This lobed pattern is consistent with the NASA results presented in Dittmar (1985b). There is a slight drop in sound pressure level at 100° from propeller axis followed by a rise in the sound pressure level at 110° to the same level as it was at 90°. Similar to 0.6 Mach number, the magnitude of the sound pressure level is lower except at 100°. The is a sharper decrease in sound pressure level between 110° and 131° compared to the NASA results.

In order to improve and extend on this simulation, a few adjustments could be implemented. The unsteady pressure simulations were conducted using an inviscid model in order to compare the results with NASA's Euler code results. An Unsteady RANS turbulence model could be used to obtain the same results and compare it to the experimental results performed by NASA. The introduction of the turbulence model would take into account various physics phenomena that were ignored in this simulation and would complement the acoustic and power coefficient simulations performed.

Another recommendation would be to use a finer mesh in the permeable region of the computational domain. STAR-CCM+ recommends a mesh density of 20 cells per acoustical wavelength in order to perform an accurate simulation. Even though this would require large computational time and resources, it would improve the sound pressure level magnitude greatly.

The final recommendation would be to perform a parametric study about the effect of the region sizes (particularly the permeable size and location) on the acoustical results. This would provide a lot of insight and help in producing a relatively practical mesh for industrial design optimization uses.

Bibliography

[1] AAAC Annual Report FY 2002 – 2003, *AAAC Research Facilities*.

[2] Barlow, J. B., Rae, W. H., & Pope, A. (1999). *Low-Speed Wind Tunnel Testing*. Wiley-Interscience, 3 Ed.

[3] Brès, G. A., Freed, D., Wessels, M., Noelting, S., and Perot, F. (2012). *Flow and noise predictions for the tandem cylinder aeroacoustic benchmark*. Journal of Physics of Fluids, Vol. 24, 036101.

[4] Brentner, K. S., Farassat, F. (2003). *Modeling aerodynamically generated sound of helicopter rotors*. Prog. Aero. Sci. 39:83–120

[5] CD-ADAPCO. (2013). *STAR-CCM+ User Guide Version 8.06*.

[6] De Gennaro, M., Caridi, D., Pourkashanian, M. (2010). *Ffowcs Williams-Hawkings acoustic analogy for simulation of NASA SR2 propeller noise in transonic cruise condition*, ECCOMAS CFD 2010 Conference.

[7] Dickson, N. (2013). *ICAO Noise Standards*. ICAO Symposium on Aviation and Climate Change, "Destination Green". ICAO, Montreal, Canada

[8] Dittmar, J.H., Blaha, B.J., Jeracki, R.J. (1978). *Tone noise of three supersonic helical tip speed propellers in a wind tunnel at 0.8 Mach number*. NASA TM-79046.

[9] Dittmar, J.H. (1984). *Why credible propeller noise measurements are possible in the acoustically untreated NASA Lewis 8-by-6 ft Wind Tunnel*. Journal of American Acoustical Society. Vol. 75, no.6. pp. 1913 – 1914.

[10] Dittmar, J.H., Lasagna, P.L. (1982). *A preliminary comparison between the SR-3 propeller noise in flight and in a wind tunnel*, NASA TM-82805.

[11] Dittmar, J.H. (1985a). *Further comparison of wind tunnel and airplane acoustic data for advanced design high speed propeller models*. NASA TM-86935.

[12] Dittmar, J.H. (1985b). *Preliminary measurement of the noise from the 2/9 scale model of the large-scale advanced propfan (LAP) propeller, SR-7A*. NASA TM-87116.

[13] Dittmar, J.H., Stang, D.B. (1988). *Cruise noise of the 2/9 scale model SR-7A*. Journal of Aircraft, Vol. 25, pp. 740-746.

[14] Dittmar, J.H. (1989). *Cruise noise of the SR-2 propeller model in a wind tunnel.* NASA TM-101480.

[15] Doolan, C. J. (2009). *Flow and Noise Simulation of the NASA Tandem Cylinder Experiment using OpenFOAM. 15th AIAA/CEAS Aeroacoustics Conference*, pp. 1-22.

[16] Farassat, F. (2007). *Derivation of formulations 1 and 1A of Farassat.* Technical Memorandum TM-2007-214853, NASA, NASA Langley Research Center (USA).

[17] Ffowcs Williams, J. and Hawkings, D. (1969). *Sound Generation by Turbulence and Surfaces in Arbitrary Motion*. Philosophical Transactions of Royal Society of London, Series A, Mathematical and Physical Sciences (1934-1990), **264**:1151, pp. 321-342.

[18] Groeneweg, J.F., Bober, L.J. (1988). *NASA advanced propeller research.* NASA TM-101361.

[19] Groeneweg, J.F. (1990), *Aeroacoustics of advanced propellers*. NASA TM-103137.

[20] Gunston, B. (2006). *The Development of Jet and Turbine Aero Engines, 4th Edition*. Haynes Publishing, England, UK.

[21] Heidelberg, L.J., Nallasamy, M. (1990). *Unsteady blade pressure measurements for the SR-7A propeller at cruise conditions.* AIAA-90-4022.

[22] Hughes, C.E., Gazzaniga, J.A. (1988). *Summary of low-speed wind tunnel results of several high-speed counterrotation propeller configurations*. NASA TM-100945.

[23] Hutcheson, F. V., Brooks, T. F. (2006). *Noise radiation from single and multiple rod configurations*. 12th AIAA/CEAS Aeroacoustics Conference, Paper No. 2006-2629.

[24] Jeracki, R.J., Mikkelson, D.C., Blaha, B.J. (1979). *Wind tunnel performance of four energy efficient propellers designed for Mach 0.8 cruise*. NASA TM-79124.

[25] Jenkins, L. N., Neuhart, D. H., McGinley, C. B., and Choudhari, M. M. (2006). *Measurements of unsteady wake interference between tandem cylinders*. 36th AIAA Fluid Dynamics Conference and Exhibit, Paper No. 2006-3202.

[26] Jones, W. P., & Launder, B. E. (1972). *The Prediction of Laminarization with a Two-Equation Model of Turbulence.* International Journal of Heat and Mass Transfer, Vol. 15, 1972, pp. 301-314.

[27] Khorrami, M. R., Choudhari, M. M., Jenkins, L. N. and McGinley, C. B. (2005). *Unsteady flowfield around tandem cylinders as prototype for component interaction in airframe noise*. 11th AIAA/CEAS Aeroacoustics Conference, Paper No. 2005-2866.

[28] Khorrami, M. R., Lockard, D. P., Choudhari, M. M., Jenkins, L. N. Neuhart, D. H., and McGinley, C. B. (2006). *Simulations of bluff body flow interaction for noise source modeling*. 36th AIAA Fluid Dynamics Conference and Exhibit, Paper No. 2006-3203.

[29] Kotapati, R. B, Squires, K. D, and Forsythe, J. R. (2004). *Prediction of the Flow over an Airfoil at Maximum Lift.* AIAA, Paper No. 2004- 0259.

[30] Lighthill, M. (1952). *On Sound Generated Aerodynamically. I. General Theory. Proceedings of the Royal Society of London. Series A, Mathematical and Physical Sciences (1934-1190)*, 211:1107, pp. 564-587.

[31] Lighthill, M. (1954). *On Sound Generated Aerodynamically. I. Turbulence as a Source of Sound. Proceedings of the Royal Society of London. Series A, Mathematical and Physical Sciences (1934-1190)*, 222:1148, pp. 1-32.

[32] Lockard, D. P., Khorrami, M. R., Choudhari, M. M., and Stead, D. J. (2007). *Tandem Cylinder Noise Predictions*. 13th AIAA/CEAS Aeroacoustics Conference.

[33] Menter, F. R. (1992). *Improved Two-Equation k-omega Turbulence Models for Aerodynamic Flows.* NASA TM 103975, October 1992.

[34] Menter, F. R. (1993). *Zonal Two Equation k-omega Turbulence Models for Aerodynamic Flows.* AIAA Paper 93-2906, July 1993.

[35] Menter, F. R. (1994). *Two-Equation Eddy-Viscosity Turbulence Models for Engineering Applications.* AIAA Journal, Vol. 32, No. 8, pp. 1598-1605.

[36] Menter, F. R. & Kuntz, M. (2002). *Adaptation of Eddy Viscosity Turbulence Models to Unsteady Separated Flows Behind Vehicles. The Aerodynamics of Heavy Vehicles: Trucks, Buses and Trains*, Springer, Asilomar, CA.

[37] Menter, F. R., Kuntz, M., and Langtry, R. (2003). *Ten Years of Industrial Experience with the SST Turbulence Model*. Turbulence, Heat and Mass Transfer 4, ed: K. Hanjalic, Y. Nagano, and M. Tummers, Begell House, Inc. pp. 625 - 632.

[38] Nallasamy, M., Groeneweg, J.F. (1989). *Prediction of unsteady blade surface pressures on an advanced propeller at an angle of attack*. AIAA-89-1060.

[39] Nallasamy, M., Groeneweg, F.F. (1990). *Unsteady Euler analysis of the flow field of a propfan at an angle of attack.* AIAA-90-0339.

[40] Qantas Airlines. *Our Approach to Aircraft Noise Management*. Qantas.com .Retrieved February 20, 2014, from http://www.qantas.com.au/travel/airlines/our-approach/global/en#jump1

[41] Spalart, P. R., Jou, W.-H., Stretlets, M., and Allmaras, S. R. (1997). *Comments on the Feasibility of LES for Wings and on the Hybrid RANS/LES Approach.* Advances in DNS/LES, Proceedings of the First AFOSR International Conference on DNS/LES.

[42] Stefko, G. L., Rose, G.E, & Podboy, G.G. (1987). *Wind Tunnel Performance Results of an Aeroacoustically Scaled 2/9 Model of the PTA Flight Test Prop-fan*. NASA TM-89917.

[43] Strelets, M. (2001). *Detached Eddy Simulation of Massively Separated Flows*. AIAA 2001-0879.

[44] Wilcox, D.C. (1988). *Re-assessment of the scale-determining equation for advanced turbulence models.* AIAA Journal, vol. 26, no. 11, pp. 1299-1310.

[45] Wilcox, D.C. (2008). *Formulation of the k-ω turbulence model revisited*. AIAA Journal, 46(11), pp. 2823–2838

[46] Woodward, R.P., Loeffler, I.J., Dittmar J.H. (1989). *Measured far-field flight noise of a counterrotation turboprop at cruise conditions*. NASA TM-101383.

[47] Woodward, R.P., Loeffler, I.J. (1991). *Inflight source noise of an advanced full-scale single-rotation propeller*. NASA TM-103687.

[48] Zdravkovich, M. (1987). *Review of flow interference between two cylinders in various arrangements*. ASME Journal of Fluids Engineering, Vol. 99, pp. 618-631.